

© Copyright 2019

Yuandong Li

Application of Functional Optical Coherence Tomography Angiography in Neurovascular Research

Yuandong Li

A dissertation

submitted in partial fulfillment of the
requirements for the degree of

Doctor of Philosophy

University of Washington

2019

Reading Committee:

Ruikang K. Wang, Chair

Ying Zheng

Jonathan T.C. Liu

Program Authorized to Offer Degree:

Bioengineering

University of Washington

Abstract

Application of Functional Optical Coherence Tomography Angiography in Neurovascular Research

Yuandong Li

Chair of the Supervisory Committee:
Professor Ruikang K. Wang
Bioengineering

Optical coherence tomography (OCT) is a revolutionary non-invasive imaging technique that can perform high-resolution, cross-sectional tomographic imaging of the internal microstructure in biological tissues by measuring backscattered or backreflected light. Its functional extension, OCT angiography (OCTA), analyzes the intrinsic scattering property of the heterogenous tissue bed to extract dynamic blood flow signals to the capillary level without a need of contrast agents. Aside from the commonly known application of OCTA in clinical ophthalmology for imaging the retinal blood flow in human subjects, the technique has recently emerged as a useful tool in pre-clinical neuroscience for imaging cerebral microcirculation and dynamics in rodent models. The main goal of this thesis is to progress with the application of OCT/OCTA in neurovascular research and solve questions in neurovascular functions and associated disorders, including

ischemic stroke, aging, and Alzheimer's disease. To achieve this goal, firstly, novel mouse cranial window techniques will be developed together with series of OCTA algorithms to image the cerebral blood flow in mouse brain that covers capillary, pial and penetrating vessels. Then, a newly developed method, OCTA capillary velocimetry, will be applied to investigate the capillary flow pattern adjustment during neurovascular coupling and brain oxygenation. Next, vasodynamics of pial and penetrating arterioles of the cerebral collateral network will be unraveled in rodent models of ischemic stroke, upon which new details of a vascular self-protective mechanism will be revealed. Lastly, the multifunctional OCTA will be applied for a comprehensive investigation of aging-associated cerebral vasculature and blood flow changes that give indications to Alzheimer's disease.

TABLE OF CONTENTS

List of Figures	v
List of Tables	vii
Chapter 1. Introduction	1
1.1 Significance and research motivation	1
1.2 Optical coherence tomography (OCT).....	3
1.2.1 Principle of OCT.....	3
1.2.2 Fourier-domain OCT	4
1.3 OCT data structure.....	5
1.4 OCT angiography (OCTA).....	6
1.4.1 Optical microangiography (OMAG).....	7
1.4.2 Doppler OMAG (DOMAG)	8
1.4.3 Eigen-decomposition OMAG (ED-OMAG).....	9
1.4.4 OCTA capillary velocimetry.....	10
1.5 Scope of the thesis	14
Chapter 2. Developing cranial window techniques to image mouse cerebral blood flow with OCTA.....	15
2.1 Background and motivation	15
2.2 Methods.....	16
2.2.1 Animal models	16
2.2.2 Cranial window techniques.....	17
2.2.3 Imaging protocol.....	18

2.3	Results.....	19
2.4	Discussion.....	24
2.5	Updates	26
Chapter 3. Capillary flow homogenization during functional activation revealed by OCTA based capillary velocimetry		
		28
3.1	Background and motivation.....	28
3.2	Material and Methods	31
3.2.1	Animal preparation	31
3.2.2	Hindpaw electrical stimulation and laser speckle contrast imaging (LSCI).....	32
3.2.3	OCTA imaging.....	33
3.2.4	Capillary velocity analysis.....	33
3.2.5	Capillary flow parameter evaluation.....	34
3.2.6	Statistical analysis.....	35
3.3	Results.....	35
3.3.1	Activation at HLS1 upon hindpaw electrical stimulation.....	35
3.3.2	OCTA angiogram and velocimetry at HLS1 and CTRL	36
3.3.3	Capillary transit time distribution change and CTTH reduction at HLS1	38
3.3.4	Capillary transit time distribution at control region.....	39
3.3.5	Hemodynamic parameter changes upon stimulation at HLS1 and CTRL.....	40
3.4	Discussion.....	41
3.5	Conclusion	44

Chapter 4. Vasodynamics of pial and penetrating arterioles in relation to arteriolo-arteriolar anastomosis after focal stroke.....	46
4.1 Significance.....	46
4.2 Material and Methods.....	47
4.2.1 Animal preparation.....	47
4.2.2 Optical microangiography.....	48
4.3 Results.....	50
4.3.1 Pial and penetrating arteriole vasodynamics under basal conditions.....	50
4.3.2 Pial and penetrating arteriole vasodynamics in response to MCAO.....	52
4.3.3 Pial and penetrating arteriole vasodynamics in relation to AAA.....	55
4.4 Discussion.....	57
Chapter 5. Aging-associated changes in cerebral vasculature and blood flow as determined by quantitative OCTA.....	61
5.1 Background and motivation.....	61
5.2 Method and materials.....	63
5.2.1 Animal preparation.....	63
5.2.2 OCTA scanning protocols.....	65
5.3 Data analysis.....	66
5.3.1 Arterial tortuosity measurement.....	66
5.3.2 Capillary vessel density quantification.....	67
5.3.3 CBF analysis.....	68
5.3.4 Capillary mean velocity and velocity heterogeneity calculation.....	68

5.3.5	Statistics	69
5.4	Results.....	69
5.4.1	Measured physiology parameters	69
5.4.2	Arterial tortuosity.....	70
5.4.3	Capillary vessel density	71
5.4.4	CBF measurements from PA flow	73
5.4.5	Capillary mean velocity and heterogeneity.....	74
5.5	Discussion.....	76
5.5.1	Aging-related vessel tortuosity increase	76
5.5.2	Aging-related capillary loss	79
5.5.3	CBF modification in the aging brain	81
5.5.4	Capillary velocity heterogeneity development during aging.....	82
5.5.5	Study limitation.....	84
5.6	Conclusion	85
Chapter 6. Summary and future work.....		87
Bibliography		89

LIST OF FIGURES

Figure 1.1. Organizations of cerebral vascular network [2].	1
Figure 1.2. Schematic illustration of time-domain OCT [7].	4
Figure 1.3. Schematic illustration of SD-OCT [7].	5
Figure 1.4. OCT signals of dynamic and static tissues.	6
Figure 1.5. Eigenvalue spectrum analyzed from mouse cortical tissue.	11
Figure 1.6. The relationship between frequency and eigenvalue.	12
Figure 1.7. Validation of ED-based capillary velocimetry with microfluidic phantom.	13
Figure 2.1. Microscopic images of intact skull and cranial windows.	17
Figure 2.2. OMAG MIP of microcirculation network up to ~1 mm depth.	20
Figure 2.3. Cross-sectional view of the flow and structure images.	21
Figure 2.4. DOMAG MIP view of microcirculation network at 50 ~ 450 μ m depth.	22
Figure 2.5. Comparison of detectable vessel density for n=5.	24
Figure 2.6. Depth color coded OMAG MIP of microcirculation network.	27
Figure 3.1. Schematics of the Jespersen and Østergaard model of CTTH and MTT	29
Figure 3.2. Oxygenation mapping during functional activation	36
Figure 3.3. Cerebral angiogram and capillary velocity maps	37
Figure 3.4. Capillary transit time distribution at HLS1	39
Figure 3.5. Capillary transit time distribution at control region	40
Figure 3.6. Statistical comparison of capillary parameters between HLS1 and CTRL	41
Figure 4.1. Pial and penetrating arteriole vasodynamics under basal conditions	51
Figure 4.2. Changes in flow pattern in the pial network during MCAO and reperfusion	54
Figure 4.3. The lumen diameter distribution of pial and penetrating arterioles.	55
Figure 4.4. Vasodynamics of penetrating arterioles with respect to AAA during stroke.	56
Figure 4.5. Lumen diameter, velocity, and flow comparison.	57
Figure 6.1. System setup and cranial window preparation	64
Figure 6.2. Method used for vessel tortuosity measurements	67
Figure 6.3. Comparison of cerebral pial collateral vessel tortuosity	71
Figure 6.4. Comparison of the cerebral capillary vessel density	73

Figure 6.5. CBF and PA/RV parameter comparisons.....	74
Figure 6.6. Capillary flow velocity and heterogeneity quantification	75

LIST OF TABLES

Table 3.1. Capillary flow parameters during rest and stimulation (n=12).....	41
Table 6.2. Measured physiology parameters	69
Table 6.3. Characteristic age-associated changes	76

ACKNOWLEDGEMENTS

I have received the most incredible support throughout this journey, for which I am thankful for the people who took a part in it.

Firstly, I would like to express my deepest gratitude to my advisor, Prof. Ruikang Wang, for being the best mentor that I can possibly have. This work would not have been done without his tremendous support and guidance. Thank you for trusting my potentials, guiding me with directions, and training me to be a scholar. Thank you for providing me with the best resources to explore and develop my research. Thank you for your patience, kindness, and the laughs. Your dedication to science and wisdom in life have constantly inspired me. I am honored to have had the opportunity to work in your lab.

I would like to thank my PhD dissertation committee members, Prof. Ying Zheng, Prof. Jonathan Liu, who have spent their valuable time to review my work and give me suggestions, and Prof. Dan Fu (Graduate School Representative), for making room in his busy schedule to attend my final defense.

I sincerely extend my appreciation and best regards to all the lab members, both current and previous, in the Biophotonics and Imaging Laboratory (BAIL). Thank Dr. Utku Baran, my working partner at the very beginning who has mentored me incredibly in my early research; Dr. Woo June Choi and Dr. Wei Wei and who I closely collaborated with for many publications. Great thanks to Dr. Shaozhen Song, Dr. Qinqin Zhang for their significant help on systems and algorithms, and Dr. Jingjiang Xu and Dr. Chenxi Li for many important discussions. Special thanks to Dr. Zhongwei Zhi for introducing me to the lab and being a great mentor in my early days in

the lab, and Dr. Hequn Wang for getting me started on publishing papers, as well as Dr. Suz Dziennis and Dr. Jia Qin who taught me rodent surgeries.

I was also lucky to work with and learn from our excellent external collaborators, Prof. Jialing Liu and her team from UCSF, Prof. John Morrison and his team from Casey Eye Institute at OHSU, as well as Prof. Nabil Alkayed and his team from OHSU.

Special thanks to Prof. Gerald Pollack at UW for introducing me to research and training me to think critically about scientific problems in my sophomore/junior years in college.

I am eternally grateful for my family for their endless love and support. My parents, Mr. Gaobao Li and Ms. Meiju Ma, who love me wholeheartedly and unconditionally. They give me the courage to pursue my true passion and overcome the difficulties. It was my inspiration to make them proud. My husband and best friend, Dr. Xiang Chen, who has given me countless help and support throughout. This journey could have been really tough without him.

I am thankful for all my friends who have provided me with friendship, love, and encouragement.

Chapter 1. INTRODUCTION

1.1 SIGNIFICANCE AND RESEARCH MOTIVATION

The energy requirements of the cerebral cortex, the outer neural layer of the brain responsible for the complex brain functions [1], are met almost exclusively by oxidative metabolism of glucose, necessitating continuous delivery of oxygen to the tissue from flowing blood through a highly organized and dense vascular network [2]. Therefore, characterizing the cerebral vasculature and circulatory behavior *in vivo* at high resolution is crucial for understanding brain's functions and dysfunction. Non-invasive imaging of cerebral blood flow is therefore indispensable for both research and clinical cares, tremendously helping with our understanding of the neurovascular system and the treatment interventions of neurovascular diseases and neurometabolic disorders.

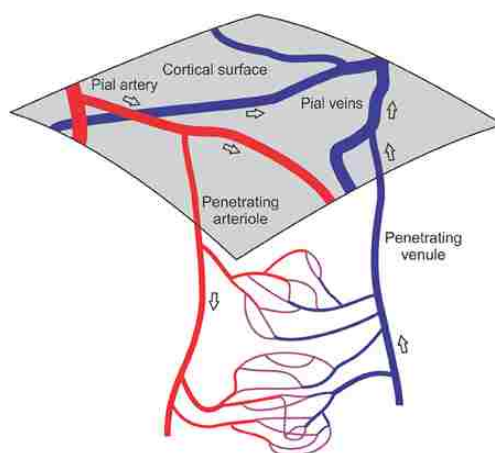


Figure 1.1. Organizations of cerebral vascular network [2].

A unique organization of the cortical vascular network is presented in **Figure 1.1**. In the cerebral cortex, a mesh of pial arteries and veins lies on the cortical surface. Penetrating arterioles and venules branch off the pial vessels and transverse the thickness of the cortex, supplying dense arrays of capillaries. Through decades of research, our understanding of this vascular system

continues to advance with imaging technologies. From the macroscopic modality, such as magnetic resonance imaging (MRI), in clinical settings, to the microscopic techniques, such as two-photon microscopy (TPM), in experimental research, a common goal of pursue has been imaging with high spatial and temporal resolution, while being non-invasive to the native neurovascular environment. However, neither quality has been proven easy to be achieved. MRI assessment of blood flow often requires injecting paramagnetic contrast agents into the patient's blood stream [3], which is also limited in spatial resolution (arteriole level in best cases) and temporal resolution (hours). TPM is capable of ultrahigh resolution ($\sim 1 \mu\text{m}$) imaging with fluorescent markers, and have been used to map the detailed vasculature in rodent cortex [4]. The temporal resolution for obtaining functional blood flow information in TPM, such as red blood cells (RBC) velocity, is extremely poor, taking hours to measure a few vessels. Other optical-based techniques, such as laser speckle contrast imaging (LSCI) [5] and intrinsic signal optical imaging (ISOI) [6], are also options to monitor the neurovascular interactions, which can measure the rapid relative changes of blood flow and oxygenation in the cerebral vessels during neural activation in a large transverse field of view. Nevertheless, these techniques are limited to two-dimensional (2-D) hemodynamic mapping, mostly in pial vessels, lacking the ability to reveal important information in penetrating and capillary networks.

Currently, there is a critical limitation in the field of neurovascular research: to efficiently image the uniquely structured cerebral vasculature and obtain functional blood flow information at capillary-level resolution *in vivo*. To overcome the limitation of imaging in previous research and help with solving the outstanding questions in neuroscience, I will apply the functional optical coherence tomography angiography (OCTA) in mouse models to investigate the neurovascular functions and neurovascular disorders, including ischemic stroke, aging, and Alzheimer's disease.

In the following sections, I will briefly introduce the OCT imaging modality and a variety of its functional extensions to be applied in this thesis.

1.2 Optical coherence tomography (OCT)

OCT is an imaging modality analogous to ultrasound, but measuring the backreflected light waves from the biological tissues instead of sound waves. OCT is being rapidly developed since it is non-invasive, label-free, and generates three-dimensional, high-resolution images of the biological sample *in vivo*. Here, I will illustrate how these characteristics can be achieved through going over the basic principle of OCT.

1.2.1 *Principle of OCT*

OCT is an interferometric technique, which analyze the interference signals between a split and later re-combined broadband optical field [7]. An early OCT system, also known as time-domain OCT is shown in **Figure 1.2**. It consists of an interferometer with a low coherence and broad bandwidth light source. The light (E_{in}) passes through a beam splitter and is split into two beams, where one travels in a reference path (E_r) to a reference mirror, and the other beam goes into the biological samples (E_s). The detected backscattered signals (E_{out}) from the reference mirror and the sample generate an interference pattern with maximal intensity if the optical path length from both split paths are matched to within the coherence length of the light source. By changing or scanning the position of the reference mirror, depth-resolved tissue reflectivity can be reconstructed from the interference pattern, which is recorded as a one-dimensional intensity profile along the axial (depth) direction (A-line). Due to the slow mechanical scanning of the reference mirror, however, the speed of the time-domain OCT is limited, with the A-line (one depth scan) scanning rate achieved at a maximum of ~ 8 kHz.

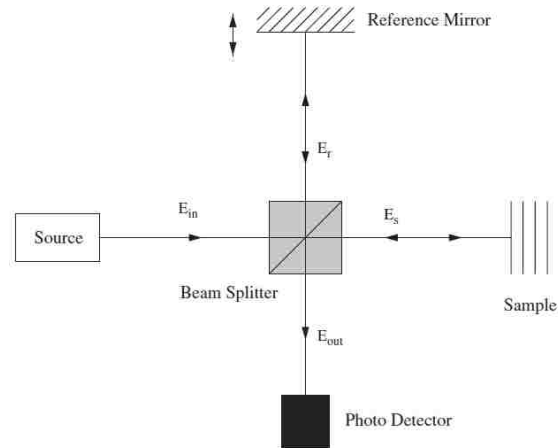


Figure 1.2. Schematic illustration of time-domain OCT [7].

Basic OCT system based on a Michelson interferometer. E_{in} : incident light; E_r : reference light; E_s : sample light; E_{out} : detected light.

1.2.2 *Fourier-domain OCT*

Instead of physically scanning a reference mirror, a later version of OCT detects the backscattering signals in frequency domain, which directly encodes the time delay information in spectral interferogram. It can be shown that a Fourier transform of spectral interference data provides information of the sample along the depth which is equivalent to the one obtained by moving the reference mirror. This version of OCT is often referred to as Fourier-domain OCT (FD-OCT). Spectral-Domain OCT (SD-OCT) is a sub-category of FD-OCT. In SD-OCT (**Figure 1.3**), the reference mirror is stationary, and the interference pattern is split by a grating into its frequency components and all of these components are simultaneously detected by linear detector. Frequency information from all depths of one A-line in tissue is acquired in parallel and converted to an intensity profile by a simple operation of the Fourier transformation of captured spectral interferogram.

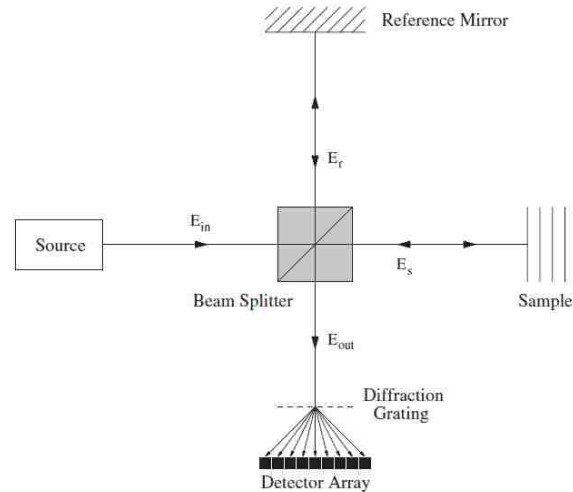


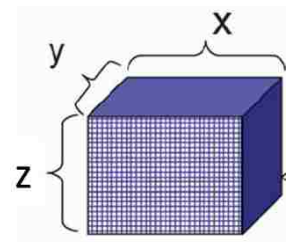
Figure 1.3. Schematic illustration of SD-OCT [7].

Basic SD-OCT system based on a Michelson interferometer. E_{in} : incident light; E_r : reference light; E_s : sample light; E_{out} : detected light.

The introduction of spectrometer and frequency domain detection have improved the image acquisition speed dramatically, to between 26K to 100K [8], and the implementation of broadband light source with broader bandwidth enhances the axial resolution to between $10\ \mu\text{m}$ to $2\ \mu\text{m}$ [9]. A higher signal-to-noise ratio (SNR) is also achieved. These advantages enable the FD-OCT to image not only the 3-D tissue microstructure but also dynamic information, such as *in vivo* blood flow, using its functional extension: OCT angiography.

1.3 OCT DATA STRUCTURE

As introduced in the previous section, an A-line (or A-scan) from OCT scans represents the depth information in one-dimensional space. This dimension is referred to the z-axis in the following context. The second dimension can be obtained by making multiple A-scans in the transverse



direction to form a B-scan (OCT cross-sectional frame) in the x-axis, and the three-dimensional (3-D) imaging can be achieved by making multiple B-scans in the y-axis that composes the

tomographic images to a volumetric dataset. An *en face* concept is often used to visualize the projection of a 3-D dataset from the x-y plane from the entire depth, or at a designated depth (orthoslice).

1.4 OCT ANGIOGRAPHY (OCTA)

The basic concept of OCTA is to use the moving particles, for example, the RBC in the blood vessels, in the biological tissues as an intrinsic contrast to map blood flow without a need of dye injections. Shown in **Figure 1.4**, when observing two types of OCT signals over time, the signal backscattered from tissue components (a and d) remains steady for there is no movement in the static tissue, while the backscattering signal from blood vessels (b and c) changes over time as the RBC tumbling and moving while flowing in the blood stream. By calculating the OCT signals acquired at the same location at different time points (M-scan), moving particles is discriminated from the static tissue to generate angiograms.

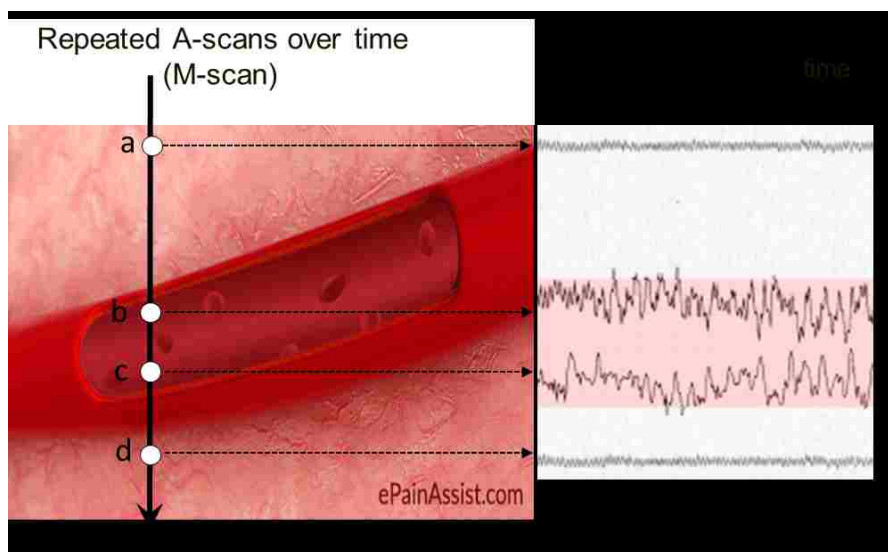


Figure 1.4. OCT signals of dynamic and static tissues.

A simplified schematic figure of the concept of OCTA. Signals are sample from four different points (a, b, c, and d) in the M-scan, where a, d are located at the static tissue, and b, c are located within a functional blood vessel. Dynamic changes in the OCT signals for b and c are observed over time while the other two remain steady.

OCT signal is naturally a complex function, consisting of amplitude and phase information, and can be expressed in the Equation 1.1:

$$C_{OCT}(x, z, t) = I(x, z, t)e^{-i\Phi(x,z,t)} \quad (1.1)$$

where I indicates the amplitude component and Φ represents the phase component in an OCT signal. Various OCTA algorithms have been vigorously developed in recent years to extract the flow signal based on different components of OCT signals. Methods include phase-signal-based OCTA [10]–[12], intensity-signal-based OCTA [13]–[16], and complex-signal based OCTA [17], [18] are all proven practical to extract dynamic blood flow information from the living tissue bed. Due to the space limitation, here I only describe the OCTA algorithms to be applied in the thesis.

1.4.1 *Optical microangiography (OMAG)*

OMAG is a representative of complex-signal-based OCTA algorithm, proposed firstly by Wang et al. in 2007 [17] and then refined into a later implementation in 2010 [19], [20]. The rationale of including both phase and amplitude components in the OCT signals here is to improve the sensitive of flow detection. The flow signal based on OMAG algorithm is calculated by subtracting consecutive complex signals, as shown in Equation 1.2:

$$Flow_{OMAG}(x, z) = \frac{1}{N-1} \sum_{i=0}^{N-1} |C_{i+1}(x, z) - C_i(x, z)| \quad (1.2)$$

where N indicates the repetition number of B-scans at the same transverse location, and $C_i(x, z)$ indicates the complex signal (carrying both intensity and phase values) in i -th B-scans at lateral location x and depth position z . As indicated in the equation, the final flow intensity is obtained by calculating the average of the absolute values of the complex signal differences in each B-scan pair. In its first demonstration [17], the number of B-scans at each transverse location was set to 4, determined based on the tradeoff between imaging time and SNR. Though 2 B-scans at the same

location would be sufficient to detect blood flow with good image quality [21], we have used 8 repeated B-scans in the cerebral blood flow imaging to enhance the SNR for capillary flow contrast. With the use of Hilbert transformation, OMAG is also able to discriminate the directions of the moving RBC relative to the incident OCTA beam direction, and therefore, OMAG can further provide the flow image either with or without directional information [22].

1.4.2 Doppler OMAG (DOMAG)

Taking the advantage of OMAG, a phase-resolved Doppler OCT technique was combined to develop DOMAG [23] to map the axial velocities of the blood flowing in functional vessels within tissue beds *in vivo*. The application of OMAG to firstly reject the static tissue signal from dynamic blood flow before applying the phase-resolved methods makes DOMAG more sensitive to flow velocity detection within the microcirculatory network. Then, the phase difference ($\Delta\varphi(z)$) between adjacent A-scans of OMAG flow signals is calculated to realize the flow axial velocity (v_{axial}):

$$v_{axial}(z) = \frac{\lambda\Delta\varphi(z)}{4\pi n\Delta t} \quad (1.3)$$

where Δt is the time interval between adjacent A-lines and n is the refraction index of the tissue. Accordingly, longer Δt is required for detecting slow velocities, which might still be insufficient to detect irregular and slow RBC flow in capillaries. Later on, a variation of DOMAG was introduced [24] by choosing A-lines at various time points, to have change multiple Δt s, for analyzing the Doppler signal. This method is important in the investigation of impaired blood flow within microcirculatory tissue beds, because it can provide Doppler analyses over a wide velocity range from capillaries to arterioles and venules, providing useful information to aid in the assessment of whether the blood flow within injured region of interest is compromised or ceased to flow.

This method is implemented to the current application of DOMAG in the evaluation of blood flow characteristics in the cerebral penetrating arterioles, a group of vessels mostly perpendicular to the cortical surface, being most sensitive axial flow velocity detection. In addition to the axial velocity of the penetrating arterioles obtained with DOMAG, the rate of the blood flow can be also obtained using the flow area integration method:

$$F = \iint_{xy\ plane} v_z(x, y) dx dy \quad (1.4)$$

According to a validation in the previous study [25], this procedure does not require explicit calculation of the vessel angle. By knowing the cross-sectional occupying area of the penetrating flow from an *en face* cut in the 3-D volume (orthoslice), the flow rate of the chosen vessels can be deduced, and the area total flow, also referred as cerebral blood flow (CBF) in the following studies, can be obtained by measuring multiple penetrating arterioles in a cortical region.

1.4.3 *Eigen-decomposition OMAG (ED-OMAG)*

An eigen-decomposition (ED)-based method was firstly demonstrated in 2011 [18] with OMAG in order to minimize the false-positive flow signals resulted from the tissue motion for OCTA. In this method, the OCT signal at each voxel in the 3-D volume was modeled as a superposition of three independent components: tissue signal (the clutter components coming from stationary or slowly moving tissue structures), hemodynamic signal, and system noise. Due to its best mean-square approximation of the clutter, eigen-regression filters could theoretically provide maximum clutter regress, and thus could successfully remove the bulk motion while preserving the flow information. The ED-based algorithm was later improved in 2014 with a multiple signal classification method (MUSIC) [26]. The MUSIC method was capable of decomposing the backscattered OCT signal into orthogonal basis functions and distinguishing the flow signal caused by moving RBC from static tissue and system noise. The angiography results with this method

outperform the flow images using phase-compensation method or static high-pass filtering to remove the bulk motion and is thus being implemented in the most current version of ED-OMAG for a variety of *in vivo* applications. More importantly, the flow signal obtained using the MUSIC approaches is amenable to provide quantifiable flux information about the dynamic blood flow, which was validated with a phantom study using OMAG [26]. A further improvement of the method has been made to develop the ED-based OCTA capillary velocimetry, which is illustrated in the next section.

1.4.4 *OCTA capillary velocimetry*

The MUSIC method only provided flow velocity of relatively large functional blood vessels, with no indication of its possibility to quantify capillary flow and microcirculation behavior. A most recent development has used an alternative model-based statistical analysis approach of the ED-based analysis to estimate the frequency component of the dynamic OCT signals due to moving RBC from high-speed scans [27], which finally achieved large-scale quantitative capillary velocity measurements in the chaotic tissue bed. The basic idea of this method is observing in the repeated A-scans (50 repetition in this case), the total energy in the received OCTA signal equals the sum of all the eigenvalues. Therefore, the eigenvalue distribution must be a measure of the signal spectrum. In SD-OCT, the spectrum can be regarded as the generalization of the Fourier power spectrum. **Figure 1.5** shows a typical eigenvalue spectrum with their represented signal makeup. The static signal can be suppressed to retain blood flow signal through applying eigenregression filtering, such as removing the first eigenvalue in this case.

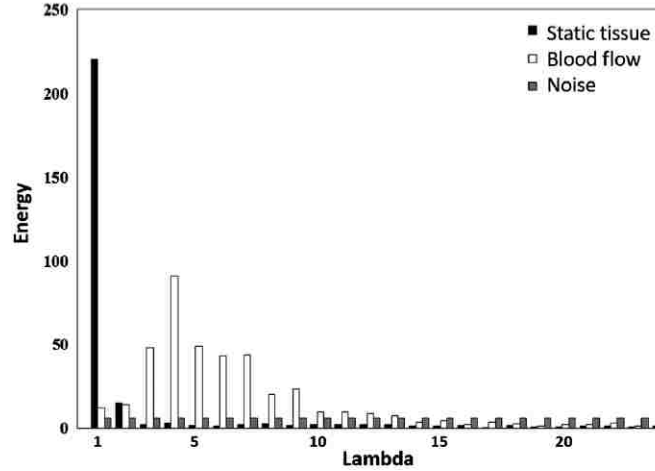


Figure 1.5. Eigenvalue spectrum analyzed from mouse cortical tissue.

Typical eigenvalue spectrum where 30 eigenvalues are analyzed from the signals representing static tissue components, dynamic motion signals, and system noise.

The power spectrum of the signal is the Fourier transform of the autocorrelation function defined as:

$$G_x(\omega) = \int_{-\infty}^{\infty} R_x(\tau) e^{-i\omega\tau} d\tau \quad (1.5)$$

If the frequency components have spectral support on the interval $(-\pi, \pi)$, the signal power indicating the presence of blood flow can be simplified as follows:

$$P = \int_{-\pi}^{\pi} G(\omega) d\omega \quad (1.6)$$

The mean frequency (MF) of signal frequency spectrum, ω_m , representing the mean velocity of blood flow within the scanned tissue volume; and the bandwidth frequency (BF), B^2 , of the frequency spectrum, which is related to the flow fluctuation (temporal velocity heterogeneity) can be defined as Equation 1.7 and Equation 1.8, respectively.

$$\omega_m = \frac{1}{P} \int_{-\pi}^{\pi} \omega G(\omega) d\omega \quad (1.7)$$

$$B^2 = \frac{1}{P} \int_{-\pi}^{\pi} (\omega - \omega_m)^2 G(\omega) d\omega \quad (1.8)$$

The estimation of spectral moments can be obtained using the well-known lag-one autocorrelation equation given by the following equation:

$$\omega_k = \frac{FPS/2}{2\pi} \arg\{R(1)_k\}, \text{ for } R(1)_k = \frac{1}{N_D-1} \sum_{m=0}^{N_D-2} e_k^*(m)e_k(m+1), \quad (1.9)$$

where is the lag-one autocorrelation value for the k^{th} eigenvector, FPS is the sampling rate, and N_D is the number of eigenvectors. At this point, the frequency content of the individual eigenvectors, with the spectral band information and the eigencomponents that represent them are obtained. Here, one frequency measure of interest is each eigenvector's MF. **Figure 1.6** provides the relationship between frequency and eigenvectors, presented in box-whisker plot form, which were evaluated from 10 volumetric scans from a mouse brain *in vivo*. The red squares connected with a black dashed line indicate the MF of each eigenvector. Combined with the energy spectrum of **Figure 1.5**, a conclusion were made that the highest energy is associated with the highest eigenvalue, representing the static or slowing moving signal, correspond to the eigenvector of lowest frequency.

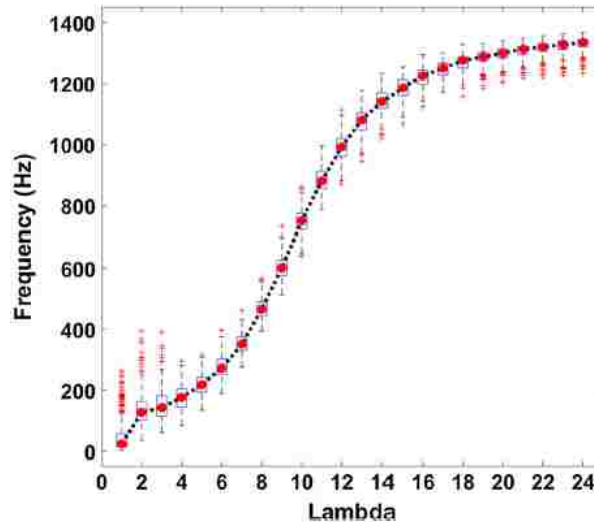


Figure 1.6. The relationship between frequency and eigenvalue.

The relationship between frequency and eigenvalue (eigenvector) presented in box-whisker plot form. The results were obtained and evaluated from 10 3-D scans of rodent brain *in vivo*.

The proposed ED-based capillary velocimetry was validated with a phantom experiment in microfluidic channels perfused with 5% intralipid solution with multiple predefined flow velocities. The advantage of MF analysis in flow velocity estimation is clearly observed (Figure 1.7). The OCT signal power decomposed by ED that is related to the OCTA signal intensity increases with velocity but approach plateau, which agrees with previous publication [28], indicating its relationship with flow flux (Figure 1.7d). On the other side, the relationship between MF and velocity among all channels is shown linear, which indicate a one-on-one relationship between MF to the flow velocity regardless of the channel size (Figure 1.7e).

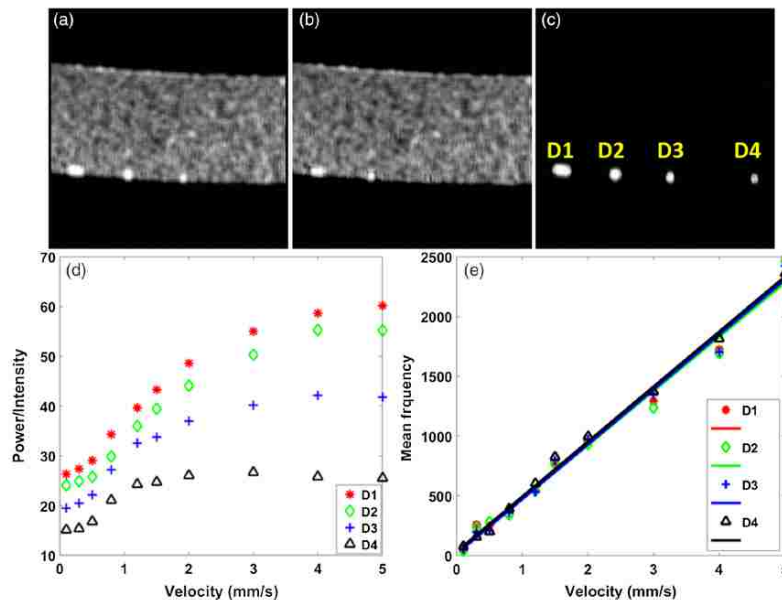


Figure 1.7. Validation of ED-based capillary velocimetry with microfluidic phantom.

The ED-algorithm is capable of measuring the mean flow velocity in the microfluidic channels. (a) The structure OCT image. (b) Static tissue signal image. (c) OCTA flow image of the scanned microfluidic phantom. (d) The relationship between velocity and OCTA signal power within four channels. (e) The relationship between velocity and MF for four channels. A same linear relationship between MF and velocity is found with squared Pearson's correlation coefficient of 0.983, 0.982, 0.970, and 0.920 from D1 to D4, respectively, among all given velocities (0~5 mm/s).

The result has indicated that the new ED-based OCTA velocimetry is able to measure accurately the velocities in capillaries with different sizes. Furthermore, this type of statistical analysis, with designated scanning protocol, is able to reveal a large quantity of capillary flow

signal (thousands) within seconds to one minute of data acquisition, which is extremely useful for applying to the functional brain activity study to reveal the microcirculatory dynamics during neurovascular coupling.

1.5 SCOPE OF THE THESIS

The objective of this thesis is to apply the aforementioned OCTA algorithms to perform cerebral blood flow imaging in mouse models and solve questions in neurovascular function and neurovascular diseases. To achieve so, firstly, novel mouse cranial window surgery techniques will be developed in Chapter 2 to prepare for the high-resolution OCTA imaging in the deeper cerebral vascular bed. Chapter 3 will centrally present the application of ED-based OCTA capillary velocimetry to study microcirculatory dynamics during flow-metabolism coupling. Following in Chapter 4, a new vascular protective mechanism during ischemic stroke is discovered with OMAG and DOMAG by analyzing pial and penetrating arteriole vasodynamics. In Chapter 5, the multi-functional OCTA will be applied for a comprehensive investigation of aging-associated cerebral vascular and blood flow changes that gives indications to Alzheimer's disease. The last chapter of the thesis will summarize and make a conclusion of the research, and propose future directions based on the achieved.

Chapter 2. DEVELOPING CRANIAL WINDOW TECHNIQUES TO IMAGE MOUSE CEREBRAL BLOOD FLOW WITH OCTA

2.1 BACKGROUND AND MOTIVATION

The cranial tissue scattering is one of the greatest obstacles faced by all optical imaging modalities in imaging the cerebral blood flow (CBF) *in vivo*, affecting the image resolution, light penetration, and the dynamic signal detection [29]. This problem must be solved in order to obtain quantifiable blood flow parameters in mouse brain with OCTA.

Two different types of mouse cranial window techniques have been previously developed by other studies: the traditional craniotomy, also known as the open-skull cranial window technique, in which part of the skull is removed and replaced with a glass coverslip [30]–[32], and the thinned-skull cranial window technique, in which a selected area of the skull is thinned to a desired thickness (typically 15 μm ~ 50 μm), with an optional placement of a glass coverslip on top of the thinned-skull for longitudinal imaging [33]–[35]. Although both techniques have shown promise in several studies using two-photon microscopy [31] to image deeper and better in the brain tissue, their practicality for OCTA imaging has not yet been evaluated [36], neither has there been a comparison of two cranial window types as to their impact on cerebral blood flow imaging.

In this first project of the thesis, I implemented and improved two types of mouse cranial window techniques for imaging mouse CBF using OCTA algorithms: OMAG and DOMAG. The ability of both types of cranial window in revealing detailed pial vessel networks and deeper blood flow will be compared to the intact skull. Additionally, procedural complexity, angiogram quality, and a vascular density quantification will be compared between two methods, upon which recommendations will be given to the future OCTA studies.

2.2 METHODS

2.2.1 *Animal models*

Three-month-old C57/BL6 mice (n=5) weighing 23 ~ 25 g were obtained from Charles River Laboratories. The mouse was deeply anesthetized using 1.5 ~ 2% isoflurane (0.2 L/min O₂, 0.8 L/min air) through a nose cone and placed on a stereotaxic frame and supported by a heating pad to maintain body temperature during the entire experiment. After checking on the toe-pinching reflexes, the skin covering the cranial bone were incised and retracted, and the periosteum was carefully removed. Then, a microscopic image of the exposed skull was taken (**Figure 2.1a**). The mouse was then transferred to the optical table for intact-skull imaging (see 2.2.3 for imaging protocol). Drops of saline were constantly applied onto the cranium surface to prevent it from drying and becoming opaque. After baseline imaging, animal was transferred back to the surgical platform and two types of cranial window procedures are performed on each side of parietal bone (see 2.2.2 for cranial window techniques). After the surgery, another microscopic image was taken to compare the cortical tissue transparency to the prior taken intact skull (**Figure 2.1b**). Lastly, the two cranial windows on the same animal were subjected to optical imaging following the same protocol (see 2.2.3).

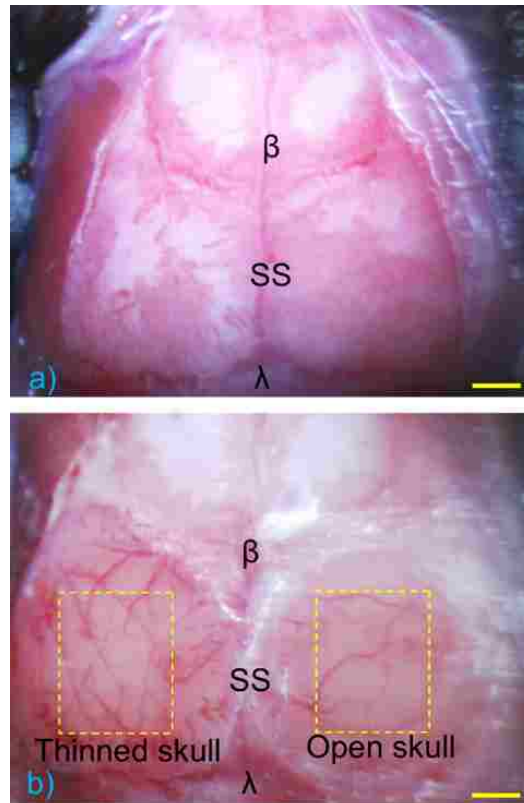


Figure 2.1. Microscopic images of intact skull and cranial windows.

(a) Intact skull showing bregma (β), lambda (λ), and sagittal suture (SS). (b) Left: Thinned-skull window with 4x4 mm available imaging area. Right: Open-skull cranial window with 3x3 mm available imaging area. Scale bar represents 1 mm.

2.2.2 Cranial window techniques

Before starting cranial window procedures, dexamethasone sodium phosphate (0.02 ml at 4 mg/ml; $\sim 2\mu\text{g/g}$ dexamethasone) was administered subcutaneously to prevent cerebral inflammation and swelling/edema. The cranial surface was cleaned and dried with sterile saline and cotton swabs. Then, a drop of 1% Xylocaine (Lidocaine 1% + epinephrine 1:100,000 solution) is applied directly onto the skull to minimize the pain and bleeding from the procedure.

In preparation of the thinned-skull window, a selected area (4x4 mm) on the left parietal bone ~ 1.5 posterior and lateral to bregma was located. The thinning was performed by a high-speed

surgical hand drill (Foredom Electric Co., Ethel, CT, USA) with a round carbide bur (0.75 mm), followed by a green stone bur (Shofu Dental Corp., San Marcos, CA, USA). The skull was constantly wetted with sterile saline to remove the bone dust and to prevent overheating. When the thickness of the skull reaches $\sim 30 \mu\text{m}$ with the pial vessels clearly visible through wetted bone, a polishing step was followed. The skull was sequentially polished with size 3F grit followed by size 4F grit (Convington Engineering, Redlands, CA, USA). A slurry of grid and saline was agitated with a custom-made silicone coated drill bit. The polished skull was finally washed with sterile saline and the remaining bone dust are picked up by saline-soaked gelfoam.

For the open-skull cranial window, a circular piece of skull (4x4 mm) at the region of interest ~ 1.5 posterior and lateral to bregma was removed and replaced with a round coverglass (Thermo Scientific, Waltham, MA, USA). To do so, a circular groove was first thinned with a shaft drill (Foredom Electric Co., Ethel, CT, USA). The groove was drilled slowly, and saline was applied regularly to avoid heating. In the end, the central island of skull bone was lifted and removed with help of saline and replaced with a circular coverglass and sealed with cyanoacrylate glue, leaving the available imaging area with $\sim 3 \times 3$ mm.

2.2.3 *Imaging protocol*

To visualize the volumetric cerebral microvasculature through the intact skull and through the cranial windows, OMAG scanning protocol was applied. Each B-frame consists of 400 A-lines covering a distance of ~ 2.0 mm. The imaging rate was 180 fps. In the slow axis (C-scan), a total number of 2000 of B-frames with 5 repetitions in each location were performed also covering a distance of ~ 2 mm. Hence the data cube of each 3D image was composed of 1024 by 400 by 400 (z-x-y) voxels, which took ~ 11 s to acquire.

After OMAG scans, DOMAG was performed covering the same area to map the axial velocity of CBF. Each B-scan in DOMAG protocol consisted of 10000 A-lines by acquiring 25 A-lines at each 400 discrete steps. In the C-scan direction, there were 300 discrete positions. During the Doppler phase calculation, 3 A-lines were skipped during to increase the time interval between the used A-lines, which gives an axial velocity range of ± 6.1 mm/s. The data cube of each 3D image (C-scan) was composed of 1024 by 400 by 300 (z-x-y) voxels, which took ~ 100 s to acquire with 6 fps imaging speed.

To acquire the images that over a large area of the cortex, the scans were repeated to create a mosaic image.

2.3 RESULTS

The volumetric OMAG maximum intensity projection (MIP) result of pial network in mouse brain is presented in **Figure 2.2**, corresponding to the yellow dashed area in the microscopic image (**Figure 2.1b**). The pial collateral network play an important role in CBF regulation. Hence, the microcirculation at up to 200 μ m depth was targeted, which was arranged to cover the depth of focus of the lens. The final image, representing the CBF over the mouse cortex in the area of interest, was obtained by stitching and cropping 4 images together, for each side of the parietal bone. This procedure was applied both to baseline with intact skull (**Figure 2.2a** and **Figure 2.2b**) and to two cranial window cases (**Figure 2.2c** and **Figure 2.2d**) to compare the visible vessel density changes regarding to two different window opening methods.

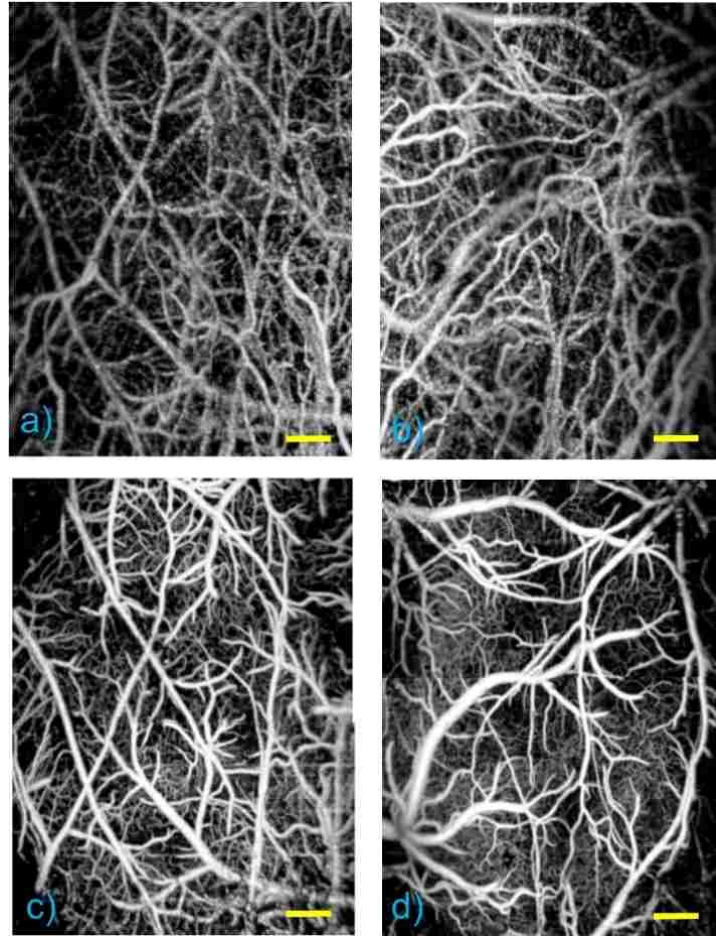


Figure 2.2. OMAG MIP of microcirculation network up to ~1 mm depth.

(a) and (b) With intact skull (baseline). (c) With thinned-skull cranial window. (d) With open-skull cranial window. Scale bar represents 0.4 mm.

To identify the location of the blood vessels and to determine the remaining thickness of the thinned-skull, OMAG images were merged with structural OCT images for both before and after cranial windows. **Figure 2.3** presents maximum projection view of OMAG images of intact skull (**Figure 2.3a**), thinned-skull (**Figure 2.3b**) and open-skull cranial windows (**Figure 2.3c**). Moreover, the cross-sectional blood perfusion and structural images corresponding to the positions marked

by the dash yellow lines are presented in **Figure 2.3d-f** and **Figure 2.3g-i**, respectively. From the cross-sectional structural images, the remaining thickness of the skull was estimated at $\sim 20\text{-}30\ \mu\text{m}$.

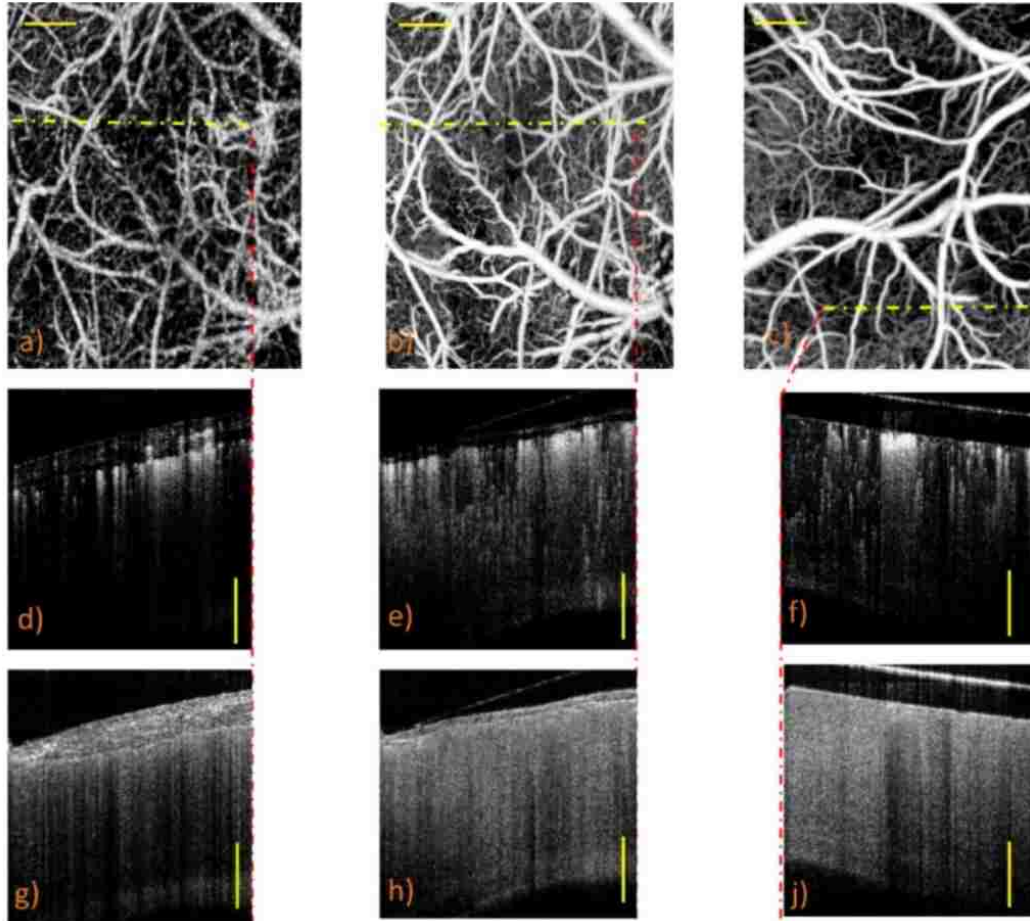


Figure 2.3. Cross-sectional view of the flow and structure images.

(a) Before cranial windows (baseline). (b) After thinned-skull cranial window. (d)-(f) The blood perfusion images of the cross-sections located at dotted yellow lines. (g)-(i) The structural images of the same cross-sections. Scale bar represents 0.4 mm.

Furthermore, the same area was imaged using DOMAG protocol to obtain CBF axial velocity mapping. The bidirectional *en face* MIP images in **Figure 2.4** show the penetrating and rising vessels as green and red signals, respectively, where RBC axial velocity information is coded with a color bar in a range of $\pm 6.1\ \text{mm/s}$. The penetrating arterioles and rising venules appear as vivid

green and red isolated spots. This is because their flow directions are mainly parallel to the beam axis, giving their axial velocity large enough to be detected at this range. However, the surface vessels connected to them, whose flow nearly perpendicularly to the probe beam, escaped the detection due to their small axial velocity. Few out-of-range flows are also observed as phase-wrapped signals, seen as yellow color (combination of red and green). For the intact-skull case, although the bigger vessels can be visualized, the penetrating arterioles or rising venules are harder to detect as seen in **Figure 2.4e** and **Figure 2.2f**. On the other hand, **Figure 2.4g** and **Figure 2.2h** shows that both types of cranial windows provide better visualization of the penetrating arterioles and rising venules. Furthermore, similar to the OMAG in **Figure 2.2** and **Figure 2.3**, thinned-skull cranial window provides larger imaging area with visibility of more blood vessels.

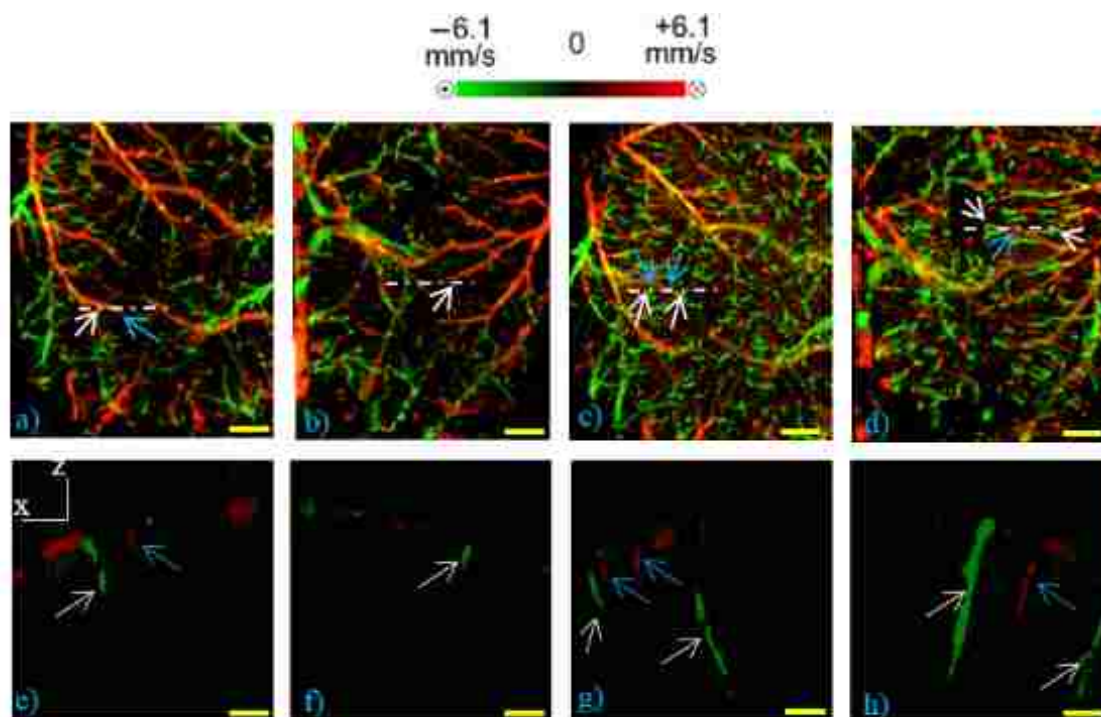


Figure 2.4. DOMAG MIP view of microcirculation network at 50 ~ 450 μ m depth.

(a-b) Shows baseline before the application of cranial windows to intact skull. (c) With thinned-skull cranial window (d) With open-skull cranial window. The white dashed lines represent the location of the

cross-sectional views (along x-z planes) shown in (e-h). White arrows point the diving arterioles and blue arrows point the rising venules. Scale bar represents 0.5 mm in (a-d) and represent 0.15 mm in (e-h).

To quantitatively evaluate the effect of cranial window procedures on *in vivo* blood perfusion imaging, vessel density of images resulted from each type of windows was calculated. To do so, firstly, a same-sized region was selected from both before and after craniotomy and registered using the function, `imregister`, available in MATLAB[®]. Then, registered images were segmented for the blood vessels by creating a binary black and white image with an adaptive threshold technique specifically designed for OMAG blood flow images. Briefly in this method, first, a low-pass filter was used to minimize the elements that are smaller than a specific radius size. Then, a global threshold was used to set to zero all the pixels below a certain threshold. Finally, a local adaptive threshold was implemented to binarize the image based on the mean pixel value within a predefined window size. The vessel density was calculated by dividing the number of ones with the total pixel number. **Figure 2.5** shows the mean vessel density of n=5 animals with intact skull (baseline) and two types of cranial windows. The results indicate that as compared to baselines, both types of cranial window have improved the measured vessel density significantly. The thinned-skull cranial window provides 60% more vascular details compare to baseline case, and the open skull cranial window gives 45% more details, in average.

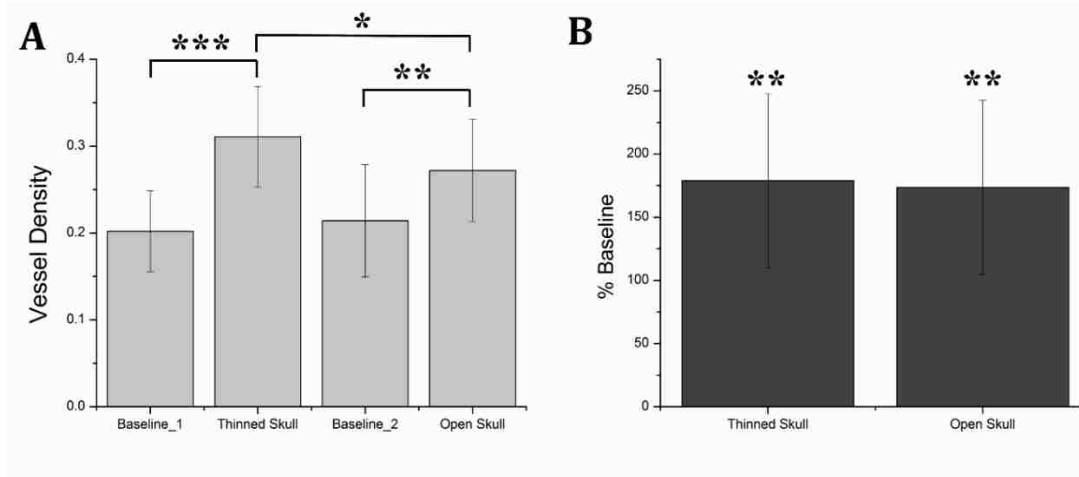


Figure 2.5. Comparison of detectable vessel density for n=5.

Box borders show the standard deviation, while lines show the middle value and white boxes present the mean value.

2.4 DISCUSSION

In this study, we demonstrated the feasibility of OMAG in cerebral blood flow imaging through cranial windows in mice *in vivo*. The results also revealed that both types of cranial window improve the imaging quality and provides higher detected cerebral vessel density. Both thinned-skull and open-skull windows can enhance the optical penetration depths of ~1 mm below the cortical surface in OMAG imaging, but thinned-skull procedure results in larger available imaging area, which could be useful for a comprehensive assessment of pial collateral network (e.g. one or more anastomosis between major cerebral arteries) in stroke studies. In an open-skull cranial window preparation, craniotomy must be carefully performed to avoid damaging the blood vessels at the sagittal sutures, which usually results in smaller window and available imaging area. In our experience, additionally, the use of glue and dental cement around the coverglass edge in the open-skull window can further deteriorates the available imaging area. As a result, in most cases, a

thinned-skull technique creates a larger imaging window of $\sim 4 \times 4$ mm compare to an open-skull window available imaging size of $\sim 3 \times 3$ mm. It is also noted that both cranial window techniques developed in this study were to image much larger cortical area than previously applied in TPM ($\sim 1 \times 1$ mm).

Although both cranial window methods enhance imaging depth and quality for OMAG, they both bring certain invasiveness to the cerebral blood flow conditions. In the open-skull cranial window procedure, cerebral inflammation/edema may be induced by craniotomy. Although efforts have been made to suppress the effect of inflammation, such as administering dexamethasone, the procedure will still cause mild dura swelling. The effect of such inflammatory response to blood flow dynamics remains to be investigated. On the other hand, thinned-skull cranial window has preserved the integrity of the cranium, which is considered as the less invasive option. During the skull thinning, however, subdural bleeding may occur due to unexperienced operation. Care and training should be given to avoid such.

An advantage of the thinned-skull over the open-skull method is the procedural efficiency. From our experience, thinned-skull method requires less surgical time (~ 15 min) compared to the open-skull cranial window (~ 30 min). Since the thinned-skull method does not require a craniotomy, the training curve to master this procedure is much shorter than the open-skull craniotomy for a beginner.

There is a significant limitation for the thinned-skull cranial window as well. For longer duration imaging, even longer than 30 min, the remaining thinned layer of skull tissue will start to become opaque quickly. The thinning and polishing steps need to sometimes be repeated for multiple imaging sessions, such as baseline, stroke, reperfusion, etc. For a short term, a plastic

food wrap can help with this issue by keeping the thinned-skull window wet to preserve cranial tissue clarity, but the open-skull cranial window gives the most robust imaging quality among multiple imaging sessions. Alternatively, a polished and reinforced thinned skull [34] may be considered, which uses a coverglass glued onto the thinned cranium to create an imaging window, but this operation will result in a smaller available imaging area, similar to the idea of an open-skull cranial window.

2.5 UPDATES

Since the initial application of cranial window techniques to OMAG imaging in 2014 [37], many improvements have been made to the surgical procedure and image scanning skills. **Figure 2.6** shows an update on OMAG image quality with an open-skull cranial window. The blood flow signals are falsely color-coded according to their depth to the cortical surface. Pial vasculature is visualized in red, immediately deeper followed by green, while capillary network is revealed in blue color. Currently, this large-area (4x4 mm) open-skull cranial windows are performed in the lab at daily basis, and used with multi-functional OCTA algorithms for many neurovascular applications. The cranial window techniques have greatly benefited our imaging study with mouse models and have made the applications in the following chapters possible.

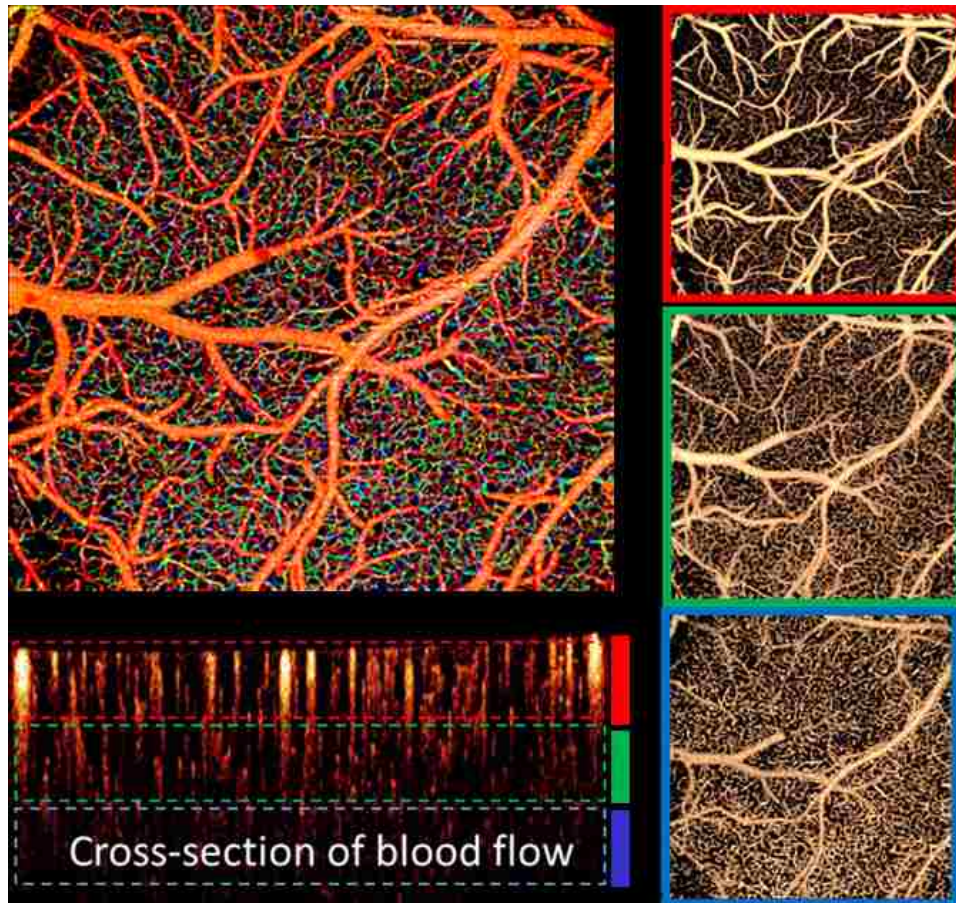


Figure 2.6. Depth color coded OMAG MIP of microcirculation network.

Colors represent blood flow at depths of 0~100 μm (red), 100~200 μm (green), and 200~300 μm (blue).

Chapter 3. CAPILLARY FLOW HOMOGENIZATION DURING FUNCTIONAL ACTIVATION REVEALED BY OCTA BASED CAPILLARY VELOCIMETRY

3.1 BACKGROUND AND MOTIVATION

Normal brain function depends on the regulation of oxygen supply through bloodstream to support the actively changing metabolic needs [2]. The temporal and spatial relationship between neuronal activity and cerebral blood flow (CBF), termed neurovascular coupling [38], has been utilized and studied in functional magnetic resonance imaging (fMRI) [39]–[41]. Specifically, the hemodynamic response during neurovascular coupling has been observed in fMRI as localized increase of CBF exceeding that of cerebral metabolic rate of oxygen ($CMRO_2$) [42], giving rise to a lower deoxyhemoglobin concentration in brain tissue and hence blood oxygen level dependent (BOLD) signal contrast for functional brain mapping [43]–[45]. Despite decades of effort in analyzing the functional relationship between CBF and brain oxygenation, our understanding of such flow-metabolism coupling remains incomplete. The disproportionate elevation of CBF in comparison to the relatively increased $CMRO_2$ [46], [47], particularly, suggests an involvement of additional factors in the non-linear coupling between oxygen consumption and the extent of hyperemia [48].

Recently, Jespersen & Østergaard [49] have revisited the flow-diffusion function of oxygen, taking into account of the heterogeneous distribution of the red blood cells (RBC) transit times across capillary bed, to evaluate oxygen extraction in cerebral tissue. Accordingly, they have modeled the combined effects of CBF and capillary transit time heterogeneity (CTTH) on the maximum oxygen extraction fraction (OEF^{\max}). Briefly in this elegant theoretical model [49] (**Figure 3.1**), the hemodynamic contribution to OEF^{\max} is determined by both vascular mean

transit time (MTT), which is inversely related to CBF according to central volume theorem [50], and CTTH, which is quantified as the standard deviation of the RBC transit time distribution across capillary bed. During functional activation, the inherent reduction of OEF due to the initial CBF increase is counteracted by capillary transit time homogenization, hence CTTH reduction, which would secure sufficient oxygenation during the subsequent (or simultaneous) episodes of hyperemia to meet the increased metabolic demand of oxygen in the activated tissue bed. This model has provided biophysical support to the disproportionate increase in CBF seen in functional activation, and established a framework for the quantitative characterization of capillary flow adjustment in neurovascular coupling.

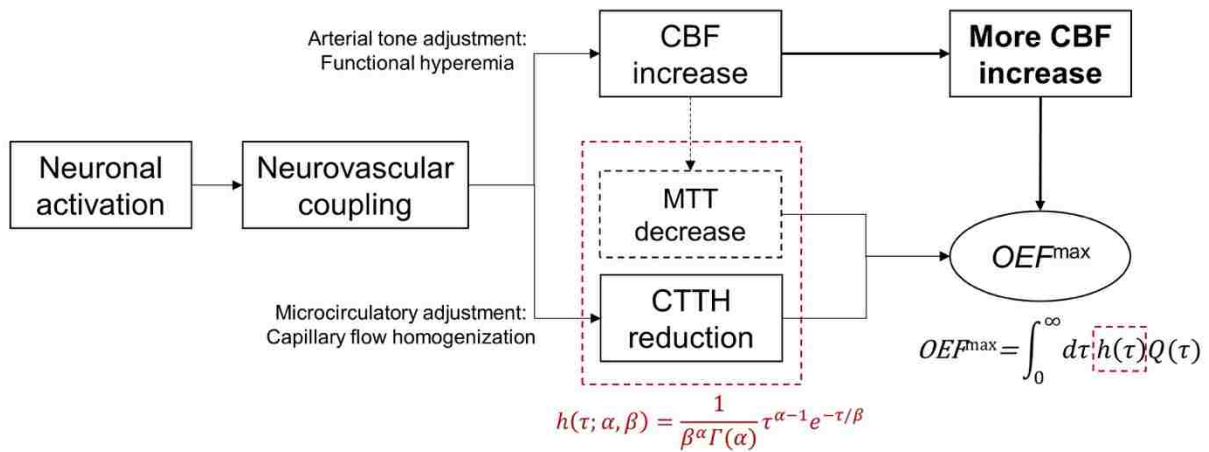


Figure 3.1. Schematics of the Jespersen and Østergaard model of CTTH and MTT

The upper thread refers to arterial tone adjustment in neurovascular coupling during functional activation, representing as functional hyperemia in observation with excessive increase of CBF (relative to the increase of $CMRO_2$). The lower thread represents microcirculatory adjustment during functional activation involving capillary flow homogenization. In this work, capillary flow dynamics are modeled with capillary transit time τ distribution in gamma function $h(\tau)$, where MTT is determined by the mean $\alpha\beta$ of the gamma function and CTTH is determined by the standard deviation $\sqrt{\alpha}\beta$. The OEF of the entire capillary bed is calculated from a single capillary contribution $Q(\tau)$ weighted by distribution $h(\tau)$. During cortical activation, assuming $CBV' = CBF \cdot MTT$ is constant according to the central volume theorem, the inherent reduction of OEF due to decreased MTT must be accompanied by CTTH reduction (capillary homogenization) in order to secure adequate level of oxygenation to achieve OEF^{\max} during functional hyperemia.

The *in vivo* imaging of capillary flow dynamics and the validation of CTTH hypothesis have challenged the current microscopic neuroimaging techniques. Bolus tracking techniques with high resolution two-photon microscopy (TPM) [51] or confocal laser scanning fluorescence microscopy [52] have been previously used to estimate MTT and CTTH in rodent brains, based on measurements of a bolus plasma dye passage through cortical vasculature. Due to the incapability of direct imaging of RBC in single capillary vessels, however, spatial distribution of RBC transit times at capillary bed was unobtainable for an accurate CTTH evaluation [53]. Alternatively, single-line scanning velocimetry using TPM measures RBC speed directly in individual capillary passages [54]. Despite of a promising results of capillary velocity and flux quantification using line-scanning velocimetry in steady-state brain [55], the technique is limited in its data acquisition speed (hours) [56], as well as in an inadequate sampling size (<100 capillaries) [55] for CTTH assessment with sufficient statistical power. Optical coherence tomography angiography (OCTA) has enabled three-dimension (3-D) quantitative imaging of blood flow in cerebral arteries and veins [57], as well as visualization of the microvasculature at capillary level by analyzing the dynamic scattering signals embedded within the tissue volume [17]. As OCTA obtains flow information over a generally large focal depth [56] in cerebral tissue together with micron-scale resolution [58], the limitations in line-scanning TPM can be potentially lifted by imaging a larger amount (hundreds to thousands) of capillaries in 3-D space within tens of seconds [59]. Nevertheless, the accurate characterization of capillary flow speeds with sufficiently high statistical power remains a challenge for the use of current OCTA technique to investigate hemodynamic responses during cortical activities. In a recent study, Lee et al. have developed and applied statistical intensity variation analysis with OCTA for tracing changes in RBC flux over hundreds of capillaries within ~ 1 s [60]. Using such high-throughput monitoring of RBC flux

dynamics, they have revealed capillary flux homogenization in rat somatosensory cortex during forepaw electrical stimulation, which showed the potential OCTA based techniques to study microcirculatory dynamics during neural activation.

Recently, based on OCTA, we have developed a statistical method of eigen-decomposition (ED) analysis [27] to extract the frequency components of dynamic capillary flow from the coherent optical signals generated in high-speed OCT scans. The preliminary results have indicated a linear relationship between the measured mean frequency (MF) and the mean RBC velocity in individual capillary passages. The method has been successfully applied to quantify capillary flow parameters in mice by measuring thousands of capillaries in one volumetric dataset with 50 μ s temporal resolution, which revealed MTT and CTTH differences in mouse somatosensory cortex before and after ischemic stroke insult [27].

In this project, we applied this novel approach of ED analysis with OCTA to study the microcirculatory adjustment during stimulus-evoked cortical activation. Guided with the oxygenation mapping using laser speckle contrast imaging (LSCI) [61], we performed OCTA velocimetry scans at both activated and non-activated cortex based on oxygen consumption, and correlated, for the first time, capillary flow responses to oxygen metabolism signal. We aimed to utilize the statistical powered OCTA results to validate, *in vivo*, the local CTTH reduction during functional hyperemia proposed in previous modeling study.

3.2 MATERIAL AND METHODS

3.2.1 *Animal preparation*

All animal experimental procedure in this study were approved by the Institutional Animal Care and Use Committee (IACUC) of the University of Washington and conducted in accordance with University of Washington guidelines and ARRIVE guidelines.

C57BL/6 mice (Charles River Laboratories, n=12, 3-month-old, 23-25 g) were used under isoflurane anesthesia with a mixture of 0.2 L/min pure oxygen and 0.8 L/min air. Physiological parameters were monitored, including adequate anesthesia depth (no hindpaw reflexes), blood pressure, heart rate, and body temperature ($36.8 \pm 0.2^\circ\text{C}$) throughout all experimental procedures. Cranial window procedures were conducted similar to that described previously by Li et al [37].

3.2.2 *Hindpaw electrical stimulation and laser speckle contrast imaging (LSCI)*

Two 30-gauge needles inserted into the plantar surface of the mouse hindpaw, contralateral body side to cranial window, were connected to +/- outputs of a square pulse stimulator (SD9, Grass Instruments Medical) to deliver square wave voltage pulses [59]. A $4.1\text{k}\Omega$ resistor was connected between the return electrode needle and the machine output to identify the stimulus current, which was calculated with a peak voltage applied to the resistor detected on a digital oscilloscope. Each trial of stimulation consists of 20 min resting time before 30 s stimulation with an amplitude of 2 mA in 0.3 ms duration repeated at 3 Hz. Each animal received 3 trials of electrical stimulation. The first trial was performed under LSCI imaging to localize oxygenation signal at HLS1 during stimulation. Briefly in this imaging method, a differential model [61], based on the difference in absorption between two wavelengths, was used to estimate the changes in oxy- (ΔHbO) or deoxyhemoglobin (ΔHb), and the concentration changes of Hb was mapped where Hb of $40\ \mu\text{M}$ in the resting brain was assumed [5]. The other two trials of stimulation were performed for OCTA velocimetry scans, one at HLS1 region, and the other at a non-activated control region (CTRL) identified from LSCI oxygenation mapping.

3.2.3 *OCTA imaging*

OCT angiograms and capillary velocity mapping were obtained using an in-house spectral-domain OCT (SD-OCT) system [62]. Briefly, the system was equipped with a broadband superluminescent diode (SLD) light source (LS2000B, Thorlabs Inc.) with a center wavelength of 1340 nm and a spectral bandwidth of 110 nm, giving an axial resolution of $\sim 6 \mu\text{m}$ in tissue. A $10\times$ objective lens was used to focus the light into the brain subsurface cortex of the animal, providing a lateral resolution of $\sim 10 \mu\text{m}$. Details of the system configuration can be found in [24].

Typical cerebral angiogram within the cranial window ($4\times 4 \text{ mm}$) was first produced in resting-state brain using traditional optical microangiography (OMAG) protocol, where 400 A-lines in the depth axis (z) was acquired within each B-scan at A-line rate of 92 kHz, and 8 repeated B-scans were performed at each of the 400 cross-sectional locations (z - x).

OCTA capillary velocimetry was then performed at HLS1 and CTRL cortex by simply targeting the designated cortex regions identified by the LSCI oxygenation maps. Prior to stimulation, capillary velocimetry scans at two regions were acquired during resting-state, then scans were performed during trials of electrical stimulation. The OCTA velocimetry scanning protocol [27] consists of 50 repeated A-lines at each spatial position, i.e. M-scan, at a rate of 20 kHz (time interval $50 \mu\text{s}$ between successive scans). A total of 200 positions within each B-scan (x) and 100 spatial locations (i.e. B-scans) in the slow axis (y) were completed within 75 s, covering a region of $1.5\times 0.75 \text{ mm}$ (x - y) with a uniform transverse sampling of $7.5 \mu\text{m}/\text{pixel}$. Electrical stimulation was incorporated within the first 30 s of the volume scans.

3.2.4 *Capillary velocity analysis*

ED-based capillary velocimetry analysis was performed based on repeated 50 A-scans acquired. Details of the velocimetry analysis is demonstrated in our previous publication²⁶. Briefly,

frequency analyses were firstly conducted using the covariance matrix of grouped A-lines (50 repetitions), with which the eigenvalues and eigenvectors that represent the subsets of the signal markup were calculated. The eigen values and vectors that are due to moving RBC were isolated via an adaptive regression filter to remove the eigencomponents that represent static tissue. And then the mean frequency (MF) of moving RBC were calculated through first lag-one autocorrelation of the obtained eigenvectors. According to Wang et al. [27], the measured MF is linearly related to the mean RBC velocity in single-file passages as verified by a phantom experiment. All MF values in the 3-D space within the scanned tissue bed are used for calculating capillary flow parameters, including mean and spatial distribution of transit time.

3.2.5 *Capillary flow parameter evaluation*

All MF values were converted to velocities based on linear function [27], and the mean of all RBC velocities within 3-D space of each dataset is represented with mean transit velocity (MTV). For MTT and CTTH measurements in the capillary bed, however, transit time of the RBC must be resolved. In doing so, we simply adopted the method in the modeling study [49] with assumption of a uniform capillary path length $L=400 \mu\text{m}$ to convert velocity to time. After obtaining the RBC transit times from velocities, the values in each 3-D dataset were plotted into a histogram distribution. To validate MTT and CTTH change with the modeled transit time function, where capillary transit time distribution is expressed in gamma function of τ modulated by shape and scale parameters of α and β in equation :

$$h(\tau; \alpha, \beta) = \frac{1}{\beta^\alpha \Gamma(\alpha)} \tau^{\alpha-1} e^{-\tau/\beta} \quad (3.10)$$

we fitted our data points on the transit time distribution to a gamma function curve to derive MTT from $\alpha\beta$ and the standard deviation CTTH from $\sqrt{\alpha\beta}$. These values and their alterations are then compared between rest and stimulation, HLS1 and CTRL, respectively.

3.2.6 *Statistical analysis*

All capillary flow parameters are expressed as mean \pm std. (n=12). The relative change in the hemodynamic parameters, such as Δ MTV, Δ MTT, and Δ CTTH, from rest to stimulation were statistically tested using Student *t-test* (two-tailed) between HLS1 and CTRL. $P < 0.05$ was considered significant.

3.3 RESULTS

3.3.1 *Activation at HLS1 upon hindpaw electrical stimulation*

Spatial relationship between the cranial window and mouse primary somatosensory cortex, including both forelimb (FLS1) and hindlimb (HLS1), was identified using the method described in previous study [63] and demonstrated on the microscopic image of mouse intact skull before cranial window surgery (**Figure 3.2a**). To precisely locate the HLS1, LSCI imaging was performed at the cranial window during rest (**Figure 3.2b**) and hindpaw electrical stimulation (**Figure 3.2c**). Localized increase of Δ Hb were observed during stimulation, indicating an increased utilization of oxygen at the HLS1 (shown as warmer color in **Figure 3.2c**). The oxygenation mapping validated stimulus-evoked activation at HLS1 and provided guidance for the investigation of localized changes in capillary flow pattern in the following experiments.

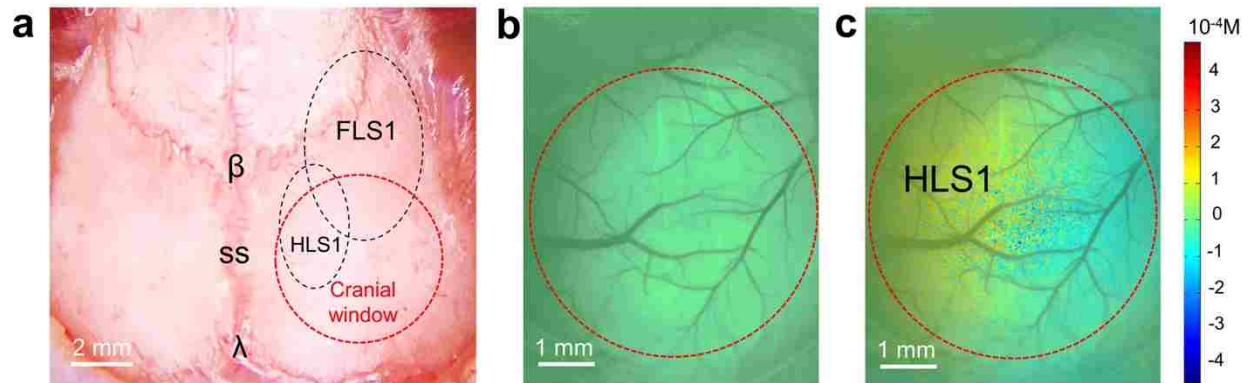


Figure 3.2. Oxygenation mapping during functional activation

(a) Light microscopic image giving the relative location of cranial window to the FLS1 and HLS1. Red dashed circle shows the location of cranial window to be created, 1 mm posterior and lateral to bregma. Black dashed regions indicate the approximate locations of HLS1 and FLS1 [63]. (b) and (c) ΔHb during rest and stimulation, respectively, overlaid with arterial angiogram inside the cranial window. Color bar represents Hb concentration differences in μM . The region shown with warmer color in (c) corresponds to a higher ΔHb level; thus, indicating oxygen consumption at the HLS1 region during functional activation. β , bregma; λ , lambda; SS, sagittal suture; FLS1, forelimb somatosensory cortex; HLS1, hindlimb somatosensory cortex.

3.3.2 OCTA angiogram and velocimetry at HLS1 and CTRL

Cerebral angiogram inside the cranial window was obtained from x-y *en face* maximum projection (MIP) of the volumetric 3-D OMAG dataset (**Figure 3.3a**). Within 300 μm thick slab from the cortical surface, the depth locations of vessel in axial space (z) are visualized with colors. Red, green, and blue represents vessels from surface pial vessels to deeper capillary vessels, respectively, with each color occupying a 100- μm thick slab as measured from the cortical surface (identified from 3D OCT structural image). Guided with oxygenation mapping obtained from LSCI, a cortical region with increased oxygenation, HLS1, and non-activated region, CTRL, were selected for velocimetry scans during rest and trials of stimulation. MF maps from the 3-D velocimetry scans are displayed with x-y *en face* average intensity projection (AIP) for HLS1 during rest (**Figure 3.3b**) and stimulation (**Figure 3.3c**), and for CTRL during rest (**Figure 3.3d**) and

stimulation (**Figure 3.3e**). In these maps, each signal points represent an MF analyzed from dynamic RBC movement, with the MF value (Hz) indicated on the color bar. In each of the four maps, >20,000 MF signals were obtained from the 3-D space within 300 μm thick slab from the cortical surface.

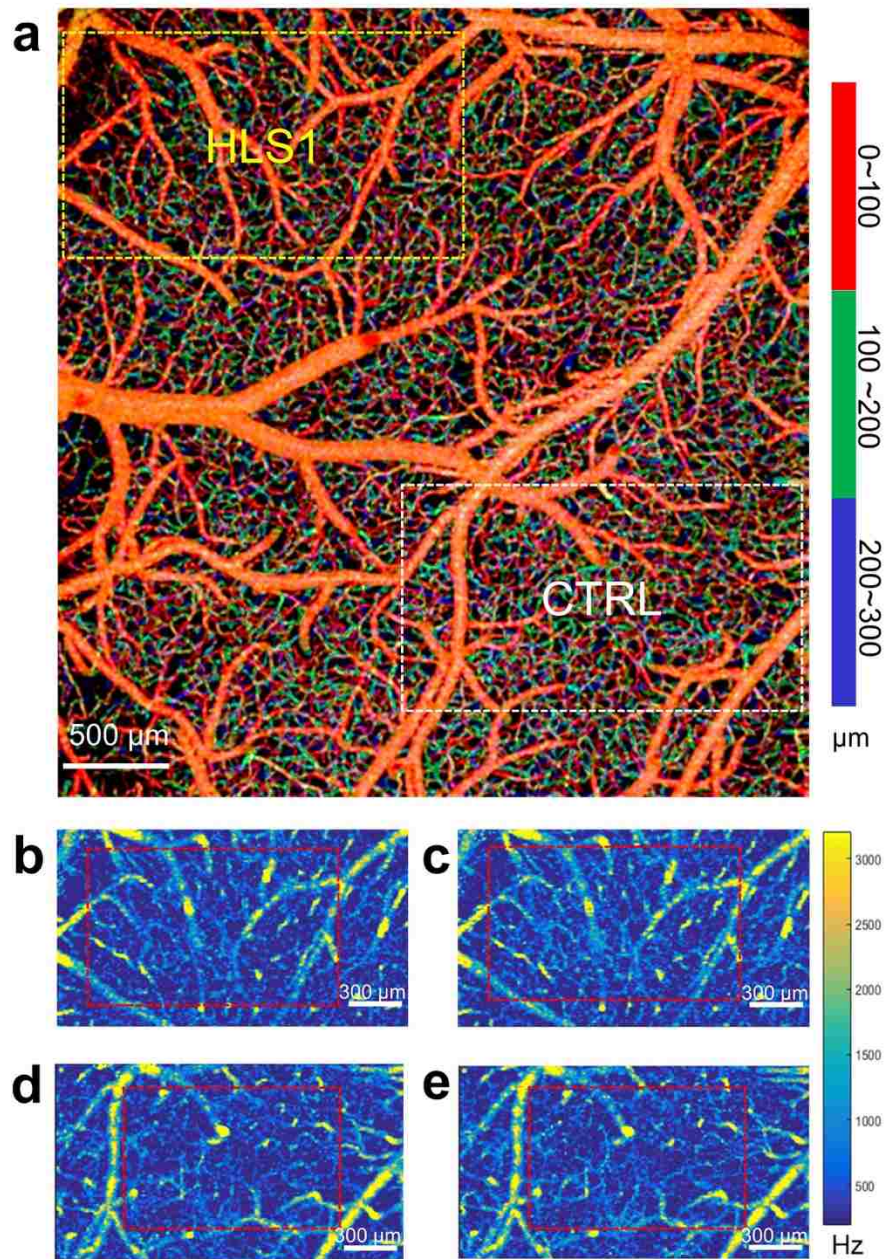


Figure 3.3. Cerebral angiogram and capillary velocity maps

(a) *En face* maximum intensity projection (MIP) of the 3-D OMAG dataset inside the cranial window within 300 μm depth from the cortical surface. Colors represent vessels at depths of 0~100 μm (red), 100~200 μm (green), and 200~300 μm (blue). Dashed squares indicate regions where OCTA velocimetry scans were performed. The yellow square encloses the vascular bed inside activation center (HLS1) as indicated by previous ΔHb maps, and the white square marks a control region (CTRL) further away from the activation center with no noticeable oxygenation consumption change. *En face* average intensity projection (AIP) images of the 3-D MF maps are shown within 300 μm thick slab from the cortical surface for HLS1 during (b) rest and (c) stimulation, and for CTRL during (d) rest and (e) stimulation. Color bar represents MF values. The red dashed squares indicate the regions selected for velocity distribution analysis, avoid including large pial arterioles.

3.3.3 *Capillary transit time distribution change and CTTH reduction at HLS1*

Spatial distributions of MF and transit times were evaluated at HLS1 during rest and upon electrical stimulation. For more accurate evaluation of capillary flow dynamics, additional segmentation was performed to remove MF signals in larger vessels with a diameter of $>15 \mu\text{m}$, and MF *en face* projection maps after segmentation are shown for rest and stimulation (**Figure 3.4a**). The MF values from these two mapping areas are plotted into a histogram distribution with white bars represent rest and black bars represent stimulation (**Figure 3.4b**). Differentiation of the two distributions were performed (**Figure 3.4d**), indicating that the RBC velocity in most of the capillaries are statistically shifting to slow velocity, with the counts of faster flow velocity becoming less. Capillary transit time were converted from MF-derived velocity, and plotted into histogram distribution as well (**Figure 3.4c**). The differentiation between the rest and stimulation indicates that the transit times are statistically shifting to lower value during stimulation, while the counts of longer transit time become decreased (**Figure 3.4e**). To derive MTT and CTTH values [49], we fitted two histograms into gamma function curves (**Figure 3.4f**) and calculated the MTT by $\alpha\beta$ and the CTTH by $\sqrt{\alpha}\beta$. From measuring the relative changes in these quantities at HLS1 from 12 animals, we have observed $9.8\% \pm 2.2$ reduction of MTT and $5.9\% \pm 1.4$ reduction of CTTH from rest to stimulation.

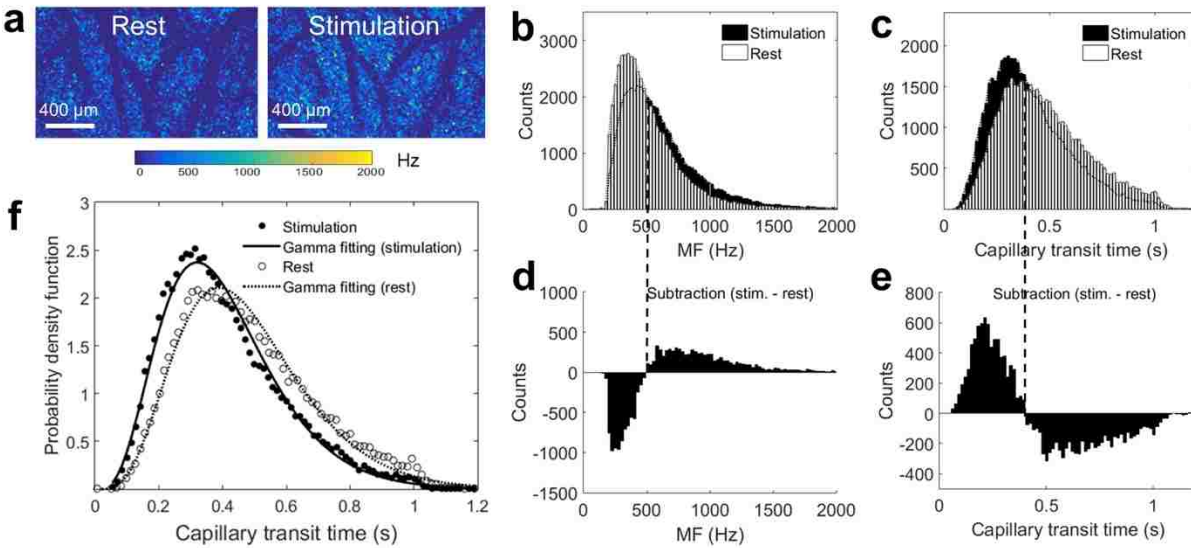


Figure 3.4. Capillary transit time distribution at HLS1

(a) MF maps shown are AIP from 3-D datasets within 300 μm thick slab from the cortical surface after removal of larger surface arterioles (>15 μm) during rest and stimulation. (b) Histogram distributions of MFs obtained from rest and stimulation. (c) Histogram distribution of capillary transit time during rest and stimulation. (d) The differentiation between the histogram functions in (b). (e) The differentiation between the histogram functions in (c). Black dashed lines mark the switch between positive and negative values from differentiations. (f) Gamma function fitting for the capillary transit time distribution in (c). The coefficient of determination in the fittings are $R^2=0.9873$ for rest (dashed line) and 0.9811 for stimulation (solid line).

3.3.4 Capillary transit time distribution at control region

Capillary flow distribution change at CTRL are also demonstrated. MF *en face* projection maps after segmentation are shown for rest and stimulation (**Figure 3.5a**). From the histogram distribution of MF (**Figure 3.5b**) and transit time (**Figure 3.5c**), the differentiation between rest and stimulation (**Figure 3.5d** and **Figure 3.5e**), as well as the nearly overlapping gamma function curves (**Figure 3.5f**), one can conclude a non-significant change in capillary flow pattern during hindpaw electrical stimulation. Such observation was consistent in the non-activated region from 12 animals.

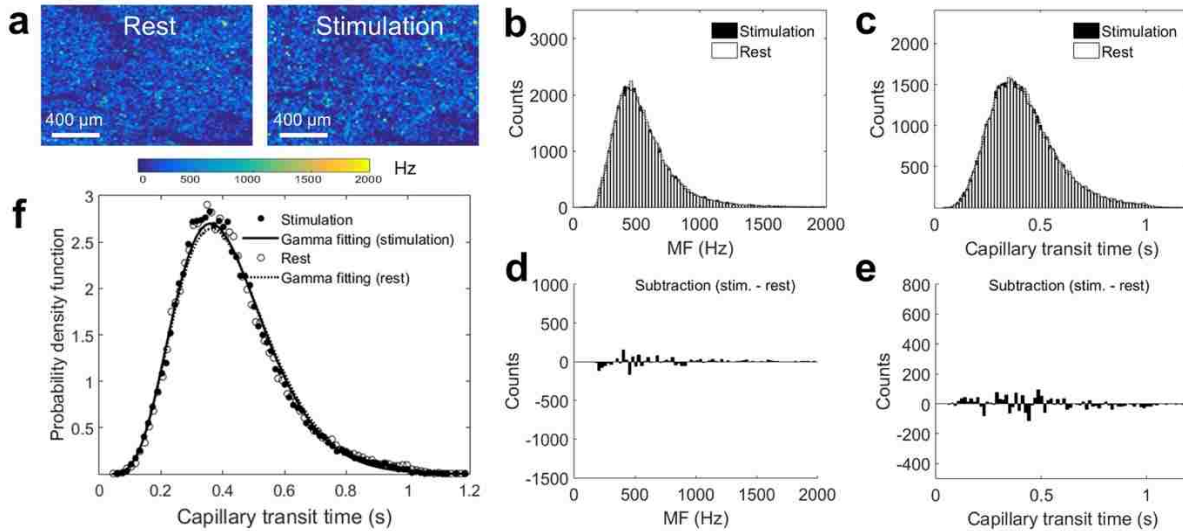


Figure 3.5. Capillary transit time distribution at control region

(a) MF maps at CTRL region are shown for rest and stimulation. (b) and (c) are histogram distributions of MF and capillary transit time, respectively. The differentiation between the histogram functions from rest to stimulation are shown for (d) MF and (e) transit time. Differences are not obvious between the probability of rest and stimulation, and no clear switch were identified from negative to positive values. (f) Gamma function fitting for the capillary transit time distribution where $R^2=0.9796$ and 0.9922 for rest and stimulation, respectively.

3.3.5 Hemodynamic parameter changes upon stimulation at HLS1 and CTRL

The relative changes (rest to stimulation) of hemodynamic parameters are compared between HLS1 and CTRL. Significant differences of ΔMTV (t -test, $p < 0.01$) (Figure 3.6a) and ΔMTT (t -test, $p < 0.01$) (Figure 3.6b) were observed between two regions upon electrical stimulation, which indicates a higher transit velocity and lower transit time of the RBC traveling in the capillary bed, regional to HLS1 during hindpaw electrical stimulation. Correspondingly, significant differences of $\Delta CTTH$ (t -test, $p < 0.05$) (Figure 3.6c) were revealed between two regions, indicating a local capillary homogenization to HLS1 only, not globally across all cortical regions. Table 3.1 listed the MTV, MTT, and CTTH measured from both regions at rest and stimulation. Values represent mean \pm std from 12 animals.

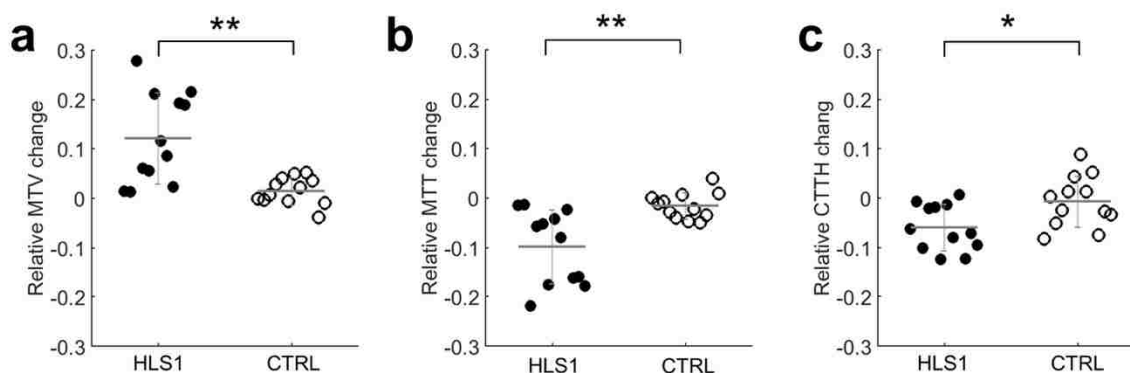


Figure 3.6. Statistical comparison of capillary parameters between HLS1 and CTRL

Relative change of capillary parameters compared between HLS1 and CTRL for (a) Δ MTV, (b) Δ MTT, and (c) Δ CTTH. * represents $p < 0.05$ and ** represents $p < 0.01$ (*t-test*, two-tailed)

Table 3.1. Capillary flow parameters during rest and stimulation (n=12)

Capillary flow Parameters (Mean \pm std)	HLS1		CTRL	
	Rest	Stimulation	Rest	Stimulation
MTV (mm/s)	1.037 \pm 0.223	1.146 \pm 0.229	1.059 \pm 0.212	1.077 \pm 0.228
MTT (s)	0.412 \pm 0.134	0.367 \pm 0.098	0.387 \pm 0.110	0.382 \pm 0.112
CTTH (s)	0.233 \pm 0.079	0.218 \pm 0.070	0.229 \pm 0.063	0.227 \pm 0.059

3.4 DISCUSSION

The current understanding about flow-metabolism coupling is incomplete. During cerebral functional activation, for instance, CBF and glucose metabolism remain coupled as they increase in proportion, whereas oxygen metabolism only increases to a minor degree, so-called uncoupling of CBF and CMRO₂ that produces BOLD signal in fMRI [42], [48]. Reports have speculated about the existence of a potential microcirculatory adjustment in capillary bed where oxygenation occurs. Using accepted diffusion properties of single capillaries, elaborate model shows that it is a basic property of the spatial organization of capillaries that oxygen extraction capacity depends not only

on tissue oxygen tension and arterial tone (as quantified by CBV, CBF and MTT), but also, to a large extent, on the distribution of capillary transit times. According to such, the Jespersen and Østergaard [51] have introduced a crucial physiological effect of CTTH reductions that seemingly counteract the drop in OEF that invariably occurs during functional hyperemia.

Using the transit time parameters introduced in previous framework, we investigated the effect of stimulus-evoked functional activation on microcirculatory hemodynamics in the mouse brain cortex using OCTA velocimetry, based on ED-based frequency analysis of RBC signals within the ensemble of repeated OCT A-scans. This imaging approach enabled >20,000 frequency-derived RBC velocities to be analyzed from each 3-D tissue volume within 75 s. Reported RBC velocity (v) distributions were converted to transit time (τ) distributions assuming $\tau = L/v$, where L is the length of the capillary path along which RBC exchanges oxygen with tissue before it converges to draining venules [54], [64]. We adopted the value of $L=400 \mu\text{m}$ reported in the literature as a conservative estimate of the RBC travel length in the capillary path to obtain the transit time distribution, upon which the spatial heterogeneity of capillary flow, CTTH, is derived in resting state and during hemodynamic response. In addition, our study employed the state-of-art LSCI to generate oxygenation maps to reveal functional activation with an increase in ΔHb , which indicates relative increase in CMRO_2 [5]. This provides evidence of concomitant oxygen metabolism to guide for OCTA scans at designated region and, for the first time, provides the validation of correlation of capillary flow homogenization with localized oxygen consumption. In our experiments, reductions in both MTT and CTTH were seen upon hindpaw electrical stimulation. Such changes were only observed at the cortex corresponding to hindlimb region (HLS1). The differences in hemodynamic response between HLS1 and the non-activated region is statistically significant (two-tailed t -test, $\Delta\text{MTV } p<0.01$, $\Delta\text{CTTH } p<0.05$). By plugging our observations into

the previous, we were able to confirm the correlation of capillary flow homogenization (CTTH reduction) with functional hyperemia (increased CBF and decreased MTT) during the increased demand of oxygen metabolism (increase in ΔHb) at activated tissue bed.

The *in vivo* observations of reduction in MTT and CTTH also well corroborate the prior findings using bolus tracking with TPM conducted in similar stimulation regime [51]. However, the magnitude of reduction measured in this study, $9.8\% \pm 2.2$ for MTT and $5.9\% \pm 1.4$ for CTTH, is less than the estimated values when using bolus tracking approach, where decreases of $11.3\% \pm 1.3$ and $24.1\% \pm 1.6$ were seen in CTTH and MTT, respectively, during electrical stimulation. This discrepancy may be due to the nature of signals measured. Bolus tracking measures the transport function of plasma dye, and their hemodynamic variables (therefore indicating plasma dynamics), whereas OCTA velocimetry evaluates directly the moving RBC. Difference between plasma and erythrocyte (RBC) transit times have been previously modeled and estimated (25%) [65]. Thus, MTT and CTTH values cannot be simply compared between two approaches. Before exact relationship of dissociation between plasma and erythrocyte transit time was established, OCTA velocimetry possesses an advantage in estimating RBC transit time distribution for capillary flow parameter measurements.

The current method is not without limitations. It was previously reported that the most pronounced changes in RBC velocity and flux were observed beyond depths of 200 μm [51], corresponding to layer II and III [66]. The capillary velocity measurements in the current study were performed within 300 μm thick slab from the cortical surface that covered the region of significant capillary flow change. However, to avoid biased measurement in deeper cortical layer due to multiple light scattering that causes optical signal attenuation, inner cortex (depths >300 μm) was not included in the analyses, and capillary flow response beyond such region remains to

be elucidated. In this current study, a linear relationship function between MF and capillary velocity was used to differentiate RBC speed information from the complex OCT signals, but the exact correlation considering the size and shape of RBC, hematocrit density has not been fully explored. Neither limitations, however, are thought to affect our comparisons of relative change in capillary parameters between two cortical regions to reveal localized capillary response and CTTH reduction to functional activation. Additionally, we notice that the measurement errors of the Δ MTV and Δ MTT in HLS1 are larger than those in CTRL among 12 animals. It may be necessary to increase the subject number and look into the criterion of Δ Hb in relation to the changes in the magnitude of capillary transit time parameter in the future systemic investigation of microvascular contribution to the brain oxygenation.

The use of isoflurane as anesthetic agent in this functional activation study was justified by previous observations that showed the preservation of neurovascular coupling under isoflurane anesthesia [67], [68]. We found isoflurane to be an easy-to-manage anesthetic drug, without negative effects on hemodynamics from accumulation of injectable anesthetic agents. However, vasodilatory effect of isoflurane [69] on capillary flow parameters in resting and functional activation state remains to be elucidated in awake animals.

3.5 CONCLUSION

We have investigated the microcirculatory adjustment to functional activation at mouse somatosensory cortex upon hindpaw electrical stimulation. The statistical powered ED-based OCTA analysis on capillary transit times in cerebral tissue beds has revealed a decreased MTT in consistency with functional hyperemia (CBF increase) and CTTH reduction locally to increased

ΔHb . The results support the important role of capillary flow homogenization to cerebral tissue oxygenation during functional hyperemia.

In addition to the spatial velocity distribution change observed in this study, temporal fluctuation of the velocity within the time interval of 400 μs (50 A-scans), termed bandwidth frequency (BF), were also obtained, which represents temporal heterogeneity of RBC in spatial capillary network [27]. Due to the space limitation, the change of BF, which were carefully investigated in another publication [70], will not be described here. Such useful ultra-microscopic perspectives may uncover the spatiotemporal relationship between capillary flow response and brain oxygenation during functional activation, which may potentially yield additional insight to the flow-metabolism coupling mechanism.

Chapter 4. VASODYNAMICS OF PIAL AND PENETRATING ARTERIOLES IN RELATION TO ARTERIOLO-ARTERIORAL ANASTOMOSIS AFTER FOCAL STROKE

4.1 SIGNIFICANCE

Pial arterioles are highly collateralized on the surface of the cerebral cortex, providing redundancy in the circulatory network [4]. Pial arterioles can respond to an occlusive event to redistribute blood flow through anastomoses, which is a vital neural self-protective mechanism in ischemic stroke [71]. The penetrating arterioles (PA) perpendicularly attached to the pial vessels, however, are excluded from the collateral circulation. These vessels bridge the mesh of inter-connected pial arterioles with the subsurface microvascular bed that feeds the underlying neural tissue, which were described as “bottleneck” in the perfusion of neocortex [72]. Therefore, the perfusion of PA directly impact the downstream capillary circulation and neural tissue survival during ischemic stroke. The ability to monitor the vasodynamics of pial and penetrating arterioles simultaneously during ischemic stroke can offer important insights about the vascular regulation in each type of vessel groups, and potentially improve stroke treatment methods.

Within the pial collateral network, the major cerebral arteries, known as middle cerebral artery (MCA), anterior cerebral artery (ACA), and posterior cerebral artery (PCA) are connected by arteriolo-arteriolar anastomoses (AAAs), with penetrating arterioles attaching to them as T-junctions [73]. Although the behavior of collateral and PA flow after small localized ischemic injury (e.g. photothrombosis) has been investigated [74], [75], little is known about the vasodynamics of pial and PA with respect to the location of AAAs during an occlusion of a major cerebral artery.

In this project, we apply OMAG and DOMAG to evaluate the vessel diameter, RBC axial velocity, and total blood flow changes in a large number of pial and PA across the stroke core penumbra region before, during, and after MCA occlusion (MCAO). We focus on analyzing the vasodynamics at different spatial location with respect to the AAA territory between MCA and ACA distal branches enclosed in the open-skull cranial window. OMAG and DOMAG images will be acquired at baseline, during 60 min of MCAO, and after reperfusion of the MCA. The following questions will be centrally addressed: How do the AAAs redistribute blood flow in response to MCAO; what kind of vasodynamic regulation do pial and PA has; and what are the implications to vascular stimulation therapy for onset stroke treatment.

4.2 MATERIAL AND METHODS

4.2.1 *Animal preparation*

All experimental animal procedures performed in this study were approved by the Institute of Animal care and Use Committee (IACUC) of the University of Washington (Protocol number: 4262-01). Six male 12-week-old C57/BL6 mice weighing between 23 to 25 g were purchased from Charles River Laboratories (Seattle, WA, USA). The mice were deeply anesthetized using 1.5-2% isoflurane (0.2 L/min O₂, 0.8 L/min air) and euthanized at the end of the experiments. During the entire experiment, the body temperature was maintained at 36.8 C through homeothermic blanket system (507220-F, Harvard Apparatus, MA, USA). All mice were subjected to three imaging periods (baseline, MCA occlusion, reperfusion) through a cranial window, covering the distal branches of MCA and ACA, as well as the arteriole anastomoses. Surgical procedure is briefly described as follows: First, a standard 3x3 mm cranial window was created on the left parietal cortex 1 mm lateral from sagittal suture and 1 mm posterior from bregma by drilling a circular groove and lifting the central island. A circular cover-glass was placed over the exposed brain

surface and sealed onto the bone with dental cement. Then, the cranial window was subjected to a baseline imaging by OMAG (see Optical Microangiography below). After the baseline imaging was taken, the mouse was subjected to an MCAO [76], which involves an intraluminal filament insertion from isolated external carotid artery (ECA) and a temporary ligation of the ipsilateral common carotid artery (CCA). The occluding filament was slowly advanced through internal carotid artery (ICA) toward the cranial base until a mild resistance was felt. A laser Doppler flowmetry microtip was placed perpendicular to the calvarium from superior nuchal line to the nasion as a guidance during MCAO. Another set of OMAG images were taken at the same region under the window during the occlusion period of 60 minutes. For reperfusion, filament was removed from ICA, and OMAG images were again acquired to represent the reperfusion. However, due to the time constraint of the experiment, we were unable to image reperfusion without untying the CCA. From the laser Doppler flowmetry guidance, there was about 28% decrease in total flux with ligated CCA compared to the baseline, in average of 6 mice.

4.2.2 *Optical microangiography*

To visualize the volumetric microvasculature, OMAG scanning protocol was applied with 400 A-lines covering a distance of ~ 1.5 mm constituted each B-frame (fast axis). In the slow axis (C-scan), there were 400 steps, also covering a distance of ~ 1.5 mm. At each step, 8 repeated B-frames were acquired. With this scanning protocol, the data cube of one complete 3D scan was composed of 1024 by 400 by 3200 (z-x-y) voxels, which took ~ 18 s to acquire with an imaging rate of 180 fps. To obtain microvasculature down to the capillary level at each step, an ED-based clutter filtering algorithm [18] was used to separate structural tissue from dynamic scatters (e.g., moving red blood cells within patent vessels) from the 8-repeated B-frames. Hence the final 3D vascular image was composed of 1024 by 400 by 400 (z-x-y) voxels.

After each OMAG scan, DOMAG scanning was performed covering the same area to show the axial velocity map of cerebral blood flow (CBF) [24]. The calculation of axial flow velocity of the RBC using phase-resolved technique can be found in Section **Error! Reference source not found.** In order to have an axial velocity range of ± 6.1 mm/s, Doppler processing of complex signals was applied among A-lines in each step by using 3 A-line interval to increase T between processed A-lines. A phase variance mask was then employed to segment meaningful Doppler flow signals from noisy phase background. Each B-scan in DOMAG protocol consisted of 10000 A-lines by acquiring 25 A-lines at each 400 discrete steps. In the slow scan direction (C scan), there were 600 discrete steps, i.e., 600 B scans. The data cube of each processed 3D vascular image was composed of 1024 by 400 by 600 (z-x-y) voxels, which took ~ 100 s to acquire with 6 fps imaging speed. More details about this imaging protocol can be found in [24].

To acquire the CBF images over a large area of the cortex, these imaging protocols were repeated to create a mosaic image. OMAG and DOMAG algorithms were first applied to the datasets acquired at the basal condition. After applying MCAO to the mouse, the imaging protocol was repeated over the same area during occlusion and reperfusion by keeping the discrepancies minimum between the three imaging sessions in terms of the depth of the focus of the probe beam and the positioning and orientation of the sample.

The data are presented as mean \pm sem. among 6 animal experiments. The differences between the experimental means of basal, occlusion and reperfusion conditions were tested with a two-tailed paired *t-test*.

4.3 RESULTS

4.3.1 *Pial and penetrating arteriole vasodynamics under basal conditions*

Pial and penetrating arteriole mapping in the mouse cortex were obtained through imaging the cranial window (9 mm^2) using the OMAG techniques. The volumetric average intensity projection (AIP, or enface) of 3D OCT structural images (**Figure 4.1a**) is used here to visualize and locate the diving and rising vessels. Because of the strong light absorption from hemoglobin, these vertically oriented vessels (parallel to the probing beam) appear as dark dots in the enface AIP of structural OCT image in contrast to cerebral tissues. These penetrating and rising vessels are also approximately perpendicular to the pial vessels. This appearance helps with the detection of penetrating arterioles easily as compared to the maximum intensity projection (MIP, or enface) of OMAG blood flow images.

The OMAG result of blood flow map in the cerebral cortex is given in **Figure 4.1b**. To be able to focus on the pial arterioles, only the MIP of capillary loop region up to $100\mu\text{m}$ depth is presented, which was within the depth of focus of the probe beam. The bidirectional RBC axial flow velocity map of pial and penetrating vessels are demonstrated by DOMAG in **Figure 4.1e**, showing the penetrating arterioles and the rising venules as green and red colors, respectively. The flow velocity information is coded with a color bar in a range of $\pm 6.1 \text{ mm/s}$. The dense scanning protocol enables the imaging of various RBC at multiple locations to form continuous lines, however the discontinuities are still present due to very low relative axial velocity of RBC when they are nearly perpendicular to the probe beam (e.g. pial vessels). Few out-of-range flow is also observed as phase-wrapped signals, seen as yellow color (combination of red and green). The closer views of a region of interest (ROI) in **Figure 4.1b** and **Figure 4.1e** are shown in **Figure 4.1c** and **Figure 4.1f**.

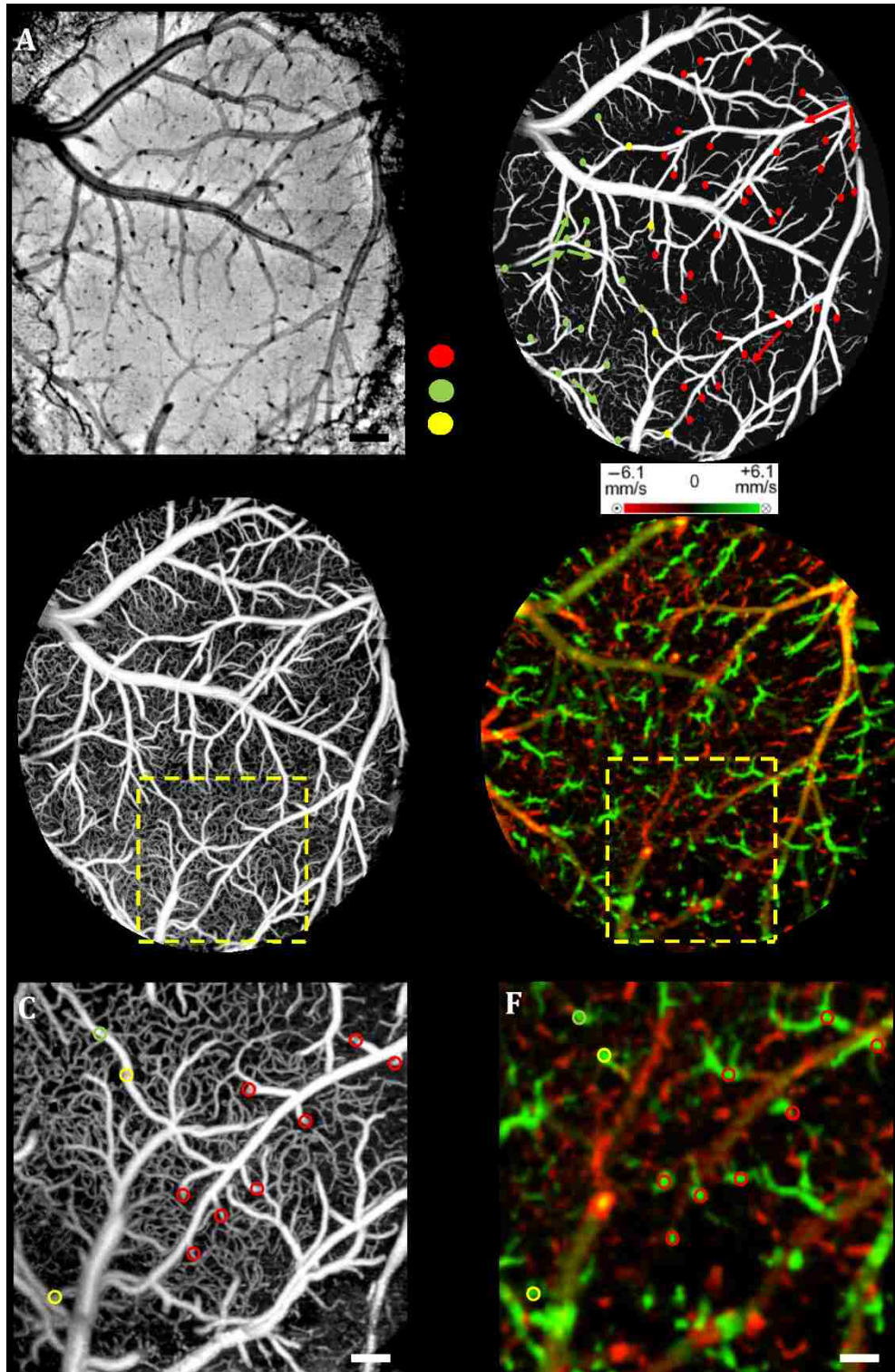


Figure 4.1. Pial and penetrating arteriole vasodynamics under basal conditions

(a) *En face* average intensity projection (AIP) of the cortical structure through the cranial window. (b) *En face* maximum intensity projection (MIP) of optical microangiography (OMAG) within 100 μm in depth from the cortical surface. (c) Closer view of a region marked by a dashed yellow box in (b). (d) *En face*

map to show penetrating arterioles in OMAG image. Red, green, and yellow dots correspond to MCA, ACA, and AAA T-junction sourced arterioles, respectively. (e) *En face* MIP of DOMAG that shows axial velocity distribution within 500- μ m depth from cortical surface. (f) Closer view of a region marked by a dashed yellow box in (d). In (c) and (f), penetrating arterioles are marked by circles. Scale bar represents 0.35 mm in (a, b, d, e) and 0.15 mm in (c, f).

Individual penetrating arterioles in the cranial window were located manually in the high contrast version of **Figure 4.1b** and are shown in **Figure 4.1d**. To do so, the *en face* AIP of the OCT structure image (**Figure 4.1a**) was used as a guide to detect the location of the penetrating arterioles, then the DOMAG image (**Figure 4.1e**) was employed to differentiate the MCA and the ACA branches from veins, then to locate the AAA T-junctions. In the particular case presented in **Figure 4.1**, the penetrating arterioles that are attached to MCA and ACA are marked with red and green dots, respectively; the ones that are attached to AAA as dually supplied T-junctions are denoted with yellow dots (**Figure 4.1d**). We do not make selections based on speed or diameter. The corresponding arterioles are also pointed out in the ROI images with circles in **Figure 4.1c** and **Figure 4.1f**. Based on random sampling (n=6 animals), the mean lumen diameter of 143 pial and 127 penetrating arterioles at basal conditions were 40.7 μ m and 25.6 μ m, respectively.

4.3.2 *Pial and penetrating arteriole vasodynamics in response to MCAO*

Changes in pial and penetrating arterioles in response to MCAO (**Figure 4.2a-c**) and after reperfusion (**Figure 4.2e-f**) were delineated using OMAG and DOMAG. During the 60-min occlusion, MCA branches failed to support its downstream penetrating arterioles, but collateral flow through AAA started to function, observed as the flow reversal of MCA, and ACA branches took over some of the penetrating arterioles flow support. However, not all penetrating arterioles can be reached by the collateral circulation. The penetrating arterioles reside in the weak AAA territory as pointed on in **Figure 4.2c** experiences hypo-perfusion. Additionally, the penetrating arterioles flow never reversed in consistence with the previous literature [74]. As a

result, the average lumen diameter of the pial and penetrating arterioles were measured as 38.8 μm and 24.2 μm , which were both decreased compared to baseline.

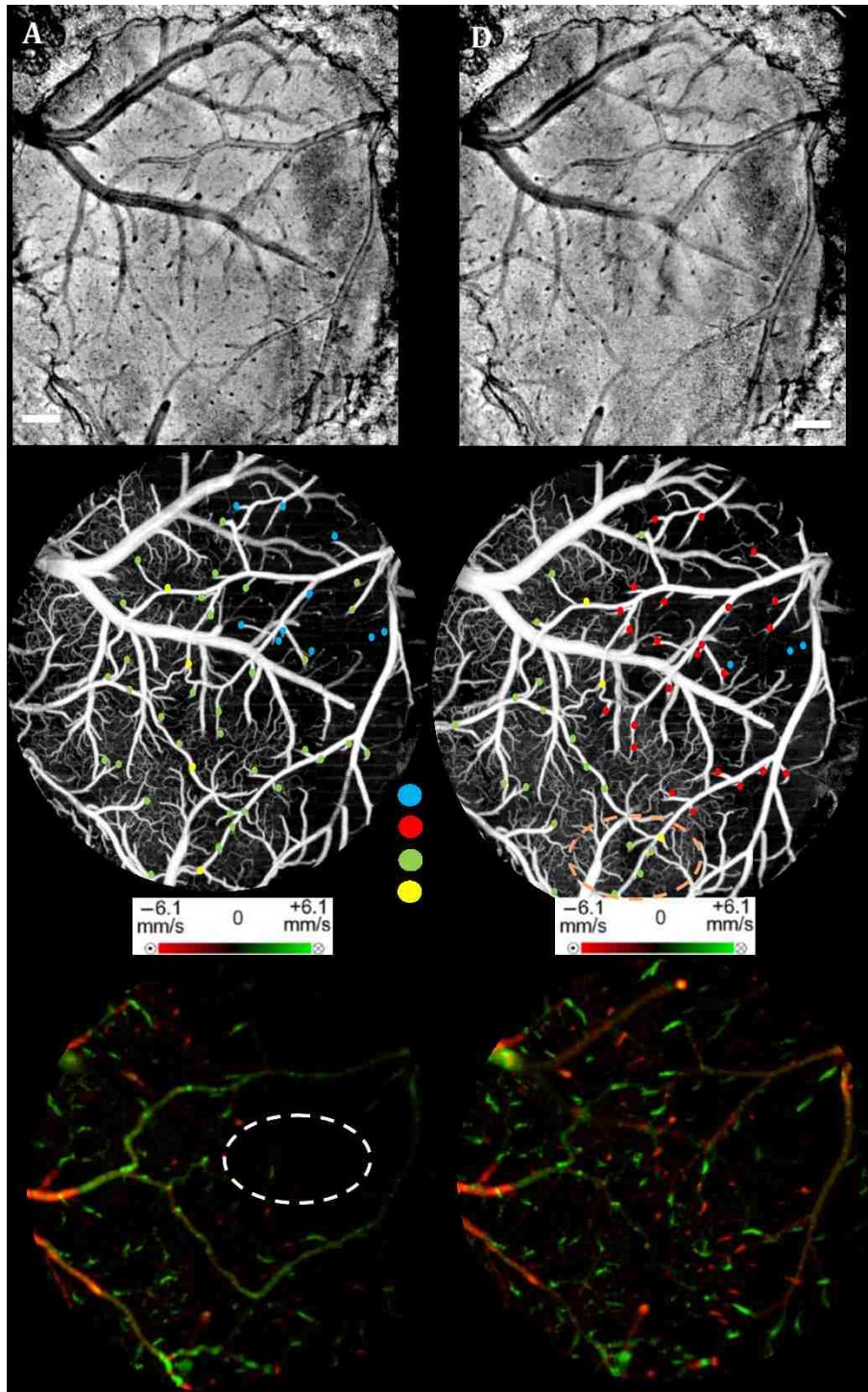


Figure 4.2. Changes in flow pattern in the pial network during MCAO and reperfusion

(a, d) *En face* AIP of the cortical structure through the cranial window (a) during occlusion and (d) during reperfusion, respectively. (b, e) *En face* OMAG MIP of the microcirculation network within 100- μm depth from the cortical surface (b) during occlusion and (e) during reperfusion, respectively. Map of the diving arterioles on OMAG image is shown. Red, green, and yellow dots correspond to MCA, ACA, and AAA T-junction sourced arterioles, respectively. Yellow dots in (b) are showing the location of T-junctions in the baseline while they were supplied by MCA and ACA. Blue dots correspond to the diving arterioles that are at not-detectable level compared to basal condition. Dashed circle in (e) points out the shift in the location of T-junction point. (c, f) *En face* DOMAG MIP of velocity distribution within 500- μm depth from cortical surface (c) during occlusion and (f) during reperfusion, respectively. Dashed circle in (c) points out the area with failed collateral support. Scale bar represents 0.35 mm.

During the reperfusion, some of the AAAs stayed active in supplying blood to four of the penetrating arterioles via ACA. Three penetrating arterioles of MCA that were rescued by collateral circulation during MCAO survived after occlusion (**Figure 4.2e**). On the other hand, most of downstream flow distance from the AAA territory disappear during MCAO and do not reappear after reperfusion. The average lumen diameter of the corresponding pial and penetrating arteriole return back to their baseline values with a slight increase (hyper-perfusion), which were measured to be on average at 41.1 μm and 26.1 μm , respectively. The comparison of the average lumen diameter among baseline, occlusion and reperfusion conditions for the pial and penetrating arterioles is shown in **Figure 4.3**. The lumen diameter of the penetrating arterioles changes dramatically in response to stroke, whereas the lumen diameters of the pial arterioles are only slight affected.

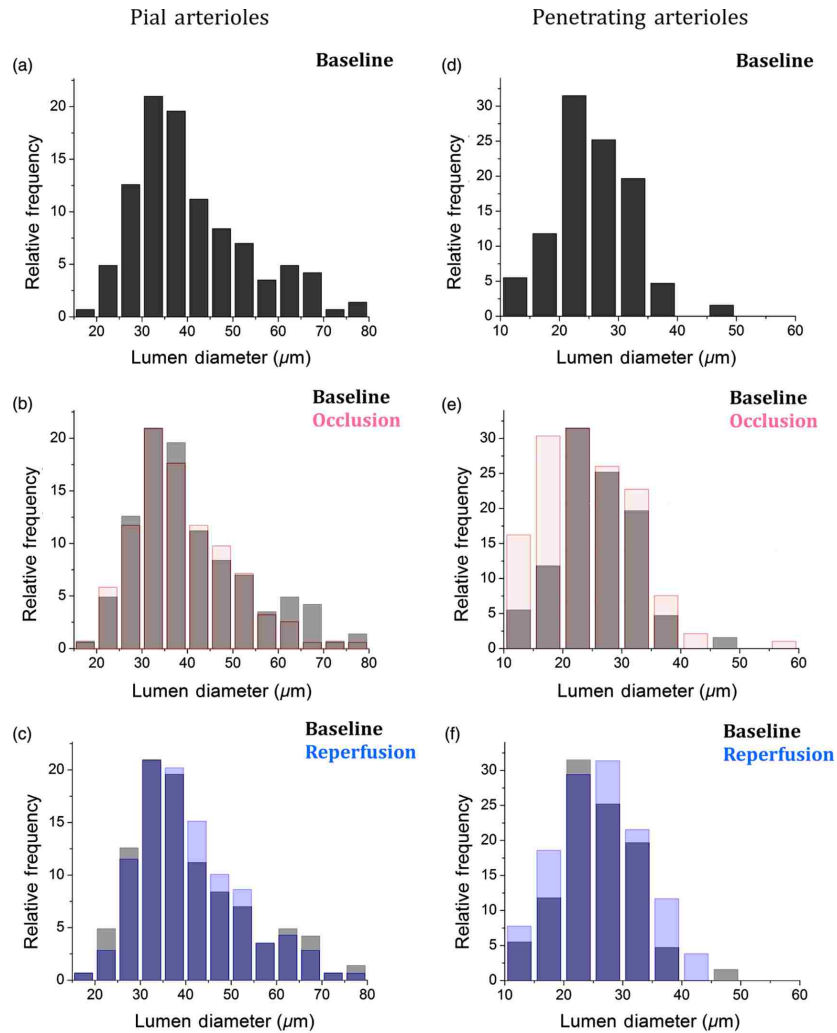


Figure 4.3. The lumen diameter distribution of pial and penetrating arterioles.

(a) Pial arterioles at baseline with overlay to occlusion (b) and reperfusion (c). (d) Penetrating arterioles at baseline with overlay to occlusion (e) and reperfusion (f).

4.3.3 Pial and penetrating arteriole vasodynamics in relation to AAA

AAA's role supporting collateral circulation during MCAO is analyzed with both OMAG and DOMAG and schematically presented in **Figure 4.4**. Two ROIs were selected in the DOMAG images where the presence of AAA is either strong or weak (**Figure 4.4a-c**). These regions are also located in OMAG images and the corresponding penetrating arterioles are marked in **Figure 4.4d-f**. Then the mean lumen diameter, the total blood flow, and the RBC axial velocity in the penetrating arterioles and the pial arterioles within these regions are compared. **Figure 4.5b**

shows that the penetrating arterioles that are close to the strong AAA territories dilate whereas the pial arterioles do not, which is consistent with previous findings [74]. Although the dilation effect in the average lumen diameter is subtle, it is statistically significant. On the other hand, the penetrating arterioles constrict significantly in the weaker AAA territories as shown in **Figure 4.5c**. Moreover, the total blood flow and RBC mean axial velocity in the penetrating arterioles close to a weak AAA suffered from a significant drop compared to the ones close to a strong AAA (**Figure 4.5e** and **Figure 4.5f**).

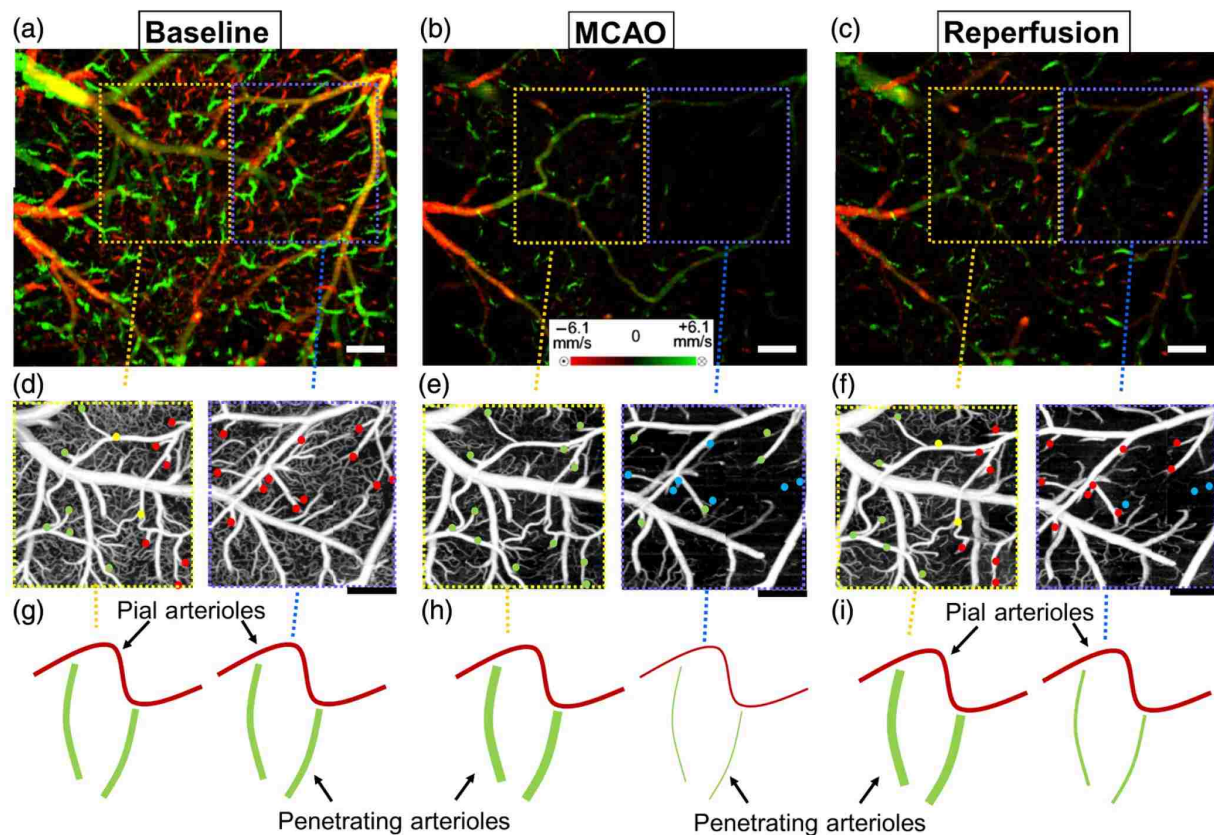


Figure 4.4. Vasodynamics of penetrating arterioles with respect to AAA during stroke.

(a–c) DOMAG results for (a) basal, (b) during MCAO, and (c) after reperfusion conditions, respectively. Strong AAA area is marked with a yellow dashed box and weak AAA area with a blue dashed box. (d–f) OMAG comparison between strong and weak AAA ROIs for (d) basal, (e) during MCAO, and (f) after reperfusion conditions, respectively. (g–i) Red, green, and yellow dots correspond to MCA, ACA, and AAA T-junction sourced arterioles, respectively. Blue dots correspond to the diving arterioles that are at not-detectable level compared to basal condition. Cartoon representations of the lumen diameters of pial and penetrating arterioles for (g) basal, (h) during MCAO, and (i) after reperfusion conditions, respectively. Scale bar is 0.3 mm.

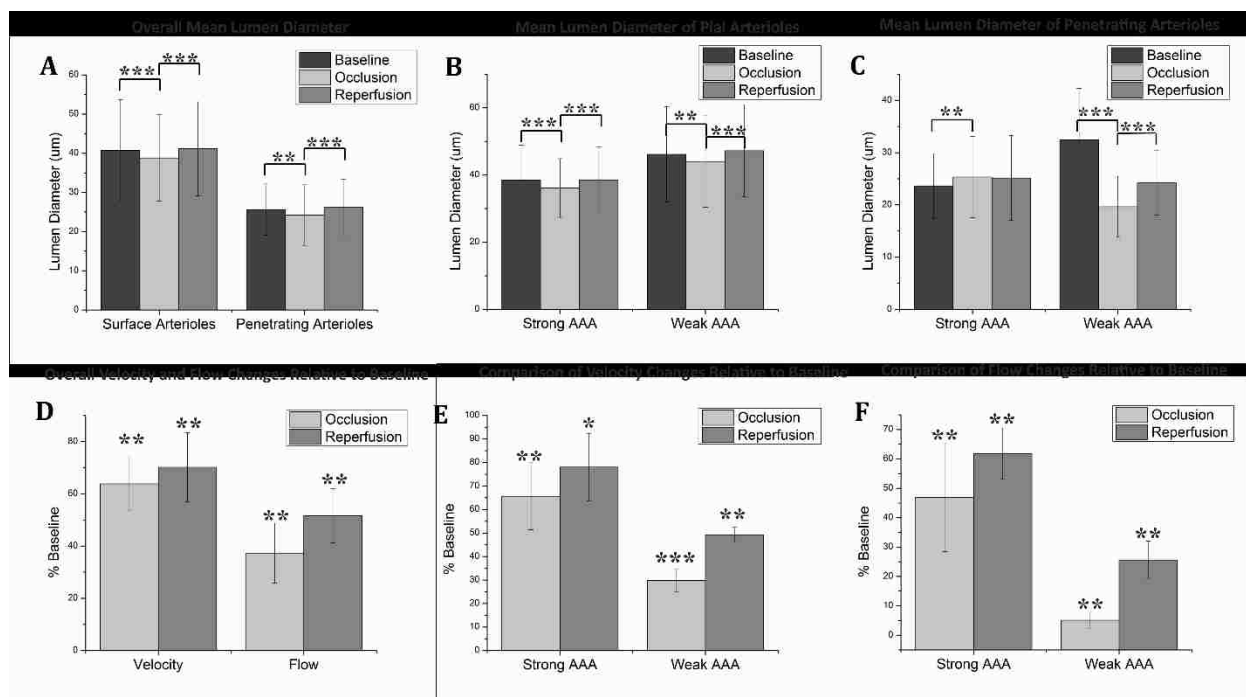


Figure 4.5. Lumen diameter, velocity, and flow comparison.

(a) the mean lumen diameters of 143 pial and 127 penetrating arterioles for basal, occlusion, and reperfusion cases ($n = 6$ animals). (b, c) Comparison of mean lumen diameters of pial and penetrating arterioles, respectively, between strong and weak AAA areas. $***P < 10^{-3}$ and $**P < 0.05$ significantly different data sets (paired *t-test*). (d) The mean total blood flow and RBC velocity changes compared to baseline among 127 penetrating arterioles during occlusion and reperfusion ($n = 6$). (d, e) Comparison of velocity and flow changes in penetrating arterioles between strong and weak AAA areas, respectively. $***P < 10^{-3}$ and $**P < 0.05$ significantly different data sets from baseline (paired *t-test*).

4.4 DISCUSSION

To reveal the role of cerebral pial arteriole network in the local hemodynamic homeostasis during ischemia, we evaluated diameter and flow fluctuations in a total of 143 pial and 127 penetrating arterioles overlaying the stroke penumbra from six animals during MCAO. Three main findings are highlighted: (1) The flow reversals occur in the pial arterioles through anastomosis and ACA takes over blood supply to the penetrating arterioles attaching to the MCA side. (2) The penetrating arterioles near a strong AAA territory dilate and sufficiently restore the flow to the ischemic region. (3) The flow compensation decreases with the increase of the

distance away from the AAA territory, resulting in poorly recovered penetrating arterioles residing away from the AAA connections during reperfusion.

Pial and penetrating arterioles respond differently to an occlusion, and they act together to compensate blood flow to an ischemic region. Reversible blood flow in the pial arterioles occurs according to a pressure gradient. When the brain is subjected to an ischemic event by MCAO, the flow balance in AAAs is immediately disrupted and the retrograde blood flow appears in MCA, as found in [73] and [77]. However, no dilation events are observed among the pial arterioles in the experiment. In contrast, the penetrating arterioles can actively dilate to deliver blood to the ischemic region, but no reversal flow occurs in the penetrating arterioles, which is consistent with the previous finding in [74]. In addition, an interesting fact found in our study is that the distribution of the arteriole dilations is not homogeneous across the ROI. The penetrating arterioles close to a strong AAA connection dilate despite the overall decrease in mean lumen diameter. In other words, the penetrating arterioles constrict significantly in the areas further away from AAAs. To summarize, in order to have active dilations of the penetrating arterioles during severe ischemia, the pial arterioles must be kept flowing due to the regulation of AAAs. Moreover, the lack of blood supply for the pial arterioles also affects the recovery of the penetrating arterioles during reperfusion. Our data report a higher restoration of RBC velocity in the penetrating arterioles near a strong AAA territory in comparison with a weak one, which is critical for the survival of the tissue during stroke recovery.

Besides the CBF images, the *en face* AIP of 3-D OCT structural images from 60 min of occlusion and reperfusion **Figure 4.2a** and **Figure 4.2b** also lead to an interesting observation: regions in the areas far from the AAA territory appear darker compared to the uniform looking baseline. The increased light scattering due to the changes in cell morphology in the infarct

region [78] is suspected to be responsible for the nonuniform intensity distribution in the cortex after stroke. This phenomenon was also observed by mapping light attenuation coefficients and was correlated with histology in a similar MCAO model [77].

The label-free OMAG technique offers a unique ability to quickly image a relatively large area in time-sensitive stroke experiments. However, it comes with some limitations. First, the lateral resolution of our system is $\sim 7 \mu\text{m}$ with a depth of focus of 0.12 mm. This makes the diameter measurement inaccurate for the pial vessels, especially for those smaller than $20 \mu\text{m}$. Second, since only the axial velocity is measured, it is difficult, if not impossible, to detect the RBC velocities and flow in the pial vessels perpendicular to the optical axis, due to their very small axial velocities, hence a slightly tilted stage is needed to solve this problem. Moreover, the absolute flow information is hard to derive accurately due to the resolution and the light intensity deterioration with depth. Hence, this technique is best suited for comparison studies where errors in the measurements do not affect the differential conclusions. In this study, we tried our best to keep all the crucial parameters, such as the focus of the probe beam and positioning and orientation of the sample, the same among all the imaging sessions. To check if there is a systematic error in the determination of total blood flow in penetrating arterioles, the total blood flow conservation rule is applied. The average velocity and flow in the 127 pairs of penetrating arterioles and rising venules are similar within a 10% margin.

In summary, our methods enable us to discover the AAAs' role in the collateral blood perfusion dynamics in the mouse cerebral cortex after focal stroke. Thanks to the high sensitivity and the large field of views provided by OMAG, we compare regions in cerebral cortex, either closer to or further away from AAA territory during MCAO. The conclusions suggest that AAA plays a major role in active regulation of the pial and penetrating arterioles during stroke,

providing blood flow to actively dilate the penetrating arterioles in order to rescue the tissue in the penumbra region.

Chapter 5. AGING-ASSOCIATED CHANGES IN CEREBRAL VASCULATURE AND BLOOD FLOW AS DETERMINED BY QUANTITATIVE OCTA

5.1 BACKGROUND AND MOTIVATION

Normal aging is associated with modifications to the biomechanical properties of blood vessels, which can result in anatomical and functional alterations in the brain vasculatures [79], and potentially lead to hypoperfusion or neurodegeneration [80]. Although there is no consensus reached regarding the causal relationship between a decreased cerebral blood flow (CBF) and decline of neuronal function, there is an increasing prevalence of coincident cerebrovascular deficiency and cognitive dysfunction with aging that is also well recognized in Alzheimer's disease (AD) [81]–[83]. Thus, the ability to image cerebral vasculatures with superior spatial detail in the aging brain and to precisely quantify vascular parameters will not only be invaluable to uncover the vascular deficiency associated with normal aging, but also crucial to decipher the functional relationship between cerebrovascular factors and pathological neurodegeneration.

A compromised structural integrity of the cerebral vasculature is a representative degenerative feature of the vascular system in aging brain [84]. Changes in vascular morphology have been identified in early studies by microscopy with post-mortem brain tissue. In larger vessels, for example, increased tortuosity have been observed in the middle, anterior and posterior cerebral arterioles of aging mice [85], [86], and in the penetrating arterioles within the white matter from humans as early as in middle age [87], [88]. At the level of cerebral microvessels, there is considerable evidence of an age-related reduction in capillary numbers and capillary density in the brain of aged rodents [89]–[97], and a decreased capillary density in older human brains [98]–[102].

The anatomical changes seen in the cerebral vessels may alter the conductance and resistance of the vascular network, leading to reduced CBF or even hypoperfusion in the cerebral tissue [103]. Consequently, cerebral metabolism can diminish, which eventually jeopardizes functional neuronal activities [104]. A number of clinical studies employing a range of imaging technologies have investigated CBF or arterial flow velocity in healthy aging subjects. Functional magnetic resonance imaging (fMRI) [105] and positron emission tomography (PET) [106] have used to reveal regionally-specific decreases in CBF during functional activity of brain in aging, while transcranial Doppler sonography [107] has shown a decrease in blood flow velocity in large cerebral arteries with advancing age. Although these *in vivo* imaging studies have cumulatively found an association between macroscopic perfusion reduction and aging [108]–[111], changes in microscopic flow remained poorly understood due to their inherent limitations in providing adequate spatial resolution required to assess capillary flow [112], in addition to a sufficient penetration depth to image sub-surface cerebral microvessels in a living subject without excessive disruption to the neuronal environment. A recent aging study has attempted to address such challenges by utilizing high-speed two-photon fluorescence microscopy (TPM) to examine age-related differences in cerebral capillary blood flow between young and old rodent brains *in vivo* [55]. Despite outstanding image quality, the very slow speed of data-acquisition and the restricted imaging area ($800\mu\text{m} \times 800\mu\text{m}$) or depth ($100\ \mu\text{m}$ below the surface) make the TPM a less ideal tool for imaging cerebral capillary blood flow.

Optical coherence tomography (OCT) has emerged as a non-invasive neuroimaging technique that distinguishes itself from other micrometer-scale resolution imaging techniques with a significant speed advantage in 3-D imaging and an appreciable penetration depth, typically at ≥ 1 mm in tissue[59]. Furthermore, recent advances in OCT angiography (OCTA) techniques, such as

the development of optical microangiography (OMAG) [17], have allowed for the acquisition of blood flow information from the volumetric OCT dataset down to the capillary level by coherently analyzing the intrinsic scattering property of moving RBC in functioning blood vessels. Furthermore, Doppler OMAG (DOMAG) [24] has been developed to quantitatively measure RBC moving velocity via the axial component and to evaluate penetrating arterioles (PA) flow dynamics in the cerebral cortex [62]. In addition to quantitative assessment of arteriole blood flow, we have recently developed an eigen-decomposition (ED) analysis of the complex optical signals generated by high-speed OCTA scans to extract the frequency components of single-file moving RBC in capillary passages [27]. A statistical evaluation of a large quantity (thousands) of capillary velocities in 3-D tissue volumes at 50 μ s temporal resolution provides a glimpse of the heterogeneity of capillary flow heterogeneity in the region of interest.

In this study, we employed a combination of OCTA techniques to examine the age-related vascular and blood flow changes in the cerebral cortex of anesthetized mice *in vivo* using a single imaging platform. The effect of aging on cerebral vessel structure and *in vivo* flow dynamics is quantitatively characterized using OCTA measurement parameters of vessel tortuosity and density, CBF, capillary velocity and heterogeneity.

5.2 METHOD AND MATERIALS

5.2.1 *Animal preparation*

All experimental procedures in this study performed on animals were approved by the Institutional Animal Care and Use Committee (IACUC) of the University of Washington. Young (2-month-old, n=8) and old (16-month-old, n=8) male C57BL/6 mice (Charles River Laboratory) were used. Females were not included due to potential influence of hormonal fluctuation on blood flow. Mice

were housed in individual cages at the imaging facility for at least 1 week prior to experimentation on a 12/12-hour light/dark cycle with access to food and water ad libitum.

On the day of the experiment, mice were anesthetized with isoflurane and placed on a stereotaxic frame (51625, Stoelting Co.) for head stabilization. Isoflurane was continuously being delivered to the animal with a mixture of 0.2 L/min pure oxygen and 0.8 L/min air. Each mouse received an open skull cranial window surgery [37], where a 4.5 mm-diameter round craniotomy at the somatosensory cortex (S1) region (1 mm posterior and lateral to the bregma) was performed on the right parietal bone as shown in an inset of **Figure 5.1**. The entire cranial window was subjected to OCT imaging with dedicated scanning protocols in section. Physiological parameters of the animal were monitored, including anesthesia depth, blood pressure, heart rate, and body temperature throughout the experiments, before then being euthanized by cervical dislocation.

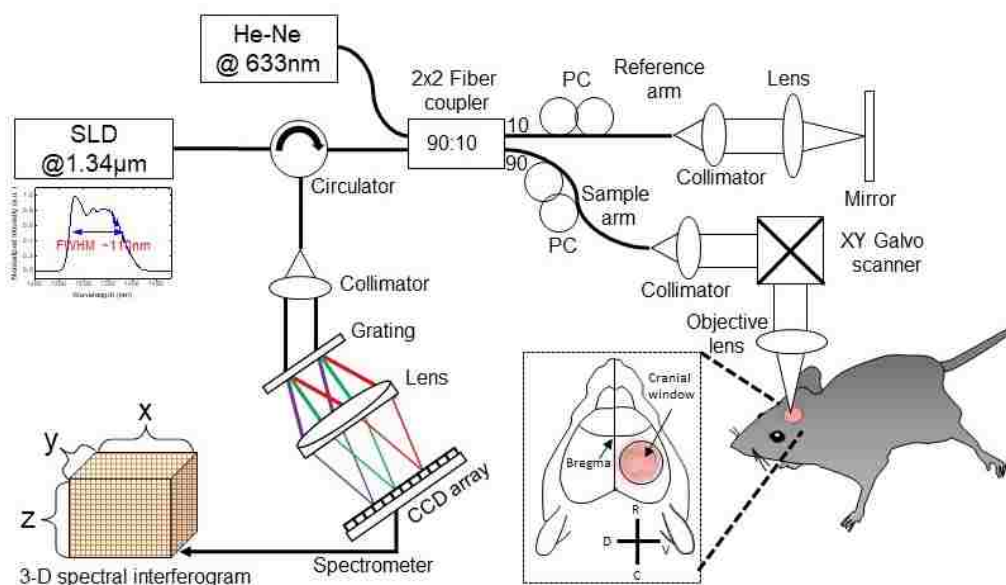


Figure 5.1. System setup and cranial window preparation

All imaging were performed on this single SD-OCT platform. A 5-mm diameter round glass cranial window was created on the right parietal bone at 1 mm posterior and lateral to the bregma. Scale bar orientation: C, caudal; D, dorsal; R, rostral; V, ventral.

5.2.2 *OCTA scanning protocols*

OMAG [17] is used to image the morphological features of cerebral blood vessel networks. In this protocol, each B-frame consisted of 400 A-lines (z axis) covering a distance of ~ 2.5 mm in the transverse direction (x axis). B-frame was repeated 8 times at each transverse location, and a total of 400 locations was recorded in the C-scan direction (y axis) covering a distance of ~ 2.5 mm. Therefore, the final 3-D volumetric dataset consisted of 3200 B-frames, which took ~ 15 s to acquire at A-scan rate of 72 kHz and B-frame rate of 180 frames/sec (fps). This protocol was performed on four quadrants, and the final image ($4\text{mm} \times 4\text{mm}$) was automatically stitched from 4 angiograms with ~ 1 mm overlap.

DOMAG [24] is used to image axial velocity components of cerebral blood flows, particularly in penetrating vessels. This protocol was performed with 25 A-lines repeatedly acquired at each depth location to give one M-scan (z axis). A B-frame consisted of 300 M-scans covering ~ 2 mm (x axis), and a total of 300 B-frames (y axis) covering ~ 2 mm was captured to accomplish the 3-D dataset. The total scanning time of each dataset is ~ 50 s at A-scan rate of 45 kHz and B-frame rate of 6 fps. This protocol was performed on 9 tiles over the cranial window to produce the final stitched bidirectional flow velocity map ($5\text{mm} \times 5\text{mm}$).

OCTA capillary velocimetry [27] is used to image heterogeneous properties of capillary hemodynamics within scanned tissue beds. In this protocol, we set the A-scan rate to be 20 kHz with 50 A-line performed consecutively at each M-scan position. This setting yields adjustable A-line interval time from $50 \mu\text{s}$ to 2.5 ms to potentially analyze slow to fast capillary flows from $100 \mu\text{m/s}$ to 5 mm/s. A B-frame consisted of 200 M-scans covering ~ 1.5 mm (x axis). A total of 200 B-frames covering ~ 1.5 mm (y axis) was acquired to finish off the 3-D dataset. The total time to complete one 3-D dataset is ~ 100 s. This protocol was performed at two selected regions inside

the cranial window, one region was proximal to the middle cerebral artery (MCA), and the other proximal to anterior cerebral artery (ACA).

5.3 DATA ANALYSIS

5.3.1 *Arterial tortuosity measurement*

Vessel tortuosity index (VTI) was used to evaluate vessel tortuosity, which is defined as an arc-chord ratio [113], i.e. the ratio of a length of curved vessel (arc) to a distance of straight line (chord) between the end points of a vessel segment (**Figure 5.2a**). In this analysis, segments MCA and ACA were chosen, referred to as arteriolo-arteriolar anastomosis (AAA), for collateral tortuosity comparison between young and old population. Our choice of AAA is rationalized by the frequent development of collateral vessel tortuosity being reported in normal aging [85]. A manual segmentation was performed from 3-D OMAG angiograms to show pial vessels within 50- μ m-thick slab from cortical surface followed by a binary processing to obtain the vessel skeleton. In a representative 5-pixel skeletonized vessel centerline (**Figure 5.2b**), chord length was simply the Euclidean distance (yellow dashed line) between two end-point pixels, whereas the arc length was obtained by summing distance of horizontally/vertically and diagonally connected pixels using pixel connectivity method [114], which describes the way in which pixels relate to their neighbors. In this method, the horizontally and vertically connected pixels are identified as 4-neighborhood pixels, whereas the diagonally connected pixels are regarded as 8-neighborhood pixels. For an example, the vessel segment in **Figure 5.2b** returns pixel paths of 3 and 1 for 4-neighborhood (**Figure 5.2c**) and 8-neighborhood (**Figure 5.2d**), respectively. The resulting arc length can be calculated by: (differences of pixel path number between 4- and 8-neighborhoods) $\times \sqrt{2}$ + total pixel number – pixel path number for 4-neighborhood, that is $((3-1)\times\sqrt{2})+5-3=4.8$. Finally, the

VTI was calculated by arc/chord ratio, having a minimum value of 1 (i.e. if $VTI = 1$, the vessel is straight).

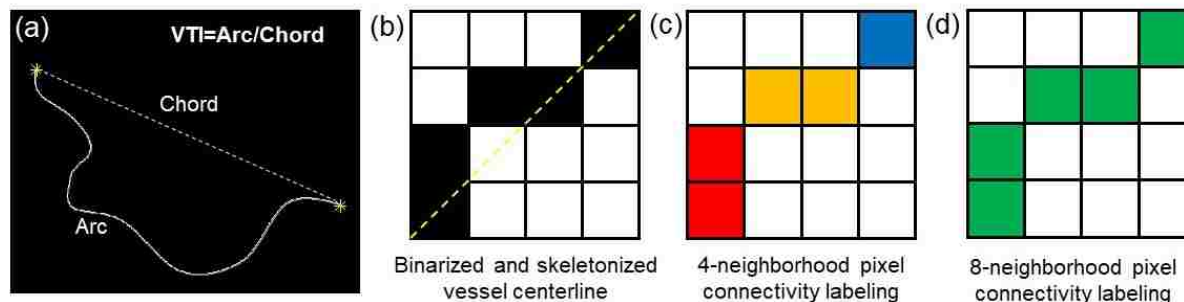


Figure 5.2. Method used for vessel tortuosity measurements

(a) A sketch demonstrating the definition of vessel tortuosity index (VTI) as a length of vessel (arc) divided by a length of straight line (chord) connecting its end points (yellow asterisks). (b) A 5-pixel example of binary vessel segment, with chord distance marked in yellow dashed line. (c) Pixel connectivity labeling for 4-neighborhood pixels. If the 4-neighborhood condition was not met, the pixel path changes with a different label color. Therefore, 3 paths are labeled with 3 different colors: red, yellow, and blue. (d) Pixel connectivity labeling for 8-neighborhood pixels. In this case, all 5 pixels are 8-neighborhood pixels, touching one of the neighbor pixel's edges or corners; thus giving 1 complete pixel path labeled with green.

5.3.2 Capillary vessel density quantification

We calculated vessel area density (VAD), defined as the percentage of area occupied by vessels [115], [116], of the capillary network obtained from OMAG angiogram. This parameter calculation was developed previously within our group and validated in ophthalmic imaging for retinal VAD measurements [115]. To more accurately evaluate cerebral capillary VAD, we reconstructed the 3-D OMAG dataset to segment a 300- μm -thick slab of vessels from the cortical surface, avoiding biased measurements at deeper cortical layers due to multiple-scattering that might cause signal attenuation and resolution degradation. Additionally, large pial vessels (>50 μm in diameter) from the *en face* image were excluded. Therefore, individual capillaries within the reconstructed 3-D image were resolvable. The image was then processed into a binary image

using global thresholding, a hessian filter, and adaptive thresholding to generate a binary vessel area map, where a value of 1 represents a white pixel, i.e. the presence of a capillary vessel, and 0 the black pixel, i.e. the absence of a functioning vessel. Finally, the VAD was calculated as a ratio of the area occupied by vessels to a given region ($2.5 \text{ mm} \times 2.5 \text{ mm}$ selected).

5.3.3 *CBF analysis*

Penetrating arterioles (PA) pass blood directly from the pial vessel network and remains uncollateralized, which vertically descend into the cortex tissue and return as rising venules (RV) to the pial network [72]. We evaluated CBF in both arterioles and venules from 3-D DOMAG velocity maps. In this method, firstly, the axial velocity of PA/RV found by phase-based methods utilizing the well-known Doppler effect [23], [117]. From the 3-D velocity dataset, an x-y orthogonal slice $\sim 50 \mu\text{m}$ below the cortex surface was selected from the 3-D dataset to evaluate flow cross sections. Next, regional CBF was obtained by $\text{velocity} \times \text{flow area}$ for each type of vessels measured within $3.5 \text{ mm} \times 3.5 \text{ mm}$ region. The values were then normalized to a unit region (1 mm^2) and compared between young and old groups. Note that this CBF measurement is independent of the Doppler angle [25], [118].

5.3.4 *Capillary mean velocity and velocity heterogeneity calculation*

An eigen decomposition (ED) -based analysis was used to reveal capillary flow velocity within the 3-D tissue volumes [27]. Briefly, a frequency analysis was firstly obtained using the covariance matrix of grouped A-lines (50 repetitions), with which the eigenvalues and eigenvectors that represent the subsets of the signal markup were calculated. The signals generated by moving RBC were isolated via an adaptive regression filter to remove the eigen components that represent static tissue, whereas the frequency components of moving RBC were calculated through first lag-one

autocorrelation of the obtained eigenvectors. Then, the capillary flow speed was obtained according to a linear relationship between measured frequency and RBC velocity. For a more accurate evaluation of capillary velocity and heterogeneity, additional segmentation was performed on each B-frame to remove vessels with lumen larger than 15 μm in diameter. Lastly, capillary mean velocity and velocity heterogeneity within the scanned tissue volume were obtained by calculating the mean and standard deviation, respectively, from all capillaries in the 3-D dataset.

5.3.5 *Statistics*

The differences between young ($n=8$) and aged ($n=8$) group were statistically tested using Student t tests (two-tailed) for each variable presented in this study. $p<0.05$ was considered statistically significant.

5.4 Results

5.4.1 *Measured physiology parameters*

The mean recorded heart rate, respiratory rate, arterial blood pressure (diastolic and systolic), as well as blood oxygen saturation level (SpO_2) are shown in Table 1. Respiratory rate and SpO_2 levels were not significantly different between young and aged groups, but the heart rate was 10% lower and arterial pressure (both systolic and diastolic) was 11% lower in the older animals at statistically significant level of $p<0.05$.

Table 5.2. Measured physiology parameters

Parameter	Group	
	Young	Old
Number of animals	8	8
Heart rate (beats/min)	483 ± 52*	435 ± 47*
Respiratory rate (breaths/min)	92 ± 10	87 ± 11
Diastolic arterial pressure (mm Hg)	68 ± 12*	61 ± 10*
Systolic arterial pressure (mm Hg)	81 ± 14*	72 ± 11*
Blood oxygen saturation (SpO ₂ %)	96 ± 1	96 ± 1

Values shown are mean ± std. (standard deviation of group mean). The asterisk symbols and bold text denote statistically significant difference ($p < 0.05$) between the two groups.

5.4.2 Arterial tortuosity

OMAG angiograms shown for young (**Figure 5.3a**) and old mice (**Figure 5.3b**) are of mostly pial vessel networks obtained within 50- μ m-thick slab from cortical surface (**Figure 5.3c**). The average VTI value measured from the 9 AAA segments in young group (**Figure 5.3d**) was 1.19 ± 0.07 , whereas the mean value for the aged group (**Figure 5.3e**) was 1.36 ± 0.09 . The VTI of AAA in old mice is 14% statistically significant higher than that of the young group ($p < 0.01$) (**Figure 5.3f**), indicating that the collateral vessels at in the older mice are more tortuous.

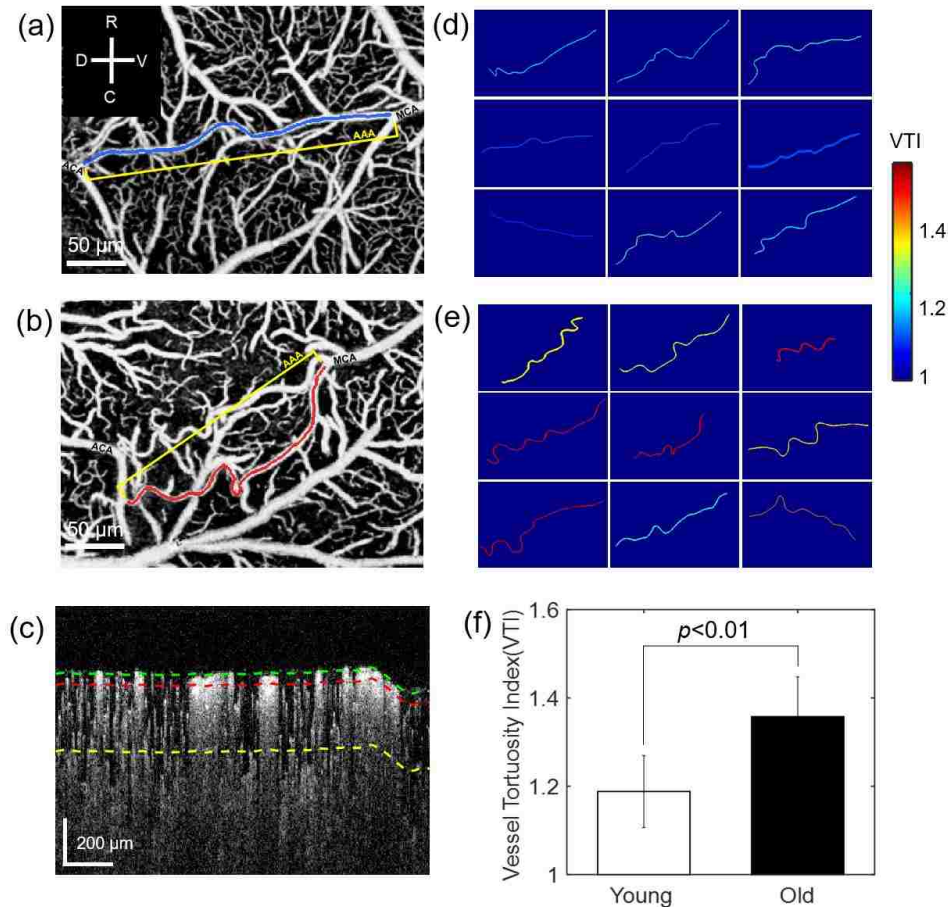


Figure 5.3. Comparison of cerebral pial collateral vessel tortuosity

(a) and (b) are angiograms of the young and old mice, respectively, obtained from *en face* maximum intensity projection (MIP) of 3-D OMAG datasets within 50- μ m-thick slab between the green and red dotted lines shown in B-scan flow cross section image (c). The green line in (c) marks the cortical surface, while the red and yellow lines are located at the depths of 50 and 300 μ m from the cortical surface, respectively. On the angiogram (a) and (b), the selected AAA segments between MCA and ACA are highlighted with false colors. The colors represent calculated VTI values as indicated on the color bar. A total of 9 AAA segments were measured in each group as shown in (d) young and (e) old mice. (f) Comparison of VTI between young and old groups. The values are mean \pm std. (standard deviation of group mean, n=9 segments per group).

5.4.3 Capillary vessel density

Differences in the capillary vessel density between young and old mice were qualitatively revealed by OMAG angiograms and quantified by VAD parameter. In comparison with the light microscopic images (Figure 5.4a and Figure 5.4b), which show larger surface arterioles only, the

OMAG angiograms (Figure 5.4c and Figure 5.4d) reveal high resolution cerebral microvascular networks down to the capillary level. Comparing the angiograms, it is apparent that the older mouse had an uneven distribution of vascular perfusion, where localized rarefaction of capillary perfusion can be seen (Figure 5.4d). The distribution of VAD is more heterogeneous in the old mice (Figure 5.4f) compared to the young (Figure 5.4e). Frequency histogram distribution further shows higher population of VAD over the mean for young mice (Figure 5.4g), and statistical evaluation reveals the VAD of old mice (0.34 ± 0.08) is 15% statistically significant lower than that of young mice (0.40 ± 0.05) at a significant level of $p < 0.01$ (Figure 5.4h).

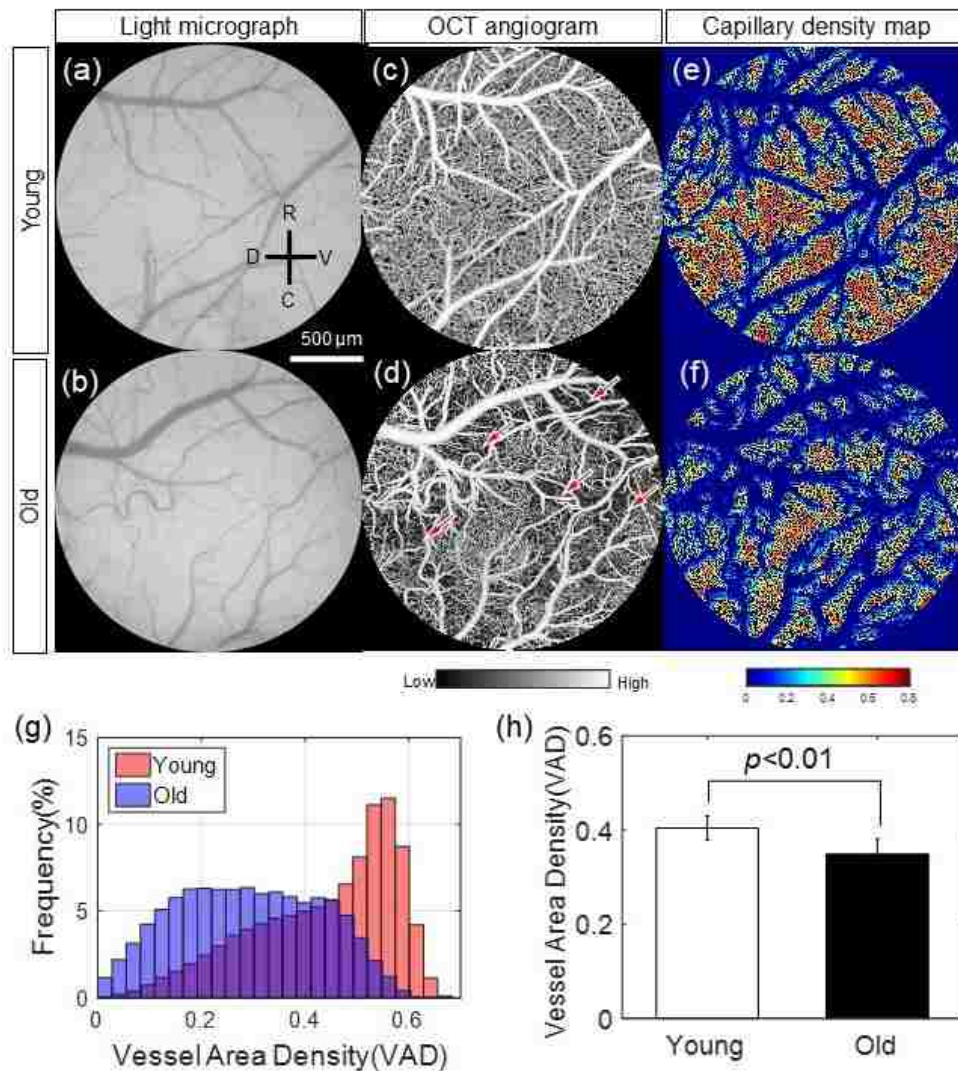


Figure 5.4. Comparison of the cerebral capillary vessel density

(a) and (b) Bright-field microscopy images of young and old mice, respectively, in a $2.5\text{mm} \times 2.5\text{mm}$ region within cranial window. (c) and (d) OMAG angiograms corresponding to (a) and (b), respectively, constructed by *en face* MIP within 300- μm -thick slab from cortical surface. Red arrows in (d) point out a suspected regional capillary rarefaction in the old animal. (c) and (f) are color index-coded VAD maps of young and old mice, respectively. (g) The VAD frequency histogram distributions of young (coral) and old mice (blue). (h) Comparison of VAD between young and old mice. The values are mean \pm std. (standard deviation of group mean, $n=8$ animals per group).

5.4.4 CBF measurements from PA flow

Bidirectional blood flow velocity maps were revealed by DOMAG for young and old mice (**Figure 5.5a**), and an x-y orthogonal slice from a 3-D dataset (**Figure 5.5b**) produces a projection of flow cross sections (**Figure 5.5c**). In **Figure 5.5c**, PA and RV axial velocity projections on x-z plane can be seen as green and red dots. We compared aged related differences in the mean velocity, and flow area, and total flow of both PA and RV within a unit region (1 mm^2) in **Figure 5.5d-f**. For the mean velocity measurement (**Figure 5.5d**), the arteriole velocity was measured to be greater than the venule velocity, in both young and old animals. No statistically significant differences were found in penetrating vessel velocity between young and old groups. In general, flow area of venules was larger than arterioles (**Figure 5.5e**). The average flow area of PA is decreased by 35% ($p<0.05$) and flow area of RV is decreased by 32% ($p<0.05$) in older animals. In **Figure 5.5f**, the total flow (mm^3/s) is calculated as velocity (mm/s) \times flow area (mm^2). In the old group, there is a 33% statistically significant reduction ($p<0.01$) in PA total flow, and 31% statistically significant reduction ($p<0.01$) in RV total flow. Additionally, no significant differences were found between PA and RV total flow volume in each individual animal.

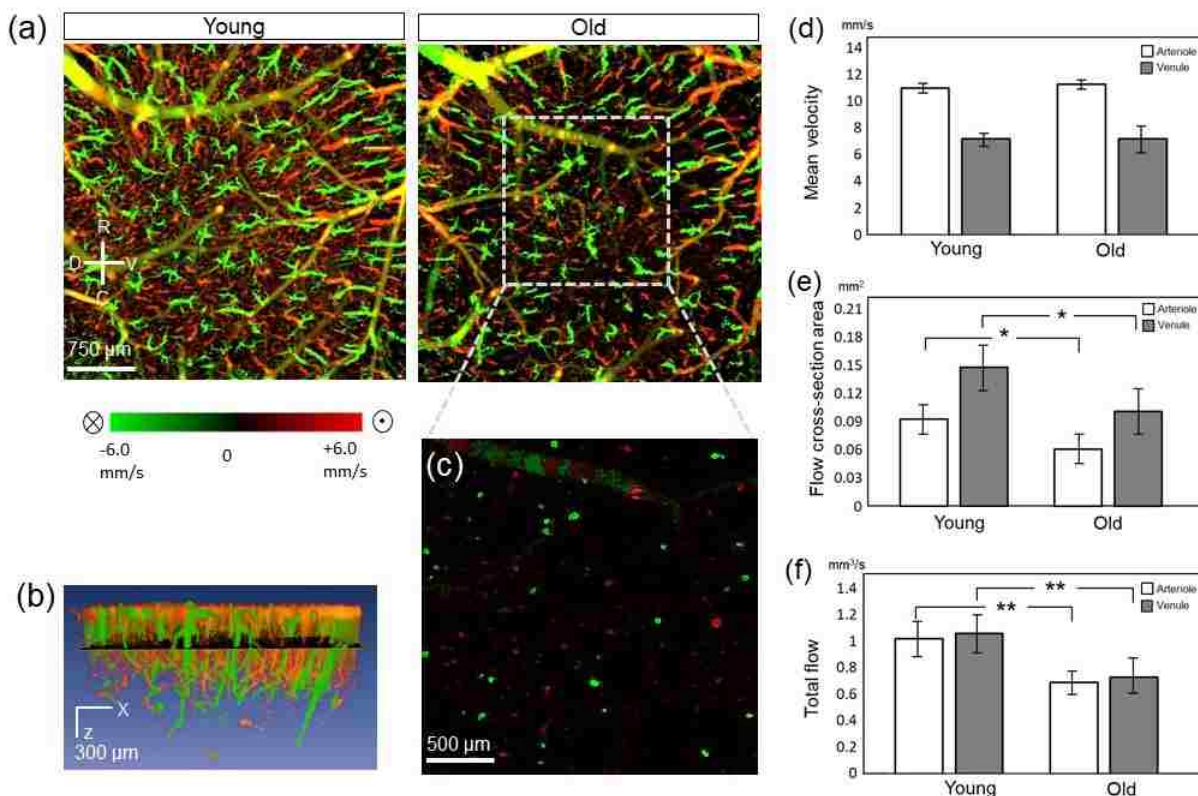


Figure 5.5. CBF and PA/RV parameter comparisons

(a) Bidirectional axial velocity maps of young and old mice generated by *en face* MIP of 3-D DOMAG datasets within 300- μ m-thick slab from cortical surface. Color bar represents RBC axial velocity of the flow descending (negative, green) and rising from (positive, red) the brain in a range of ± 6.0 mm/s for the displayed maps. The yellow color was generated from a mix of green and red signals from the projection effect. (b) 3-D visualization of descending and ascending vessels within the white squared region in (a). (c) Orthogonal slice from (b), at an x-y plane ~ 50 μ m below cortical surface. The green and red dots represent the descending arterioles and rising venules within the selected x-y plane, respectively. Green and red dots shown in (c) are cross sections of arteriole and venule flows. (d), (e) and (f) Comparisons of mean velocity, flow area, and total flow values, respectively, in unit region (1 mm^2) between young and old animals in both penetrating arterioles and venules. Velocity and flow in the plots are absolute values without direction signs. Values are mean \pm std. (Standard deviation of group mean). * represents $p < 0.05$ and ** represents $p < 0.01$.

5.4.5 Capillary mean velocity and heterogeneity

Standard OMAG angiograms of young (Figure 5.6a) and old mice (Figure 5.6b) delineate two regions on each angiogram for velocimetry assessment, one proximal to MCA and the other proximal to ACA. The resulting velocimetry maps of the two selected regions are shown for young

(Figure 5.6c,d) and old mice (Figure 5.6e,f). Each velocimetry map contains $\sim 40,000$ frequency signals within the 3-D tissue volume. The quantification reveals a capillary mean velocity of 1.11 ± 0.17 mm/s in young mice and 1.34 ± 0.23 mm/s in old mice (value taken from mean of both regions). Therefore, the mean capillary velocity is 21% higher in the old group than in the young at difference level of $p < 0.05$ (Figure 5.6g). The standard deviation, which is regarded as velocity heterogeneity was calculated as 0.44 ± 0.07 mm/s and 0.52 ± 0.08 mm/s in young and old mice, respectively, yielding a 19% increase in capillary velocity heterogeneity in the old group ($p \leq 0.05$) (Figure 5.6h).

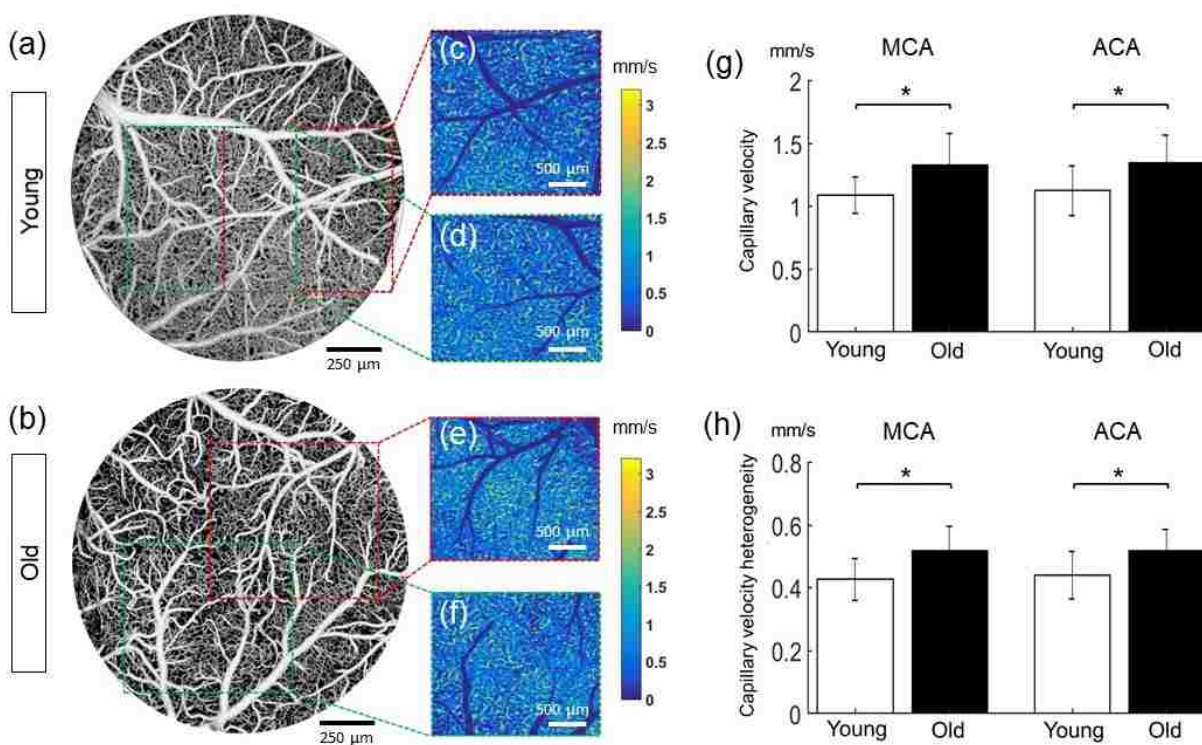


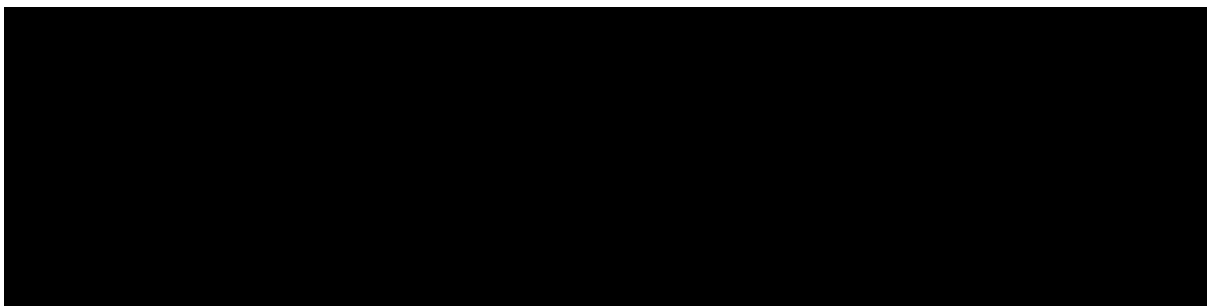
Figure 5.6. Capillary flow velocity and heterogeneity quantification

(a) and (b) Standard OMAG angiograms of young and old mice, respectively. Red and green squares indicated the regions where velocimetry was performed at MCA and ACA locations, respectively. (c)-(f) Capillary velocity maps generated by *en face* projection of 3-D frequency signal with 300 μm thick slab from the cortical surface. Color bar represents RBC velocity (0-3 mm/s). (g) Capillary mean velocity comparison between young and old mice. Values are mean \pm std. (Standard deviation of the group mean). * represents $p < 0.05$ in both MCA and ACA region. (h) Capillary velocity heterogeneity comparison between young and old mice. Values are mean \pm std. * represents $p < 0.05$ and $p = 0.05$ at MCA and ACA region, respectively.

5.5 DISCUSSION

Strong evidence has shown that the degeneration of the brain vasculature and reduced blood flow may underlie age-associated decline in neuronal function or cognition, although the underlying mechanism remains unclear. With a host of novel OCTA imaging algorithms, we quantitatively characterized a series of age-related differences in cerebral vasculature and blood flow *in vivo* with superior spatial detail between healthy young and old mice. A summary of findings is shown in Table 2. Some important changes in aged animals include 14% increase in collateral tortuosity, 15% decrease in capillary density, 33% decrease in arterial CBF, 21% increase in capillary mean velocity and 19% increase in capillary velocity heterogeneity, all at statistically significant levels. We here discuss each characteristic aged-associated changes in details.

Table 5.3. Characteristic age-associated changes



Values shown are mean \pm std. (standard deviation of the mean in each animal among the same group). The asterisk symbols and bold text denote statistically significant difference between the 2 groups (* $p < 0.05$, ** $p < 0.01$ from two-tailed *t-test*).

^a Values are averaged from the measurements in ACA and MCA territories. ^b $p = 0.052$ for capillary velocity heterogeneity measured in ACA regions.

5.5.1 *Aging-related vessel tortuosity increase*

Vascular aging is known to cause progressive deterioration in the cellular structure of the blood vessel wall, subsequently modifying its biomechanical properties and rendering morphological changes within the vessel architecture [79]. One of the most noticeable changes, the development

of arteriole tortuosity, has been observed in cerebral cortex and white matters of animal and human brains in both normal aging and age-related pathological conditions [119]. The majority studies on vessel tortuosity were carried out in human brain post-mortem and were focused on the penetrating arterioles of in white matter diseases [88], [120], with few studies evaluating tortuosity changes during normal vascular aging *in vivo*. Recently, Faber et al. reported an increased tortuosity in rodents from measuring pial cerebral arterioles at the bridge of the MCA and ACA branches, known as AAA, in mouse S1 cortex during normal aging. They demonstrated that the average VTI was much higher (1.43) for the aged group (16-month-old) compared to that of the young group (1.22) (3-month-old), leading to a 6-fold higher flow resistance in cerebral collateral vessel in the aged brain [85]. Our tortuosity measurements of AAA by OCT produced similar VTI values of 1.36 ± 0.09 and 1.19 ± 0.07 for healthy aged (16-month-old) and young mice (2-month-old), respectively (**Figure 5.3f**). Previous studies used fixed brain tissue with dilated and filled pial cortical vessels, albeit an elegant technique used to evaluate post mortem brain vasculature, is prone to potential changes in vessel morphology during tissue processing. In contrast, the label-free, *in vivo* nature of OCTA used in this study preserved the native architectures of the blood vessels and increases the fidelity of the VTI analysis. Apart from methodological differences, the slight variations in VTI values between our results and those previously reported may be attributed to the range of collateral segments selected for measurements. There is currently no accepted definition of the range of collateral segment, as its definition is related to the functional role during an occlusive event. For the consistency within measurements in our study, we followed the branching orders arterioles (e.g. the start point of measuring on the MCA side is at the last bifurcation of M1 segment with equal or similar sized trunks, and that one or both trunks are connected to ACA as collateral).

The mechanisms underlying age-related increase in artery tortuosity in aging remains unclear, but it is well hypothesized that structural alteration in the vessel wall plays a role in the early stage of tortuosity development [121]. As aging begins, smooth muscle cells (SMCs) progressively migrate from the tunica media to accumulate into the intima, and subsequently impair the integrity of the elastic membrane in the intima [122]. Fracturing of the elastin fibers would lead to a reduction in elasticity, resulting in stiffening of the vessel wall. As a result of the arterial stiffening, pulsatile blood pressure in the vessel lumen would become elevated, giving rise to vessel buckling to initiate tortuosity development [123].

The fragmentation of elastin, which has been reported in the artery wall of aged subjects, has been considered a cause of the vessel lengthening and tortuosity progression [124]. As a result, tortuosity increases the vessel length, and with each turn and loop there is a loss of kinetic energy that potentially reduces the flow speed in these vessels[125]. While mild increase of vessel tortuosity may be asymptomatic, severe tortuosity developed with aging can significantly reduce conductance ability of the blood vessels and diminish cerebral perfusion; hence, producing focal ischemic lesion and cellular damage in the downstream tissue [120], [125]. Tortuous penetrating arterioles in the white matter, for instance, are found to be a critical contributing factor to neurodegeneration in a subset of leukoaraiosis (LA) [88]. In another case, augmented tortuosity in the cerebral pial arterioles can cause collateral rarefaction, which could increase blood flow resistance during arteriogenesis and contribute to a more severe ischemic stroke phenotype in older subjects [85]. In addition to the coiling, looping, and spiraling profiles of blood vessels, the increased tortuosity is also associated with a greatly expanded Virchow-Robin perivascular space where amyloid movement occurs [126]. The enlarged perivascular space could disrupt the drainage of amyloid deposits, contributing to the age-associated AD pathology [127].

Though tortuosity is found to be an important vascular factor contributing to various age-related pathological conditions, however, it is neither necessary nor sufficient to produce an LA or AD [88]. A number of other vascular factors are critically involved in aging and the potential disease pathogenesis, which were also revealed in this study by OCTA as discussed in the following sections.

5.5.2 *Aging-related capillary loss*

The distance that oxygen can diffuse from blood into oxygen-consuming tissue is limited [2]. The metabolically demanding nature of the brain means, therefore, that it must be supplied by a dense network of microvessels, so that each point in the tissue is within a distance of oxygen diffusion from the nearest blood vessel. A decrease in microvascular density may increase the risk of tissue hypoxia, and may reduce the oxygen extraction efficiency during functional activity [128]. In comparison with the scarcity of systemic studies conducted for the investigation of arterial tortuosity during normal aging, the microvascular density changes through aging has attracted sizable interest. Collective evidence from 37 earlier studies have revealed an age-related vascular density decrease in both aging animals and human post-mortem [119]. More specifically, an 8% to 43% reduction in capillary numbers [89], [93], [94], [96], [97] and a 12% to 39% reduction in capillary density [90]–[92], [95] were observed in brain of aged rats (22 to 31-month-old), and a decrease in capillary density of 16% to 50% was measured from healthy aged human subjects (age 79 to 90) compared with younger subjects (age 49 to 57) [98], [99], [101], [102], [127]. Recently through the imaging of fluorescein isothiocyanate-dextran (FITC) dye-labeled cerebral capillary vessels using TPM in anesthetized rats, Desjardin et al. [55] observed 20% decrease in capillary density in older rats. In the current study, capillary density was measured *in vivo* in the brains of anesthetized mice with OCTA without the need for exogenous contrast agents. The VAD

of young and aged animals were measured as 0.40 ± 0.05 and 0.34 ± 0.08 , respectively, which revealed an age-associated reduction in capillary density by 15%. Although the values from two groups were close, the difference is statistically significant ($p < 0.01$) and has important implication on capillary flow dynamics and potentially brain oxygen extraction efficiency. In our penetrating vessel measurement by DOMAG, we surprisingly found little differences in arterial velocity between young and old groups, while capillary velocity was measured 21% in the old animals from capillary velocimetry measurement. We therefore speculate such dramatic increase in downstream flow velocity may be attributed, at least in part, to capillary density reduction.

Despite a lack of clear consensus concerning the causes of capillary loss, previous studies have suggested that age-dependent microvascular dropout may be associated with a decline in amplitude of pulsatile secretion of growth hormone (GH) and the resulting decrease in plasma levels of insulin-like growth factor 1 (IGF-1) with aging [129]. Both GH and IGF-1 are responsible for the regulation of vascular growth, maintenance, and remodeling [130], and with advancing age, the secretion of these hormones is reduced, depressing the vascular regulation necessary for maintenance of downstream microvasculature, resulting in a progressive loss of microvessels. Furthermore, aging is associated with increasing blood pressure, and hypertension is known to cause vessel rarefaction [131].

Although the causal relationship between capillary loss and neurodegeneration is still debatable, the possible contribution of microvascular deficiencies to aged brain as well as aged-related pathologies in cerebral vasculature and function [84], [132], could be studied under OCTA to enhance a comprehensive understanding of CBF reduction in these conditions.

5.5.3 CBF modification in the aging brain

The energy requirement of the brain is met almost exclusively by the oxidative metabolism of glucose, which is delivered to local neuron cells through blood vessels by continuous and sufficient CBF [2]. Given that CBF is maintained and regulated by the coordinated efforts of interconnected blood vessels, including cerebral arteries, arterioles and capillaries [133], age-related modifications in the arterial morphology and capillary density undoubtedly impact both resting state CBF and the ability to adjust blood flow during neuronal activities. The latter hemodynamic feature, also referred to as regional CBF (rCBF) change during functional activation, is coupled with the cerebral metabolic rate of oxygen (CMRO₂) in a disproportionate manner [48], which creates a contrast signal that can be detected by fMRI [105] or PET [106].

Numerous studies have utilized flow-metabolism signals to investigate rCBF change with aging in human brains. Among those investigations, an age-related rCBF reduction was reported with both young and old comparison studies [105], [109] and correlative studies between rCBF and life time [106], [134], [135]. Although useful for the assessment of CBF involvement in brain function and performance during aging, these measurements only revealed relative changes in rCBF with respect to local cerebral metabolic rates. An absolute CBF from single arterioles was unobtainable by these imaging modalities, which fails to establish an association between the magnitudes of vascular structure modification with *in vivo* blood flow changes in the resting brain during vascular aging. On the other hand, studies using transcranial Doppler sonography [107], [136] has successfully examined the blood flow velocity in basal cerebral arteries in the resting human brain, and observed decreased blood flow velocity with increasing age. In our current study, we applied the Doppler principle in OCTA technology to measure the velocity in penetrating vessels in mouse brain. The high-resolution vessel velocity maps produced by DOMAG also

provided an ability of PA/RV flow area quantification, from which arteriole and venule CBF (mm^3/s) of a cortical region can be obtained by velocity (mm/s) \times area (mm^2). In general, venules flow slower than arterioles (**Figure 5.5d**), but with great number of branches and larger surface areas (**Figure 5.5e**) than arterioles. The total flow volume of PA and RV almost equals to each other within each group (**Figure 5.5f**) as an implication of flow conservation, which validate the accuracy of DOMAG measurements on CBF. We compared the velocity, flow area, and CBF between young and old groups ($n=8$). Interestingly, mean velocities of both arterioles and venules are not significantly different between two age groups. The flow area (cross section size), though, is significantly decreased in older animals, by 35% ($p<0.05$) in PA and 32% ($p<0.05$) in RV, which indicates reductions in vessel size and vessel population in the older animals. Such change has significant effect on the CBF. As a result, there is a 33% statistically significant reduction ($p<0.01$) in PA total flow, and 31% statistically significant reduction ($p<0.01$) in RV total flow.

Owing to the joint application of Doppler velocity measurements and OCTA, resting CBF can be evaluated concurrently with quantitative vessel tortuosity and density assessment *in vivo* through one-platform imaging. The CBF profile obtained here may be used as an important parameter to assess the wellness of neurovascular system. Together with a comprehensive evaluation on structural parameters, it may facilitate a discovery of critical thresholds in vascular modifications during aging, of which the magnitude of change is not secondary to normal aging but may instead indicate impending pathologies.

5.5.4 *Capillary velocity heterogeneity development during aging*

The capillary flow pattern, a hemodynamic parameter separated from CBF, plays an equally critical role in the dynamics of tissue oxygenation and neuron functions [49]. An essential imaging feature offered by our OCTA, aside from its ability to measure CBF in arterioles, is the capability

of quantitatively analyzing the RBC speed and distribution from a large array of capillary vessels that no other current imaging techniques can achieve.

The significance of the spatiotemporal distribution of RBC speed within the capillary bed for normal brain function and pathology development has been vigorously reported in recent years. According to a model established by Jespersen and Østergaard [49], higher capillary transit time heterogeneity (CTH), especially at shorter transit times (higher speeds), results in lower oxygen delivery to tissue relative to homogenous transit times across capillary vessels. The progressive development of CTH suspected with aging, therefore, is thought to have a causative role in cognitive impairment with advancing age [137], [138]. Comparatively speaking, however, little information can be cited referring to the relevance of capillary heterogeneity to aging due to the inherent challenges associated with *in vivo* imaging of single-file, rapidly moving RBC in capillary vessels. To our knowledge, only one study, using high-speed TMP, has reported capillary velocity and heterogeneity differences between young and old rats from scanning an average number of 38 (12~93) capillaries in the S1 cortex of each brain, which revealed a 48% and 43% increase in RBC mean velocity and spatial heterogeneity (standard deviation), respectively, within the aged group [55]. From their study, however, if excluding the animals with less than 20 measured capillaries, in which the samples are too few for adequate heterogeneity evaluation, age-related difference in heterogeneity would not be statistically significant. Applying the OCTA velocimetry in this aging study, we targeted at the dynamic signal generated from RBC movements within the capillary bed and analyzed ~40,000 frequency-derived RBC velocities within each 3-D tissue volume obtained from the resting S1 cortex of young and old mice. We showed, with statistical confidence, a 21% increase in the mean capillary velocity ($p < 0.05$) (**Figure 5.6g**) and a 19% increase in heterogeneity ($p \leq 0.05$) (**Figure 5.6h**) in the old mice, which revealed, for the first time, an age-related significant

difference in cerebral capillary velocity heterogeneity *in vivo*. Moreover, the 3-D imaging of such large quantities of capillaries was achieved within minutes, which makes it feasible to investigate the on-site hemodynamic response, known as capillary flow homogenization, during stimulus-evoked neuronal activity. How aging impacts functional hyperemia or neurovascular coupling warrants further investigation.

5.5.5 *Study limitation*

Several limitations from the technical perspective of OCT imaging will be addressed. First, the range of imaging depth for capillary density and velocity measurements was limited to 300 μm from the cortical surface (corresponding to layers I, II, and III of the cortex). Such choice was made to eliminate a bias in measuring at deeper cortical layers due to multiple-scattering that might cause signal attenuation and resolution degradation. Furthermore, due to such limitation, only pial arterioles were taken as a representative vessel group for tortuosity evaluation. To further investigate vessel tortuosity in deeper brain layers and its causative role in white matter diseases, histological analyses are required. Additionally, in capillary velocimetry method, a linear relationship between ED-based frequency and mean capillary transit velocity was used based on validation on simple network phantom experiments. An improved correlation between frequency and RBC velocity considering the interwoven capillary network and the size and shape of RBC remains to be fully explored. However, neither imaging limitations here are thought to be significant enough to invalidate our comparisons between young and old groups in the current study.

The use of inhalational isoflurane has been shown to influence animal physiology parameters. Overall, the anesthetized animals tend to have increased heart rate, reduced blood pressure, and could potentially develop hypercapnia over time [139]–[141]. In this study, the level of isoflurane

was controlled at 1.5% v/v throughout, which is at the level proven in a previous study to yield stable blood pressure and heart rate values comparable to those observed in the animal's conscious state [142], and we monitored animal physiology parameters during the experiment as shown in **Table 5.2**. The heart rate (HR) and blood pressure (BP) in the old group were on the lower side. One explanation for this could be that age reduces the amount of isoflurane needed [143], and as we kept the same level of isoflurane in both groups, the old mice might possibly be in a deeper anesthetic state compare to the young. The effect of isoflurane on heart and vascular function also depends on the level of oxygen [111]. In our study, the SpO₂ was monitored, and maintained at ~96% with the use of air/oxygen gas mixture (0.8 L/min air and 0.2 L/min O₂). None of the animals developed hypercapnia, and there are no differences in SpO₂ level between young and old groups, which rule out this variable from affecting physiology differences. The observed differences in physiology parameters (HR, BP) may have influences on the measured blood flow values (e.g. CBF and capillary velocity), which remains to be explored in the future study using awake mouse. Nonetheless, the differences in the level of anesthesia does not invalidate our main observations of age-associated differences in this study, especially in vascular structure, tortuosity, and capillary density. Further investigation may be warranted in comparing the OCTA measured parameters in young and aged mice under awake conditions to exclude the effect of isoflurane anesthesia on microcirculatory dynamics *in vivo* [144].

5.6 CONCLUSION

In this study, we have systematically investigated age-associated changes in vascular features in mouse brains *in vivo* using a collection of OCTA based algorithms. From the micrometer resolution angiogram, an increased cerebral arterial tortuosity with a decreased capillary density

in old mice was revealed simultaneously, which were consistent with previously published results. Alongside with vessel structure modification, changes in hemodynamic parameters, including decreased arterial CBF and increased capillary velocity and heterogeneity were uncovered within the older age group. OCTA presented a superior advantage for multi-feature evaluation using just one imaging platform. Such information would facilitate a comprehensive understanding of vascular aging and its involvement in the age-related neurovascular diseases.

Chapter 6. SUMMARY AND FUTURE WORK

In this dissertation, the emerging applications of functional OCTA in neurovascular research are comprehensively presented. From pial network to penetrating arterioles and then to capillary bed, from mapping the cortical vasculature to the *in vivo* detection of functional blood flow parameters in a variety of physiological conditions, the OCTA possess a great potential in guiding the study of brain functions and disease mechanisms.

Specifically, three major questions in the neurovascular field were being answered through the imaging studies in this thesis. First, a puzzle in the fMRI signal origin, which is the incompletely metabolized blood oxygen at the activated neural tissue that gives rise to a BOLD contrast. From a microcirculatory prospective, as revealed in Chapter 3, capillary flow heterogeneity influences the tissue oxygen extraction ability, and in order to achieve maximum oxygenation, capillary flow must go through a homogenization process. Second, a leptomeningeal collateral circulation behavior during ischemic stroke, which was not accessible with previous imaging techniques, was unraveled with OMAG and DOMAG in a mouse MCAO model in Chapter 4. Vasodynamics of both pial collaterals and their connecting penetrating arterioles were revealed to demonstrate a vascular self-protective mechanism that provides therapeutic indications to stroke onset. The third application area address an important public health problem in the current society: aging. All applicable OCTA algorithms were used to evaluate the vascular aging in the mouse brain in Chapter 5, with a purpose to acknowledge the normal aging-related vascular changes and determine the threshold for pathology-associated changes. Features that were only seen previously by histology only (e.g. tortuous blood vessel development, vascular density dropout, CBF decrease, capillary rarefaction and heterogeneity increase, etc.) were revealed and quantified, for the first time *in vivo*, from a single imaging platform. Many features may have indications to the

risk of developing neurodegenerative diseases, such as Alzheimer's disease, and the imaging platform present a potential for future investigation of these conditions in pathology models.

Through the application process, an important recent advance in OCTA algorithms, capillary velocimetry, was shown useful to depict the microcirculatory dynamics in the living tissue bed. Aside from its application in neuroscience, the technique has potentials in other experimental and clinical field, including ophthalmology and dermatology, as the pathology of many diseases are associated with the malfunction of capillary flow and microcirculation.

There are still some caveats in OCTA as no single technology is perfect for all usage. For one, the optical penetration of OCT is limited (mm scale), restricting its brain imaging application to animal models only for mostly mechanisms study. Also, the nature of not requiring contrast agents for imaging has hindered the OCT detection of neural/cellular activities in the living brain on top of the more dynamic vascular behaviors. However, other intrinsic markers in the dynamic tissue bed that may alter the optical properties remain to be explored, and the high spatiotemporal resolution and 3-D capability of OCT has advantages with such explorations in the near future.

BIBLIOGRAPHY

- [1] R. Swanson, *Review of Clinical and Functional Neuroscience*, vol. Chapter 11. Dartmouth Medical School, 2006.
- [2] L. Gagnon, A. F. Smith, D. A. Boas, A. Devor, T. W. Secomb, and S. Sakadžić, “Modeling of Cerebral Oxygen Transport Based on In vivo Microscopic Imaging of Microvascular Network Structure, Blood Flow, and Oxygenation,” *Front. Comput. Neurosci.*, vol. 10, 2016.
- [3] N. G. Campeau and J. Huston, “Vascular disorders--magnetic resonance angiography: brain vessels,” *Neuroimaging Clin. N. Am.*, vol. 22, no. 2, pp. 207–233, x, May 2012.
- [4] C. B. Schaffer *et al.*, “Two-photon imaging of cortical surface microvessels reveals a robust redistribution in blood flow after vascular occlusion,” *PLoS Biol.*, vol. 4, no. 2, p. e22, Feb. 2006.
- [5] A. K. Dunn, A. Devor, A. M. Dale, and D. A. Boas, “Spatial extent of oxygen metabolism and hemodynamic changes during functional activation of the rat somatosensory cortex,” *Neuroimage*, vol. 27, no. 2, pp. 279–290, Aug. 2005.
- [6] Y. Ma *et al.*, “Wide-field optical mapping of neural activity and brain haemodynamics: considerations and novel approaches,” *Philos. Trans. R. Soc. Lond., B, Biol. Sci.*, vol. 371, no. 1705, 05 2016.
- [7] P. H. Tomlins and R. K. Wang, “Theory, developments and applications of optical coherence tomography,” *J. Phys. D: Appl. Phys.*, vol. 38, no. 15, pp. 2519–2535, Jul. 2005.
- [8] W. Drexler and J. G. Fujimoto, “State-of-the-art retinal optical coherence tomography,” *Progress in Retinal and Eye Research*, vol. 27, no. 1, pp. 45–88, Jan. 2008.
- [9] C.-L. Chen and R. K. Wang, “Optical coherence tomography based angiography [Invited],” *Biomed Opt Express*, vol. 8, no. 2, pp. 1056–1082, Feb. 2017.
- [10] J. Fingler, R. J. Zawadzki, J. S. Werner, D. Schwartz, and S. E. Fraser, “Volumetric microvascular imaging of human retina using optical coherence tomography with a novel motion contrast technique,” *Opt Express*, vol. 17, no. 24, pp. 22190–22200, Nov. 2009.
- [11] Z. Chen *et al.*, “Noninvasive imaging of in vivo blood flow velocity using optical Doppler tomography,” *Opt Lett*, vol. 22, no. 14, pp. 1119–1121, Jul. 1997.
- [12] S. Makita, Y. Hong, M. Yamanari, T. Yatagai, and Y. Yasuno, “Optical coherence angiography,” *Opt. Express, OE*, vol. 14, no. 17, pp. 7821–7840, Aug. 2006.
- [13] J. Barton and S. Stromski, “Flow measurement without phase information in optical coherence tomography images,” *Opt Express*, vol. 13, no. 14, pp. 5234–5239, Jul. 2005.
- [14] Y. Aizu and T. Asakura, “Bio-speckle phenomena and their application to the evaluation of blood flow,” *Optics & Laser Technology*, vol. 23, no. 4, pp. 205–219, Aug. 1991.
- [15] E. Jonathan, J. Enfield, and M. J. Leahy, “Correlation mapping method for generating microcirculation morphology from optical coherence tomography (OCT) intensity images,” *J Biophotonics*, vol. 4, no. 9, pp. 583–587, Sep. 2011.
- [16] Y. Jia *et al.*, “Split-spectrum amplitude-decorrelation angiography with optical coherence tomography,” *Opt Express*, vol. 20, no. 4, pp. 4710–4725, Feb. 2012.
- [17] R. K. Wang, S. L. Jacques, Z. Ma, S. Hurst, S. R. Hanson, and A. Gruber, “Three dimensional optical angiography,” *Opt. Express, OE*, vol. 15, no. 7, pp. 4083–4097, Apr. 2007.

- [18] S. Yousefi, Z. Zhi, and R. K. Wang, "Eigendecomposition-based clutter filtering technique for optical micro-angiography," *IEEE Trans Biomed Eng*, vol. 58, no. 8, Aug. 2011.
- [19] R. K. Wang, L. An, P. Francis, and D. J. Wilson, "Depth-resolved imaging of capillary networks in retina and choroid using ultrahigh sensitive optical microangiography," *Opt. Lett., OL*, vol. 35, no. 9, pp. 1467–1469, May 2010.
- [20] L. An, J. Qin, and R. K. Wang, "Ultrahigh sensitive optical microangiography for in vivo imaging of microcirculations within human skin tissue beds," *Opt. Express, OE*, vol. 18, no. 8, pp. 8220–8228, Apr. 2010.
- [21] R. K. Wang *et al.*, "Wide-field optical coherence tomography angiography enabled by two repeated measurements of B-scans," *Opt Lett*, vol. 41, no. 10, pp. 2330–2333, May 2016.
- [22] R. K. Wang, L. An, S. Saunders, and D. J. Wilson, "Optical microangiography provides depth-resolved images of directional ocular blood perfusion in posterior eye segment," *J Biomed Opt*, vol. 15, no. 2, p. 020502, Apr. 2010.
- [23] R. K. Wang and L. An, "Doppler optical micro-angiography for volumetric imaging of vascular perfusion in vivo," *Opt. Express, OE*, vol. 17, no. 11, pp. 8926–8940, May 2009.
- [24] L. Shi, J. Qin, R. Reif, and R. K. Wang, "Wide velocity range Doppler optical microangiography using optimized step-scanning protocol with phase variance mask," *J Biomed Opt*, vol. 18, no. 10, p. 106015, Oct. 2013.
- [25] V. J. Srinivasan *et al.*, "Quantitative cerebral blood flow with optical coherence tomography," *Opt Express*, vol. 18, no. 3, pp. 2477–2494, Feb. 2010.
- [26] S. Yousefi and R. K. Wang, "Simultaneous estimation of bidirectional particle flow and relative flux using MUSIC-OCT: phantom studies," *Phys. Med. Biol.*, vol. 59, no. 22, pp. 6693–6708, Oct. 2014.
- [27] R. K. Wang, Q. Zhang, Y. Li, and S. Song, "Optical coherence tomography angiography-based capillary velocimetry," *JBO, JBOPFO*, vol. 22, no. 6, p. 066008, Jun. 2017.
- [28] W. J. Choi *et al.*, "Characterizing relationship between optical microangiography signals and capillary flow using microfluidic channels," *Biomed Opt Express*, vol. 7, no. 7, pp. 2709–2728, Jul. 2016.
- [29] R. K. Wang, "Signal degradation by multiple scattering in optical coherence tomography of dense tissue: a Monte Carlo study towards optical clearing of biotissues," *Phys Med Biol*, vol. 47, no. 13, pp. 2281–2299, Jul. 2002.
- [30] C. Stetter, M. Hirschberg, B. Nieswandt, R.-I. Ernestus, M. Heckmann, and A.-L. Sirén, "An experimental protocol for in vivo imaging of neuronal structural plasticity with 2-photon microscopy in mice," *Exp Transl Stroke Med*, vol. 5, no. 1, p. 9, Jul. 2013.
- [31] A. Holtmaat *et al.*, "Long-term, high-resolution imaging in the mouse neocortex through a chronic cranial window," *Nat Protoc*, vol. 4, no. 8, pp. 1128–1144, 2009.
- [32] A. Holtmaat, V. de Paola, L. Wilbrecht, J. T. Trachtenberg, K. Svoboda, and C. Portera-Cailliau, "Imaging neocortical neurons through a chronic cranial window," *Cold Spring Harb Protoc*, vol. 2012, no. 6, pp. 694–701, Jun. 2012.
- [33] E. A. Kelly and A. K. Majewska, "Chronic imaging of mouse visual cortex using a thinned-skull preparation," *J Vis Exp*, no. 44, Oct. 2010.
- [34] P. J. Drew *et al.*, "Chronic optical access through a polished and reinforced thinned skull," *Nat. Methods*, vol. 7, no. 12, pp. 981–984, Dec. 2010.
- [35] J. I. Szu *et al.*, "Thinned-skull cortical window technique for in vivo optical coherence tomography imaging," *J Vis Exp*, no. 69, p. e50053, Nov. 2012.

- [36] M. Isshiki and S. Okabe, "Evaluation of cranial window types for in vivo two-photon imaging of brain microstructures," *Microscopy (Oxf)*, vol. 63, no. 1, pp. 53–63, Feb. 2014.
- [37] Y. Li, U. Baran, and R. K. Wang, "Application of Thinned-Skull Cranial Window to Mouse Cerebral Blood Flow Imaging Using Optical Microangiography," *PLOS ONE*, vol. 9, no. 11, p. e113658, Nov. 2014.
- [38] D. Attwell and C. Iadecola, "The neural basis of functional brain imaging signals," *Trends Neurosci.*, vol. 25, no. 12, pp. 621–625, Dec. 2002.
- [39] T. L. Davis, K. K. Kwong, R. M. Weisskoff, and B. R. Rosen, "Calibrated functional MRI: mapping the dynamics of oxidative metabolism," *Proc. Natl. Acad. Sci. U.S.A.*, vol. 95, no. 4, pp. 1834–1839, Feb. 1998.
- [40] F. Hyder, "Neuroimaging with calibrated FMRI," *Stroke*, vol. 35, no. 11 Suppl 1, pp. 2635–2641, Nov. 2004.
- [41] S. Ogawa, T. M. Lee, A. R. Kay, and D. W. Tank, "Brain magnetic resonance imaging with contrast dependent on blood oxygenation," *Proc. Natl. Acad. Sci. U.S.A.*, vol. 87, no. 24, pp. 9868–9872, Dec. 1990.
- [42] P. T. Fox and M. E. Raichle, "Focal physiological uncoupling of cerebral blood flow and oxidative metabolism during somatosensory stimulation in human subjects," *Proc. Natl. Acad. Sci. U.S.A.*, vol. 83, no. 4, pp. 1140–1144, Feb. 1986.
- [43] C. T. Drake and C. Iadecola, "The role of neuronal signaling in controlling cerebral blood flow," *Brain Lang*, vol. 102, no. 2, pp. 141–152, Aug. 2007.
- [44] S.-G. Kim and S. Ogawa, "Biophysical and physiological origins of blood oxygenation level-dependent fMRI signals," *J. Cereb. Blood Flow Metab.*, vol. 32, no. 7, pp. 1188–1206, Jul. 2012.
- [45] A. L. Vazquez *et al.*, "Vascular dynamics and BOLD fMRI: CBF level effects and analysis considerations," *Neuroimage*, vol. 32, no. 4, pp. 1642–1655, Oct. 2006.
- [46] C. P. Derdeyn *et al.*, "Variability of cerebral blood volume and oxygen extraction: stages of cerebral haemodynamic impairment revisited," *Brain*, vol. 125, no. Pt 3, pp. 595–607, Mar. 2002.
- [47] C. Leithner and G. Royle, "The oxygen paradox of neurovascular coupling," *J. Cereb. Blood Flow Metab.*, vol. 34, no. 1, pp. 19–29, Jan. 2014.
- [48] O. B. Paulson, S. G. Hasselbalch, E. Rostrup, G. M. Knudsen, and D. Pelligrino, "Cerebral blood flow response to functional activation," *J. Cereb. Blood Flow Metab.*, vol. 30, no. 1, pp. 2–14, Jan. 2010.
- [49] S. N. Jespersen and L. Østergaard, "The roles of cerebral blood flow, capillary transit time heterogeneity, and oxygen tension in brain oxygenation and metabolism," *J. Cereb. Blood Flow Metab.*, vol. 32, no. 2, pp. 264–277, Feb. 2012.
- [50] G. N. Stewart, "Reseraches on the circulation time in organs and on the influences which affect it. Parts I-III," *J Physiol*, vol. 15, pp. 1–89, 1894.
- [51] E. Gutiérrez-Jiménez *et al.*, "Effect of electrical forepaw stimulation on capillary transit-time heterogeneity (CTH)," *J. Cereb. Blood Flow Metab.*, vol. 36, no. 12, pp. 2072–2086, Dec. 2016.
- [52] R. Hoshikawa *et al.*, "Dynamic Flow Velocity Mapping from Fluorescent Dye Transit Times in the Brain Surface Microcirculation of Anesthetized Rats and Mice," *Microcirculation*, vol. 23, no. 6, pp. 416–425, Aug. 2016.
- [53] B. Stefanovic *et al.*, "Functional reactivity of cerebral capillaries," *J. Cereb. Blood Flow Metab.*, vol. 28, no. 5, pp. 961–972, May 2008.

- [54] D. Kleinfeld, P. P. Mitra, F. Helmchen, and W. Denk, "Fluctuations and stimulus-induced changes in blood flow observed in individual capillaries in layers 2 through 4 of rat neocortex," *Proc. Natl. Acad. Sci. U.S.A.*, vol. 95, no. 26, pp. 15741–15746, Dec. 1998.
- [55] M. Desjardins, R. Berti, J. Lefebvre, S. Dubeau, and F. Lesage, "Aging-related differences in cerebral capillary blood flow in anesthetized rats," *Neurobiol. Aging*, vol. 35, no. 8, pp. 1947–1955, Aug. 2014.
- [56] J. Lee, J. Y. Jiang, W. Wu, F. Lesage, and D. A. Boas, "Statistical intensity variation analysis for rapid volumetric imaging of capillary network flux," *Biomed Opt Express*, vol. 5, no. 4, pp. 1160–1172, Apr. 2014.
- [57] Z. Chen, T. E. Milner, D. Dave, and J. S. Nelson, "Optical Doppler tomographic imaging of fluid flow velocity in highly scattering media," *Opt Lett*, vol. 22, no. 1, pp. 64–66, Jan. 1997.
- [58] Y. Li, W. J. Choi, W. Qin, U. Baran, L. M. Habenicht, and R. K. Wang, "Optical coherence tomography based microangiography provides an ability to longitudinally image arteriogenesis in vivo," *Journal of Neuroscience Methods*, vol. 274, no. Supplement C, pp. 164–171, Dec. 2016.
- [59] W. J. Choi, Y. Li, W. Qin, and R. K. Wang, "Cerebral capillary velocimetry based on temporal OCT speckle contrast," *Biomed Opt Express*, vol. 7, no. 12, pp. 4859–4873, Dec. 2016.
- [60] J. Lee, W. Wu, and D. A. Boas, "Early capillary flux homogenization in response to neural activation," *J. Cereb. Blood Flow Metab.*, vol. 36, no. 2, pp. 375–380, Feb. 2016.
- [61] J. Qin, L. Shi, S. Dziennis, R. Reif, and R. K. Wang, "Fast synchronized dual-wavelength laser speckle imaging system for monitoring hemodynamic changes in a stroke mouse model," *Opt Lett*, vol. 37, no. 19, pp. 4005–4007, Oct. 2012.
- [62] U. Baran, Y. Li, and R. K. Wang, "Vasodynamics of pial and penetrating arterioles in relation to arteriolo-arteriolar anastomosis after focal stroke," *NPh, NEURO*, vol. 2, no. 2, p. 025006, Jun. 2015.
- [63] A. Sigler, M. H. Mohajerani, and T. H. Murphy, "Imaging rapid redistribution of sensory-evoked depolarization through existing cortical pathways after targeted stroke in mice," *Proc. Natl. Acad. Sci. U.S.A.*, vol. 106, no. 28, pp. 11759–11764, Jul. 2009.
- [64] A. Villringer, A. Them, U. Lindauer, K. Einhupl, and U. Dirnagl, "Capillary perfusion of the rat brain cortex. An in vivo confocal microscopy study," *Circ. Res.*, vol. 75, no. 1, pp. 55–62, Jul. 1994.
- [65] D. Obrist, B. Weber, A. Buck, and P. Jenny, "Red blood cell distribution in simplified capillary networks," *Philos Trans A Math Phys Eng Sci*, vol. 368, no. 1921, pp. 2897–2918, Jun. 2010.
- [66] P. Blinder, P. S. Tsai, J. P. Kaufhold, P. M. Knutsen, H. Suhl, and D. Kleinfeld, "The cortical angiome: an interconnected vascular network with noncolumnar patterns of blood flow," *Nat. Neurosci.*, vol. 16, no. 7, pp. 889–897, Jul. 2013.
- [67] K. Masamoto, M. Fukuda, A. Vazquez, and S.-G. Kim, "Dose-dependent effect of isoflurane on neurovascular coupling in rat cerebral cortex," *Eur. J. Neurosci.*, vol. 30, no. 2, pp. 242–250, Jul. 2009.
- [68] M. A. Franceschini *et al.*, "The effect of different anesthetics on neurovascular coupling," *Neuroimage*, vol. 51, no. 4, pp. 1367–1377, Jul. 2010.

- [69] P. J. Drew, A. Y. Shih, and D. Kleinfeld, "Fluctuating and sensory-induced vasodynamics in rodent cortex extend arteriole capacity," *Proc. Natl. Acad. Sci. U.S.A.*, vol. 108, no. 20, pp. 8473–8478, May 2011.
- [70] W. Wei, Y. Li, Z. Xie, A. Deegan, and R. K. Wang, "Spatial and temporal heterogeneities of capillary hemodynamics and its functional coupling during neural activation," *IEEE Trans Med Imaging*, Nov. 2018.
- [71] Brozici Mariana, van der Zwan Albert, and Hillen Berend, "Anatomy and Functionality of Leptomeningeal Anastomoses," *Stroke*, vol. 34, no. 11, pp. 2750–2762, Nov. 2003.
- [72] N. Nishimura, C. B. Schaffer, B. Friedman, P. D. Lyden, and D. Kleinfeld, "Penetrating arterioles are a bottleneck in the perfusion of neocortex," *Proc. Natl. Acad. Sci. U.S.A.*, vol. 104, no. 1, pp. 365–370, Jan. 2007.
- [73] H. Toriumi, J. Tatarishvili, M. Tomita, Y. Tomita, M. Unekawa, and N. Suzuki, "Dually supplied T-junctions in arteriolo-arteriolar anastomosis in mice: key to local hemodynamic homeostasis in normal and ischemic states?," *Stroke*, vol. 40, no. 10, pp. 3378–3383, Oct. 2009.
- [74] A. Y. Shih, B. Friedman, P. J. Drew, P. S. Tsai, P. D. Lyden, and D. Kleinfeld, "Active dilation of penetrating arterioles restores red blood cell flux to penumbral neocortex after focal stroke," *J. Cereb. Blood Flow Metab.*, vol. 29, no. 4, pp. 738–751, Apr. 2009.
- [75] A. Y. Shih *et al.*, "The smallest stroke: occlusion of one penetrating vessel leads to infarction and a cognitive deficit," *Nat. Neurosci.*, vol. 16, no. 1, pp. 55–63, Jan. 2013.
- [76] T. Chiang, R. O. Messing, and W.-H. Chou, "Mouse model of middle cerebral artery occlusion," *J Vis Exp*, no. 48, Feb. 2011.
- [77] V. J. Srinivasan *et al.*, "Multiparametric, Longitudinal Optical Coherence Tomography Imaging Reveals Acute Injury and Chronic Recovery in Experimental Ischemic Stroke," *PLOS ONE*, vol. 8, no. 8, p. e71478, Aug. 2013.
- [78] S. Kawachi, S. Sato, Y. Uozumi, H. Nawashiro, M. Ishihara, and M. Kikuchi, "Light-scattering signal may indicate critical time zone to rescue brain tissue after hypoxia," *J Biomed Opt*, vol. 16, no. 2, p. 027002, Feb. 2011.
- [79] J. M. Diaz-Otero, H. Garver, G. D. Fink, W. F. Jackson, and A. M. Dorrance, "Aging is associated with changes to the biomechanical properties of the posterior cerebral artery and parenchymal arterioles," *Am. J. Physiol. Heart Circ. Physiol.*, vol. 310, no. 3, pp. H365–375, Feb. 2016.
- [80] J. C. de la Torre, "Critical threshold cerebral hypoperfusion causes Alzheimer's disease?," *Acta Neuropathol.*, vol. 98, no. 1, pp. 1–8, Jul. 1999.
- [81] J. Attems and K. A. Jellinger, "The overlap between vascular disease and Alzheimer's disease - lessons from pathology," *BMC Medicine*, vol. 12, p. 206, Nov. 2014.
- [82] M. M. Breteler, "Vascular involvement in cognitive decline and dementia. Epidemiologic evidence from the Rotterdam Study and the Rotterdam Scan Study," *Ann. N. Y. Acad. Sci.*, vol. 903, pp. 457–465, Apr. 2000.
- [83] A. Hofman *et al.*, "Atherosclerosis, apolipoprotein E, and prevalence of dementia and Alzheimer's disease in the Rotterdam Study," *Lancet*, vol. 349, no. 9046, pp. 151–154, Jan. 1997.
- [84] E. Farkas and P. G. Luiten, "Cerebral microvascular pathology in aging and Alzheimer's disease," *Prog. Neurobiol.*, vol. 64, no. 6, pp. 575–611, Aug. 2001.

- [85] J. E. Faber *et al.*, "Aging causes collateral rarefaction and increased severity of ischemic injury in multiple tissues," *Arterioscler. Thromb. Vasc. Biol.*, vol. 31, no. 8, pp. 1748–1756, Aug. 2011.
- [86] H.-M. Kang, I. Sohn, J. Jung, J.-W. Jeong, and C. Park, "Age-related changes in pial arterial structure and blood flow in mice," *Neurobiol. Aging*, vol. 37, pp. 161–170, Jan. 2016.
- [87] E. Bullitt *et al.*, "The effects of healthy aging on intracerebral blood vessels visualized by magnetic resonance angiography," *Neurobiol. Aging*, vol. 31, no. 2, pp. 290–300, Feb. 2010.
- [88] C. R. Thore, J. A. Anstrom, D. M. Moody, V. R. Challa, M. C. Marion, and W. R. Brown, "Morphometric analysis of arteriolar tortuosity in human cerebral white matter of preterm, young, and aged subjects," *J. Neuropathol. Exp. Neurol.*, vol. 66, no. 5, pp. 337–345, May 2007.
- [89] F. Amenta *et al.*, "Age-related changes in brain microanatomy: sensitivity to treatment with the dihydropyridine calcium channel blocker darodipine (PY 108-068)," *Brain Res. Bull.*, vol. 36, no. 5, pp. 453–460, 1995.
- [90] E. M. Burns, T. W. Kruckeberg, and P. K. Gaetano, "Changes with age in cerebral capillary morphology," *Neurobiol. Aging*, vol. 2, no. 4, pp. 283–291, 1981.
- [91] M. A. Casey and M. L. Feldman, "Aging in the rat medial nucleus of the trapezoid body. III. Alterations in capillaries," *Neurobiol. Aging*, vol. 6, no. 1, pp. 39–46, 1985.
- [92] J. W. Hinds and N. A. McNelly, "Capillaries in aging rat olfactory bulb: a quantitative light and electron microscopic analysis," *Neurobiol. Aging*, vol. 3, no. 3, pp. 197–207, 1982.
- [93] M. Jucker, K. Bättig, and W. Meier-Ruge, "Effects of aging and vincamine derivatives on pericapillary microenvironment: stereological characterization of the cerebral capillary network," *Neurobiol. Aging*, vol. 11, no. 1, pp. 39–46, Feb. 1990.
- [94] C. A. Knox and A. Oliveira, "Brain aging in normotensive and hypertensive strains of rats. III. A quantitative study of cerebrovasculature," *Acta Neuropathol.*, vol. 52, no. 1, pp. 17–25, 1980.
- [95] W. E. Sonntag, C. D. Lynch, P. T. Cooney, and P. M. Hutchins, "Decreases in cerebral microvasculature with age are associated with the decline in growth hormone and insulin-like growth factor 1," *Endocrinology*, vol. 138, no. 8, pp. 3515–3520, Aug. 1997.
- [96] A. Villena, L. Vidal, F. Díaz, and I. Pérez De Vargas, "Stereological changes in the capillary network of the aging dorsal lateral geniculate nucleus," *Anat Rec A Discov Mol Cell Evol Biol*, vol. 274, no. 1, pp. 857–861, Sep. 2003.
- [97] J. H. Wilkinson, J. W. Hopewell, and H. S. Reinhold, "A quantitative study of age-related changes in the vascular architecture of the rat cerebral cortex," *Neuropathol. Appl. Neurobiol.*, vol. 7, no. 6, pp. 451–462, Dec. 1981.
- [98] W. B. Abernethy, M. A. Bell, M. Morris, and D. M. Moody, "Microvascular density of the human paraventricular nucleus decreases with aging but not hypertension," *Exp. Neurol.*, vol. 121, no. 2, pp. 270–274, Jun. 1993.
- [99] M. A. Bell and M. J. Ball, "Morphometric comparison of hippocampal microvasculature in ageing and demented people: diameters and densities," *Acta Neuropathol.*, vol. 53, no. 4, pp. 299–318, 1981.
- [100] W. R. Brown, D. M. Moody, C. R. Thore, V. R. Challa, and J. A. Anstrom, "Vascular dementia in leukoaraiosis may be a consequence of capillary loss not only in the lesions,

- but in normal-appearing white matter and cortex as well,” *J. Neurol. Sci.*, vol. 257, no. 1–2, pp. 62–66, Jun. 2007.
- [101] L. Buée *et al.*, “Pathological alterations of the cerebral microvasculature in Alzheimer’s disease and related dementing disorders,” *Acta Neuropathol.*, vol. 87, no. 5, pp. 469–480, 1994.
- [102] D. M. Mann, N. R. Eaves, B. Marcyniuk, and P. O. Yates, “Quantitative changes in cerebral cortical microvasculature in ageing and dementia,” *Neurobiol. Aging*, vol. 7, no. 5, pp. 321–330, Oct. 1986.
- [103] X. Xu *et al.*, “Age-related Impairment of Vascular Structure and Functions,” *Aging Dis*, vol. 8, no. 5, pp. 590–610, Oct. 2017.
- [104] K. Kisler, A. R. Nelson, A. Montagne, and B. V. Zlokovic, “Cerebral blood flow regulation and neurovascular dysfunction in Alzheimer disease,” *Nat. Rev. Neurosci.*, vol. 18, no. 7, pp. 419–434, Jul. 2017.
- [105] B. M. Ances *et al.*, “Effects of aging on cerebral blood flow, oxygen metabolism, and blood oxygenation level dependent responses to visual stimulation,” *Hum Brain Mapp*, vol. 30, no. 4, pp. 1120–1132, Apr. 2009.
- [106] J. Aanerud *et al.*, “Brain energy metabolism and blood flow differences in healthy aging,” *J. Cereb. Blood Flow Metab.*, vol. 32, no. 7, pp. 1177–1187, Jul. 2012.
- [107] S. Demirkaya, K. Uluc, S. Bek, and O. Vural, “Normal blood flow velocities of basal cerebral arteries decrease with advancing age: a transcranial Doppler sonography study,” *Tohoku J. Exp. Med.*, vol. 214, no. 2, pp. 145–149, Feb. 2008.
- [108] R. F. Berman, H. Goldman, and H. J. Altman, “Age-related changes in regional cerebral blood flow and behavior in Sprague-Dawley rats,” *Neurobiol. Aging*, vol. 9, no. 5–6, pp. 691–696, Dec. 1988.
- [109] K. Bertsch, D. Hagemann, M. Hermes, C. Walter, R. Khan, and E. Naumann, “Resting cerebral blood flow, attention, and aging,” *Brain Res.*, vol. 1267, pp. 77–88, Apr. 2009.
- [110] S. Heo *et al.*, “Resting hippocampal blood flow, spatial memory and aging,” *Brain Res.*, vol. 1315, pp. 119–127, Feb. 2010.
- [111] C. D. Lynch *et al.*, “Effects of moderate caloric restriction on cortical microvascular density and local cerebral blood flow in aged rats,” *Neurobiol. Aging*, vol. 20, no. 2, pp. 191–200, Apr. 1999.
- [112] H. Wang, L. Shi, J. Qin, S. Yousefi, Y. Li, and R. K. Wang, “Multimodal optical imaging can reveal changes in microcirculation and tissue oxygenation during skin wound healing,” *Lasers Surg Med*, vol. 46, no. 6, pp. 470–478, Aug. 2014.
- [113] G. M. Hutchins, M. M. Miner, and B. H. Bulkley, “Tortuosity as an index of the age and diameter increase of coronary collateral vessels in patients after acute myocardial infarction,” *Am. J. Cardiol.*, vol. 41, no. 2, pp. 210–215, Feb. 1978.
- [114] N. Efford, *Digital Image Processing: A Practical Introduction Using Java (with CD-ROM)*, 1st ed. Boston, MA, USA: Addison-Wesley Longman Publishing Co., Inc., 2000.
- [115] Z. Chu *et al.*, “Quantitative assessment of the retinal microvasculature using optical coherence tomography angiography,” *J Biomed Opt*, vol. 21, no. 6, p. 66008, Jun. 2016.
- [116] A. Y. Kim, Z. Chu, A. Shahidzadeh, R. K. Wang, C. A. Puliafito, and A. H. Kashani, “Quantifying Microvascular Density and Morphology in Diabetic Retinopathy Using Spectral-Domain Optical Coherence Tomography Angiography,” *Invest. Ophthalmol. Vis. Sci.*, vol. 57, no. 9, pp. OCT362–370, Jul. 2016.

- [117] L. Shi, J. Qin, R. Reif, and R. K. Wang, "Wide velocity range Doppler optical microangiography using optimized step-scanning protocol with phase variance mask," *JBO, JBOPFO*, vol. 18, no. 10, p. 106015, Oct. 2013.
- [118] Z. Zhi, W. Cepurna, E. Johnson, T. Shen, J. Morrison, and R. K. Wang, "Volumetric and quantitative imaging of retinal blood flow in rats with optical microangiography," *Biomed Opt Express*, vol. 2, no. 3, pp. 579–591, Feb. 2011.
- [119] W. R. Brown and C. R. Thore, "Review: Cerebral microvascular pathology in aging and neurodegeneration," *Neuropathol Appl Neurobiol*, vol. 37, no. 1, pp. 56–74, Feb. 2011.
- [120] K. M. Spangler, V. R. Challa, D. M. Moody, and M. A. Bell, "Arteriolar tortuosity of the white matter in aging and hypertension. A microradiographic study," *J. Neuropathol. Exp. Neurol.*, vol. 53, no. 1, pp. 22–26, Jan. 1994.
- [121] H.-C. Han, "Twisted blood vessels: symptoms, etiology and biomechanical mechanisms," *J. Vasc. Res.*, vol. 49, no. 3, pp. 185–197, 2012.
- [122] O. Yildiz, "Vascular smooth muscle and endothelial functions in aging," *Ann. N. Y. Acad. Sci.*, vol. 1100, pp. 353–360, Apr. 2007.
- [123] J. C. Kohn, M. C. Lampi, and C. A. Reinhart-King, "Age-related vascular stiffening: causes and consequences," *Front Genet*, vol. 6, Mar. 2015.
- [124] J. Sugawara, K. Hayashi, T. Yokoi, and H. Tanaka, "Age-associated elongation of the ascending aorta in adults," *JACC Cardiovasc Imaging*, vol. 1, no. 6, pp. 739–748, Nov. 2008.
- [125] D. M. Moody, W. P. Santamore, and M. A. Bell, "Does tortuosity in cerebral arterioles impair down-autoregulation in hypertensives and elderly normotensives? A hypothesis and computer model," *Clin Neurosurg*, vol. 37, pp. 372–387, 1991.
- [126] J. A. R. Nicoll, M. Yamada, J. Frackowiak, B. Mazur-Kolecka, and R. O. Weller, "Cerebral amyloid angiopathy plays a direct role in the pathogenesis of Alzheimer's disease. Pro-CAA position statement," *Neurobiol. Aging*, vol. 25, no. 5, pp. 589–597; discussion 603-604, Jun. 2004.
- [127] W. R. Brown, D. M. Moody, C. R. Thore, and V. R. Challa, "Cerebrovascular pathology in Alzheimer's disease and leukoaraiosis," *Ann. N. Y. Acad. Sci.*, vol. 903, pp. 39–45, Apr. 2000.
- [128] S. Hirsch, J. Reichold, M. Schneider, G. Székely, and B. Weber, "Topology and hemodynamics of the cortical cerebrovascular system," *J. Cereb. Blood Flow Metab.*, vol. 32, no. 6, pp. 952–967, Jun. 2012.
- [129] W. E. Sonntag, C. D. Lynch, P. T. Cooney, and P. M. Hutchins, "Decreases in Cerebral Microvasculature with Age Are Associated with the Decline in Growth Hormone and Insulin-Like Growth Factor 1*," *Endocrinology*, vol. 138, no. 8, pp. 3515–3520, Aug. 1997.
- [130] A. S. Khan, D. C. Sane, T. Wannenburg, and W. E. Sonntag, "Growth hormone, insulin-like growth factor-1 and the aging cardiovascular system," *Cardiovasc. Res.*, vol. 54, no. 1, pp. 25–35, Apr. 2002.
- [131] I. A. Sokolova, E. B. Manukhina, S. M. Blinkov, V. B. Koshelev, V. G. Pinelis, and I. M. Rodionov, "Rarefaction of the arterioles and capillary network in the brain of rats with different forms of hypertension," *Microvasc. Res.*, vol. 30, no. 1, pp. 1–9, Jul. 1985.
- [132] V. W. Fischer, A. Siddiqi, and Y. Yusufaly, "Altered angioarchitecture in selected areas of brains with Alzheimer's disease," *Acta Neuropathol.*, vol. 79, no. 6, pp. 672–679, 1990.

- [133] K. Kisler, A. R. Nelson, A. Montagne, and B. V. Zlokovic, "Cerebral blood flow regulation and neurovascular dysfunction in Alzheimer disease," *Nat. Rev. Neurosci.*, vol. 18, no. 7, pp. 419–434, Jul. 2017.
- [134] J. J. Chen, H. D. Rosas, and D. H. Salat, "Age-associated reductions in cerebral blood flow are independent from regional atrophy," *Neuroimage*, vol. 55, no. 2, pp. 468–478, Mar. 2011.
- [135] S. K. Schultz, D. S. O'Leary, L. L. Boles Ponto, G. L. Watkins, R. D. Hichwa, and N. C. Andreasen, "Age-related changes in regional cerebral blood flow among young to mid-life adults," *Neuroreport*, vol. 10, no. 12, pp. 2493–2496, Aug. 1999.
- [136] J. Krejza, Z. Mariak, J. Walecki, P. Szydlak, J. Lewko, and A. Ustymowicz, "Transcranial color Doppler sonography of basal cerebral arteries in 182 healthy subjects: age and sex variability and normal reference values for blood flow parameters," *AJR Am J Roentgenol*, vol. 172, no. 1, pp. 213–218, Jan. 1999.
- [137] L. Østergaard *et al.*, "The capillary dysfunction hypothesis of Alzheimer's disease," *Neurobiol. Aging*, vol. 34, no. 4, pp. 1018–1031, Apr. 2013.
- [138] L. Østergaard *et al.*, "Capillary dysfunction: its detection and causative role in dementias and stroke," *Curr Neurol Neurosci Rep*, vol. 15, no. 6, p. 37, Jun. 2015.
- [139] B. J. A. Janssen, T. De Celle, J. J. M. Debets, A. E. Brouns, M. F. Callahan, and T. L. Smith, "Effects of anesthetics on systemic hemodynamics in mice," *Am. J. Physiol. Heart Circ. Physiol.*, vol. 287, no. 4, pp. H1618–1624, Oct. 2004.
- [140] L. Schlünzen, G. E. Cold, M. Rasmussen, and M. S. Vafaei, "Effects of dose-dependent levels of isoflurane on cerebral blood flow in healthy subjects studied using positron emission tomography," *Acta Anaesthesiol Scand*, vol. 50, no. 3, pp. 306–312, Mar. 2006.
- [141] L. Vutskits and Z. Xie, "Lasting impact of general anaesthesia on the brain: mechanisms and relevance," *Nat. Rev. Neurosci.*, vol. 17, no. 11, pp. 705–717, 18 2016.
- [142] C. Constantinides, R. Mean, and B. J. Janssen, "Effects of isoflurane anesthesia on the cardiovascular function of the C57BL/6 mouse," *ILAR J*, vol. 52, no. 3, pp. e21–31, 2011.
- [143] T. Matsuura, Y. Oda, K. Tanaka, T. Mori, K. Nishikawa, and A. Asada, "Advance of age decreases the minimum alveolar concentrations of isoflurane and sevoflurane for maintaining bispectral index below 50," *Br J Anaesth*, vol. 102, no. 3, pp. 331–335, Mar. 2009.
- [144] M. Moieni *et al.*, "Effects of anesthesia on the cerebral capillary blood flow in young and old mice," presented at the Multiphoton Microscopy in the Biomedical Sciences XV, 2015, vol. 9329, p. 932929.

VITA

Yuandong Li received her B.Sc. in molecular and cell biology from the University of Washington, Seattle/USA, in 2012. She received Ph.D in Bioengineering from the University of Washington, Seattle/USA, in 2019, under the direction supervision of Prof. Ruikang Wang. She is the author/co-author of 23 peer-reviewed journal articles with 6 as the first author. Her research interests include neuroimaging and neurovascular function/disease studies.